Integrated microbioreactor arrays for high-throughput experimentation

by

Harry Lee

Submitted to the Department of Electrical Engineering and Computer Science
in partial fulfillment of the requirements for the degree of

Doctor of Philosophy in Electrical Engineering and Computer Science

at the

MASSACHUSETTS INSTITUTE OF TECHNOLOGY

June 2006

Author .....
Department of Electrical Engineering and Computer Science
March 17, 2006

Certified by .....
Rajeev J. Ram
Associate Professor
Thesis Supervisor

Accepted by .....
Arthur C. Smith
Chairman, Department Committee on Graduate Students

Integrated microbioreactor arrays for high-throughput experimentation

by

Harry Lee

Submitted to the Department of Electrical Engineering and Computer Science
on March 17, 2006, in partial fulfillment of the
requirements for the degree of
Doctor of Philosophy in Electrical Engineering and Computer Science

Abstract

Bioprocesses with microbial cells play an important role in producing biopharmaceuticals such as human insulin and human growth hormone, and other products such as amino acids and biopolymers. Because bioprocesses involve the complicated interaction between the genetics of the microorganisms and their chemical and environmental conditions, hundreds or thousands of microbial growth experiments are necessary for to develop and optimize them. In addition, efforts to develop models for bioprocesses also require numerous growth experiments to study microorganism phenotypes.

This work describes the design and development of integrated arrays of microbioreactors that can provide the oxygen transfer and control capabilities of a stirred tank bioreactor in a high-throughput format. The devices comprise a novel peristaltic oxygenating mixer and microfluidic injectors, which are fabricated using a process that allows combining multiple scale (100μm-1cm) and multiple depth (100μm-2mm) structures in a single mold. The microbioreactors have a 100μL working volume, a high oxygen transfer rate ($k_L a \approx 0.1 s^{-1}$), and closed loop control over dissolved oxygen and pH ($\pm$ 0.1). Overall, the system supports eight simultaneous batch cultures, in two parallel arrays, with two dissolved oxygen thresholds, individual pH set points, and automated near real-time monitoring of optical density, dissolved oxygen concentration, and pH.

These capabilities allowed the demonstration of multiple *Escherichia coli* aerobic fermentations to high cell densities (>13g-dcw/L), with individual bioreactor performance on par with bench scale stirred tank bioreactors. The successful integration of diverse microfluidic devices and optical sensors in a scalable architecture opens a new pathway for continued development of parallel bioreactor systems.

Thesis Supervisor: Rajeev J. Ram
Title: Associate Professor

Acknowledgments

In the time that I have spent at the MIT, I have been fortunate to know and work with extraordinary people that have had a big impact on my life and graduate career. First and foremost is my advisor Prof. Rajeev Ram whose insight into problems, constant curiosity, positive outlook, and support throughout the years have been invaluable. The research group he created has been an ideal environment to learn, live, and chase after ideas. A big part of that has been the people in the group that I have had the privilege of working with and would like to thank. From the orignal crop: Mathew Abraham for your sense of humor and sharing your thoughts on the world; Erwin Lau for your free spirit; Steve Patterson for sharing your experience, wisdom (now I know), and setting a good example; Kevin Pipe for all the pizzas, late night company, and fun experiences outside of the lab; Farhan Rana for your quiet confidence, big grin, and example of the possibilities of a disciplined mind; Holger Schmidt for sharing your insights into research and the occasional tennis match; Fatih Yanik for your enthusiasm and carefree spirit; and Margaret Wang for your warmth and humor. From current or recent group members: Reja Amatya for your calm presense and nonchalantly drinking the habanero martini; Katie Butler for your outgoing nature; Elizabeth Bruce for your pleasant smile; Gustavo Gil for all the laughs, sharing your outlook on life, and playing catch with the football; Brian Goldberg for your cheerfullness and good nature; Xiaoyun Guo for your pleasantness; Kevin Lee for tolerating a disaster of an office and your hardwork and enthusiasm; Tom Liptay for sharing your thoughts on life and business, showing the value of disciplined thought, and all the spots for the bench; Peter Mayer for sharing your knowledge and being a great sounding board for all things; Jason Orcutt for reminding me how it was like at the beginning; and Tauhid Zaman for being himself.

This work would not have been possible without the advice and support Prof. Klavs Jensen and Prof. Anthony Sinskey and their research group members, with whom I worked closely to define the scope of the project. Paolo Boccazzi deserves special thanks for his efforts, unbridled enthusiasm, and teaching me the ways of a microbiologist. Funding was generously provided by the Dupont-MIT alliance and Helen Conon, Glen Gallahger, and

Dave Kraynie deserve thanks for their efforts in defining the needs of the project. I also want to thank my thesis committee members Prof. Marty Schmidt and Prof. Todd Thorsen for taking the time to provide feedback and guidance. In addition, I would like to thank the staff at the RLE, in particular Maxine Samuels, Lorraine Simmons, Dave Foss, Al McGurl, Mary Young, and Rose Rizzo, and our secretary Cathy Bourgeios for making all of the things that happen behind the scenes go smoothly; Fred Cote for managing the student shop; John, Steve, and Nancy for taking care of place and for late night conversation; and Anna's Taqueria for for feeding me.

Outside of the lab, I would like to acknowledge my friends and family, including my mom and brother who have been behind me; the denizens of the fourth floor of building 26; the MTL tennis team, especially Andy and Albert for all the tennis balls we've hit; the MIT Euchre club for providing an outlet Thursday nights; and Team Balico - Baruch, Jimmy, and Kathy - for making 2005 a great year.

A few individuals deserve special thanks for listening, eating, and talking during those times when you really need those things. Travis Simpkins for you candor and genuinely good nature, always taking the time to throw the football, and making me feel like part of your family; Kevin Pipe for making me push the envelope to the point of vomitting and being like a brother to me; Kathy Sienko for all the laughs, burgers, and for basically being my best buddy; and Olivia for the time we had together. My life is definately better having known you guys and I can only hope that in some small way it works the other way around too.

Contents

List of Figures

List of Tables

Chapter 1

Introduction

Bioprocesses with microbial cells play an important role in producing biopharmaceuticals such as human insulin[6] and human growth hormone[7], and other products such as amino acids[8], and biopolymers[9]. Because a bioprocess involves the complicated interaction between the genetics of the microorganisms and their chemical and environmental conditions, hundreds or thousands of microbial growth experiments are necessary to develop and optimize bioprocesses[10]. In addition, efforts to develop sophisticated models[11] that may allow rational design of bioprocesses also require numerous growth experiments to study microorganism phenotypes.

With the exception of recently developed disposable bag technologies for animal cell culture[12], the experimental biologist has relied on tried and tested shake flask and stirred tank bioreactors, accepting their inherent limitations in performance or throughput. While conventional high throughput methods, such as shaken microtiter plates or flasks, offer the advantage of high parallelism, they suffer from a lack of control over pH and low oxygen transfer capacity. In contrast, bench scale stirred tank bioreactors offer full control over culture conditions and high oxygen transfer capacity; however these systems are inconvenient and costly to operate in parallel. Experiments to optimize growth conditions, screen for desired phenotypes, or to validate the predictive power of a model under different growth conditions, would benefit from a technology that offers the parallelism of high through-

put methods, with the control capability and high oxygen transfer rate of the bench scale bioreactor[13].

In this work, we describe the design and development of an microbioreactor array that offers the high performance of a stirred tank bioreactor in a high throughput format. This was enabled by the development and integration of fluidic devices for mixing and fluid injection using a novel microfabrication process. In contrast to direct miniaturization of stirred tank bioreactors, this approach offers new avenues for scaling the number pH and dissolved oxygen controlled parallel bioreactors without the use of mechanical multiplexing or robotic systems. Continued development of this microfabricated approach has the potential to realize economically scalable, fully controlled, parallel bioreactor array systems that will benefit bioprocess development and microbial model development.

1.1 Experimental Microbiology

Cell culture is fundamental to experimental microbiology to observe microorganism phenotypes, which can range from the concentration of intracellular or extracellular metabolites, the oxygen uptake rate, biomass produced, or gene expression. To grow cells, nutrients, including sources of energy, carbon, nitrogen and phosphorous, along with trace metals that are incorporated into enzymes must be provided. This can be in the form of complex media derived from yeast extract, or simple sugars and salts with the appropriate elemental composition. In addition, the culture temperature and pH should be controlled in a range where enzyme activity is optimal and sufficient oxygen provided for respiration if aerobic microorganisms are grown.

As will be described in Sec. 1.2, there are a variety of cell culture technologies at the disposal of the experimental microbiologist, and also different ways to utilize them. Microbial cell culture can be categorized into three modes of operation, batch, fed-batch, and continuous. In batch culture, all of the nutrients are added initially and nothing is added to the fermentation medium, except oxygen, and perhaps base to control the pH. In fed-batch culture, nutrients are added to replentish nutrients consumed by the cells as the cells grow,

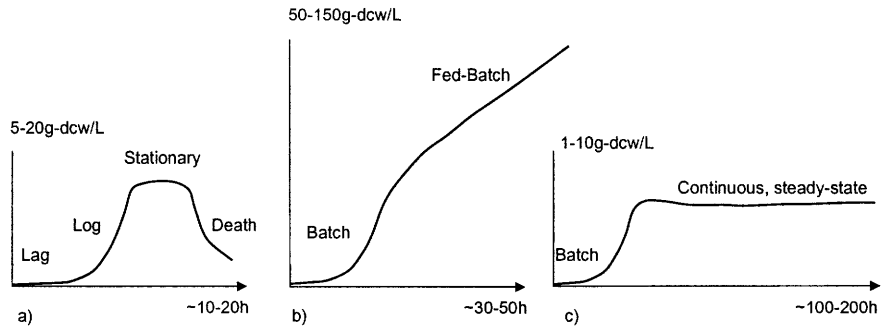

Figure 1-1: Schematic growth curves for a) batch, b) fed-batch, and c) continuous mode culture. Axes indicate typical times and cell densities. Batch cultures exhibit a lag-phase where cells are adjusting to their environment, exponential growth phase, stationary phase where growth stops but metabolism continues, and death phase when all nutrients are exhausted. Fed-batch cultures typically start with a batch growth, after which growth is limited by substrate feeding. In this example, a constant feed rate is illustrated, leading to linear growth. Continuous cultures typically have an initial batch growth while the starting nutrients are consumed and steady state is achived after tens of hours.

and nothing is removed from the bioreactor. In continuous culture, nutrients are continuously added to the medium and the same amount of the culture is continuously removed to maintain a constant volume. Fig. 1-1 illustrates typical biomass vs. time curves for the three types of culture.

Batch culture is the simplest and most often used mode of operation to generate biomass or products, and also to quickly screen strains and medium composition. However, because high concentrations of nutrients can inhibit growth[14], fed-batch culture is more frequently used in industrial bacteria fermentations to achieve high cell density, because it allows lower initial concentrations of nutrients and control over the bacteria growth rate through the nutrient feed. Both of these modes play a significant role in bioprocess development as described in Sec. 1.1.1 while continuous culture, which supports cell growth in steady state, is very useful for studying metabolism and model development as described in Sec. 1.1.2 because the data can be most easily related to mathematical models.

1.1.1 Industrial bioprocess development

For industrial bioprocess development, the primary objective is often to maximize the volumetric productivity of the fermentation, meaning to extract the maximum amount of product per unit volume per unit time. This is important because capital equipment cost and downstream product extraction and purification operations scale with volume[15]. Factors impacting the volumetric productivity are the specific product yield, which is the efficiency of bioconversion of nutrients to products per cell, and also the total biomass titer or cell density. Factors that influence the yield and titer are the genetics of the microorganism and also the external environmental conditions, which include nutrient composition, temperature, pH, dissolved oxygen concentration, and the time course of any chemical signals used to trigger product production[16],[17].

Genetic engineering techniques maintain a significant random component, where attempted modifications of the genetic material are performed on populations of microorganisms and successful modifications are selected, or screened from the population. Even with deterministic genetic modification techniques, our understanding is not at the point where the effect of these modifications could be predicted *a priori*, and screening experiments would still need to be performed.

Such screening can occur on multiple levels, from simply a yes/no on agar plates indicating whether the genetic material is incorporated non-fatally, to identifying which strains produce the most product in a small scale liquid culture with varying nutrient composition. Such a combined protocol of strain selection with medium optimization can lead to thousands of experiments that must be performed, which can take 1-3 years and thousands of man-hours to perform[10].

Even after such strain selection and medium optimization at a small scale, surprises can be in store at the industrial scale due to non-ideal mixing conditions and inhomogeneous conditions within the bioreactor, not encountered during small scale optimization[18]. These inhomogeneities induce stress responses in the microorganisms due to periodic oxygen starvation as mixing brings them to the top of the bioreactor and glucose starvation

as mixing brings them near the bottom, which can significantly effect product yield. In addition high-cell density growth at the industrial scale can lead to the accumulation of inhibitory byproducts such as acetate[19], which would not be encountered during screening if done at low cell densities and therefore, do not factor in the robustness of the strains.

An obvious solution to such problems would be to perform strain selection and medium optimization under conditions that simulate the environment of an industrial scale reactor. However, as will be discussed in Sec. 1.3 this is not practical using conventional cell culture technologies.

1.1.2 Systems biology modeling of microorganisms

The emergence of genome sequencing technologies as well as micro-array technology for high-throughput gene expression experiments has led to an effort to develop systems level models for microorganisms that attempt to capture the functioning of metabolic and regulatory networks defined by their genetics[20].

Steady state analysis of microorganism metabolism through stoichiometric bookkeeping based on known or inferred biochemical reactions occuring as part of cellular metabolism, known as metabolic flux balancing or analysis (MFA)[21], has been quite successful in predicting the effect of gene knockouts *in silico*[11] and has demonstrated the ability to model growth curves and substrate and byproduct formation rates, in agreement with batch growth experiments [22]. Such analysis has formed the basis for metabolic engineering[23], where the metabolic network for a microorganism is treated as a whole and modified to improve the production of a desired product.

1.2 Cell Culture Technologies and Capabilities

1.2.1 *Esherichia coli*

Esherichia coli (*E. coli*) is one of the most widely studied bacteria species and has served as the workhorse of biprocess industry. Its culture requirements and growth characteristics

will be outlined here to serve as a bench mark for the type of capability a bioreactor system should support.

For a typical *E. coli.* aerobic fermentation, the main nutrient is glucose which serves as a carbon and energy source. The optimal (fastest) growth temperature is 37°C, and the optimal pH is 6.9-7.0. The overall oxygenation requirement can be estimated from typical oxygen uptake rates of 20mmol/g/h[24] or 5.6×10^{-15} mol/cell/h for exponential growth on glucose, unlimited by other nutrients. For a maximum cell density of 2×10^{11} cells/mL (56g-dcw/L), representative of high cell density cultures, this translates to an oxygen uptake rate (OUR) of 1.1 mol/L/hr.

Under oxygen starvation, *E. coli* grows anerobically, with slower growth rate, in a mixed-acid fermentation where glucose is converted into acetate, formate, lactate, and ethanol [22]. In general, this condition should be avoided because energetically, growth without oxygen is theoretically 18 times less efficient and product yield is reduced.

Even during aerobic growth, *E. coli* is known to produce acetate under excess glucose conditions. It is hypothesized that this is due to an oxidation bottleneck in the TCA cycle leads to shunting of Acetyl-CoA from glycolysis and oxidative decarboxylation into a pathway that makes acetate[25]. Because acetate is known to inhibit recombinant protein production[14], prevention of acetate accumulation through fed-batch fermentation is typical for high cell density fermentation.

1.2.2 Oxygen transfer characterization

The oxygen transfer rate in cell culture systems is often characterized by the oxygen transfer coefficient, $k_L a$, which comes from the following space averaged, first order model for oxygen transfer that will be discussed in more detail in Sec. 2.2.1.

$$\frac{dC}{dt} = k_L a(C^* - C) - OUR \tag{1.1}$$

where C is the dissolved oxygen concentration in the medium and C^* is the saturation concentration in the medium. In steady state, the k_La satisfies

$$k_La = OUR/(C^* - C) \tag{1.2}$$

which for an OUR = 1.1 mol/L/hr and C^* = 0.21mmol/L (pure water in equilibrium with air at 37°C) at the threshold of oxygen limitation $C = 0$, gives k_La = 5600/hr = 1.6/s. C^* depends on the partial pressure of oxygen in the gas phase following Henry's law[26]. For pure oxygen, the required k_La to support 56 g-dcw/L would be $0.32s^{-1}$. Oxygen solubility also depends on the medium composition and is typically lower for fermentation media (10-15%) than pure water[27], therefore, comparisons of k_La values between different fermentations to follow are approximate.

1.2.3 Conventional cell culture technologies

Conventional microbial cell culture technologies are shown in Fig. 1-2 and include shaken microtiter plates, shake flasks, bench scale stirred tank bioreactors, and pilot-scale stirred tank bioreactors.

Mictrotiter plates

Microtiter plates rectangular plates of standard size (127.5 × 85.5 × 13.5mm), for interfacing with laboratory robotics, that are commonly composed of 24, 48, or 96 wells with volumes spanning 2mL, 1mL and 200μL, depending on the depth of the well. They are typically used for biochemical assays but are suitable for cell culture if shaken on a rotary table, and have recently drawn a lot of interest [28],[29] due to their high throughput format.

A wide range of oxygen transfer capacities can be achieved by changing the shaking conditions. For no shaking, or gentle shaking (<400rpm, 12.5mm diameter), which is actually quite typical, the oxygen transfer coefficient, k_La = 0.01 s^{-1}. With more vigorous shaking, of standard microtiter plates, k_La up to $0.05s^{-1}$) is achievable [28] and for round

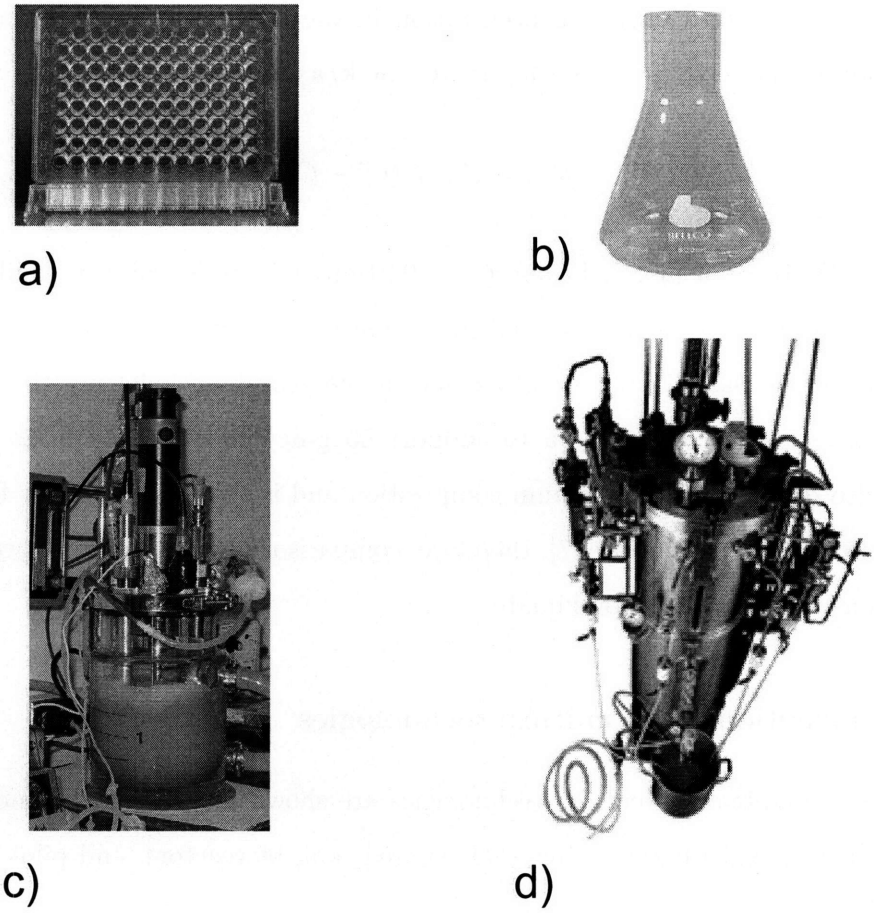

Figure 1-2: Experimental platforms for bioprocess development. a) Shaken microtiter plates, b) Shake flasks, c) Bench scale stirred tank bioreactor, d) Pilot-scale stirred tank bioreactor.

or square deep-well (height/width ratio = 4) plates, k_La as high as $0.26s^{-1}$ is possible. However, this mode of operation is non-standard and requires careful measures to prevent cross contamination and evaporation, including the use of special covers and operation in a humidified environment [29]. In addition, the inability to acquire data without suspending the shaking, and thereby introducing oxygen starvation, generally limits microtiter plate experiments to those with simple endpoint assays, such as how much product is produced under a given medium composition, or which strains grow to the highest cell density on a given medium.

Shake Flasks

Shake flasks are Erlenmeyer flasks of various volumes, typically 200mL with 50mL working volume, and shaken on a rotary shaker in batches of 10-20 flasks per shaker. Shake flasks have oxygen transfer capacity similar to shaken microtiter plates[30] with k_La up to $0.05s^{-1}$, however their larger size allows for more experimental flexibility to take samples and is also more convenient for adding instrumentation to measure culture parameters [31] or even accomplish substrate feeding and pH control[32]. However, shake flasks suffer from similar problems as shaken microtiter plates as any interruption of shaking almost immediately leads to oxygen starvation.

Bench scale stirred tank bioreactors

The bench scale stirred tank bioreactor approximates a large industrial scale bioreactor in its functional components such as impellers to stir the culture, temperature, pH, and dissolved oxygen sensors, a pH control system, and ports to inject substrates or remove samples. Its performance is actually superior to an industrial scale reactor, providing oxygen transfer rates corresponding to a k_La of up to $0.5s^{-1}$ due to better mixing on the smaller 2-10L scale, leading to a more homogeneous culture. It can be operated in all three modes, batch, fed-batch, and continuous and in addition, it can be operated as a closed system by monitoring the composition of the exit gas, allowing calculation of material balances, upon analysis of the culture medium.

Because of the capabilities of the stirred tank bioreactor, it is the system of choice for detailed studies of bioprocess characteristics and microorganism metabolism. It can also be used to simulate inhomogeneous conditions inside an industrial scale bioreactor by combining it with a plug flow reactor where culture medium is periodically pumped through a recycling loop into the plug flow section where starvation conditions can be induced[33]. The main drawback for the stirred tank bioreactor is the physical and psychological difficulty in performing many experiments in parallel.

1.3 Limitations of conventional culture technologies

Microtiter plates, shake flasks, and bench scale bioreactors all have different capabilities and corresponding effort to operate per experiment as summarized in Table 1.1. Cell culture

	Experiments per week	O_2 Transfer Rate Mass transfer coeff. k_La O_2 Limited Cell Density	Available Analysis	# Operating Protocols/ Control
Microtiter plate	10,000	OTR=0.007 mol/L/h k_La=0.01/s OLCD=0.36 g-dcw/L	End point yes/no	One, open loop
Shaken Microtiter plate		OTR=0.03 mol/L/h k_La=0.04/s OLCD=1.4 g-dcw/L		
Shake Flask	100	OTR=0.035 mol/L/h k_La=0.05/s OLCD=1.8 g-dcw/L	Time Series, no material balance	One, or two open loop
Bench Scale Bioreactor	4	OTR=0.35 mol/L/h k_La=0.49/s OLCD=18 g-dcw/L	Time series, material balances	Multiple, closed loop
With pure oxygen		OTR=1.5 mol/L/h k_La=0.49/s OLCD=76 g-dcw/L		

Table 1.1: Summary of bioprocess development tools

technologies with the most capability, bench scale bioreactors require the most effort to setup and operate and therefore have the lowest throughput, or number of experiments per man-week, while microtiter plates have the least capability.

In designing their experiments, microbiologists must trade off the quality and utility of the expected data with the effort to obtain that data. For bioprocess development, this typically results in an experimental chain where microtiter plates are used to identify and select the most promising strains based on an endpoint growth experiment. Then, candidates are grown in a series of shake flask experiments where some medium variations are explored. The most promising combinations are then used as initial starting points in bench scale stirred tank experiments.

This last step is particularly daunting because shake flask experiments do not provide

guidance on what the setpoints of the closed loop controlled parameters should be, nor how the microbes will be have under different medium compositions when those parameters are controlled. Thus, an entirely new family of optimization experiments needs to be performed to optimize a bioprocess, using the most inconvenient to use cell culture technology. When the objective is to optimize performance at high cell density, it is essential to provide closed loop controlled conditions.

1.4 Previous work

The limitations described in the previous section have of course been recognized by others and there has been a considerable amount of work to improve the throughput and capability of cell culture systems. This includes both commercial systems and academic efforts.

1.4.1 Commercial systems

Commercial systems include those based on improving the parallelism of stirred tank bioreactors, and one based on improving the capability of shaken microtiter plates. Parallel miniature stirred tank approaches include the Sixfors and Profors by Infors and the Cell Station by Fluorometrix. While a closed loop controlled microtiter plate approach, the μ-24 Bioreactor, has been introduced by Applikon. Characteristics of these systems are summarized in Table 1.2

1.4.2 Academic research systems

Recent efforts to address this need have focused on improving the capabilities of microtiter plates[29] or shake flasks[32], improving the parallelism of the stirred tank bioreactors[2],[3], or developing microfabricated bioreactor systems [34],[1],[4]. Each of these approaches have addressed parallelism, oxygenation, control, automation, and scalability to various degrees.

Manufacturer System (Parallelism)	Working Volume	Sensor Technology	Controlled Parameters (method)	Limitations
Infors Sixfors (6)	500mL	Standard Amperometric	pH, DO (agitation), Temperature	Inconvenient, Not scalable, No cell density Measurement
DASGIP Fed-batch Pro (4-16)	100mL	Standard Amperometric	pH, DO (agitation), Temperature	Inconvenient, No cell density Measurement
Infors Profors (16-32)	100mL	Standard Amperometric	pH, DO (agitation), Temperature	Inconvenient, No cell density Measurement
Fluorometrix Cell Station (12)	10mL	Optical pH, DO Optical Density	DO (agitation) Temperature (optional)	No pH control, Low cell density measurement
Applikon μ-24 Bioreactor (24)	1-5mL	Optical pH, DO	pH, DO (gas mix) Temperature	pH control with NH_3, No cell density Measurement
Bioprocessors SimCell (up to 1512)	0.5-1mL (est)	Optical pH, DO Optical Density	pH, DO (gas mix) Temperature Shear (rotation)	4 × 5 m room, Robotic equipment, At-line Measurements

Table 1.2: Overview of commercial parallel bioreactor systems.

Enahanced plates and flasks

Shaken deep 96 well microtiter plates have proven useful for screening a large number of strains[29] and provided oxygenation rates corresponding to an oxygen transfer coefficient, or k_La, of $0.05s^{-1}$. However, the pH and DO were not measured or controlled and manual sampling was required for optical density measurements.

Shake flasks with substrate feeding systems based on an array of pinch valves[32] have allowed 9 simultaneous pH controlled fed-batch growth experiments, where *E. coli* was grown to a cell density of 5.8g-dry cell weight/L (g-dcw/L). Similarly, parallel bubble columns[17] which provided improved oxygen transfer rate (k_La up to $0.16s^{-1}$), and used the same

substrate feeding mechanism allowed 12 simultaneous pH controlled fed-batch *E. coli* fermentations, and achieved a maximum cell density of 8g-dcw/L. However, with these system, manual sampling was required for optical density measurements.

Miniature stirred tanks

A miniature stirred tank bioreactor with motor driven impellers, and online optical pH, DO, and OD sensors[35] provided a k_La up to $0.1s^{-1}$ and was able to support growth of *E. coli* in batch culture to 1.4 g-dcw/L. However, this system was limited by lack of pH control. Also, only a single reactor was demonstrated due to the difficulty in scaling such a mechanically complicated reactor.

A single stirred and sparged cuvette[36], with 1mL working volume, that utilized online optical OD, DO, and pH sensors provided a k_La up to $0.012s^{-1}$ and supported batch growth of *E. coli* cell to an estimated 2g-dcw/L. Inefficient stirring and lack of pH control limited the performance of this reactor, although results were similar to a 1L stirred tank operated under similar conditions. An extension of this work, in the form of a 24 reactor rectangular array or carousel[2] of more sophisticated 1mL working volume reactors was recently demonstrated. It utilized individually motor driven impellers and integrated optical sensors for pH and dissolved oxygen, however there was no pH control and the optical density data was inconsistent with measured DO and pH profiles.

A system with 7 miniature stirred tank bioreactors[3] with 10mL working volume and high performance gas-inducing impellers that provided oxygen transfer coefficients of $0.22s^{-1}$ was recently demonstrated[37]. Dissolved oxygen was measured on-line with integrated optical sensors while pH and optical density were measured by robotically pipetting samples into microtiter plates and analysis with a plate reader. Robotic pipetting was also used for pH control and substrate feeding, which resulted in a very high performance system that allowed fed-batch growth of *E. coli* to 37g-dcw/L.

Microfabricated approaches

While continued improvements in the systems cited in Sec. 1.4.2 above provide a straightforward path to a parallel, fully controlled, and automated bioreactor system, their overall mechanical complexity could limit their ultimate scalability. For this reason, researchers have turned to microfabricated approaches under the premise that microfabrication techniques will allow batch fabrication of complicated mechanical functionality, leading to more inexpensive and easily scalable systems.

A hybrid approach combined an array of electrolytic gas generators, integrated ion-sensitive field-effect transistor (ISFET) pH sensors, LEDs and photodetectors for OD measurement, and heaters/thermistors for temperature control, on a single printed circuit board that was interfaced with two eight well microplate strips to form eight reactors[1]. Mixing was performed by shaking with a ball bearing introduced into the reactor. In this system, oxygen transfer rates equivalent to a k_La of $0.04s^{-1}$ were demonstrated along with batch growth of *E. coli* to an estimated cell density of 0.5g-dcw/L. pH control was not implemented, although a pH manipulation with electrolytically generated CO_2 was demonstrated.

A membrane aerated bioreactor[34] with working volume between 5μL and 50μL was fabricated out of polydimethylsiloxane (PDMS) with integrated optical pH and DO sensors. Online optical density measurements were reliable due to the short optical path length, and results for *E. coli* batch fermentations were shown to be reproducible and comparable to stirred tanks operated with the same k_La of $0.02s^{-1}$. This system supported growth to approximately 2.7g-dcw/L and provided sufficient cell biomass for cDNA microarray experiments[38]. However, there was no pH or DO control capability and only single reactors, were operated at one time.

As an extension of this work four computer numeric controlled (CNC) machined, magnetically stirred, polymethylmethacrylate (PMMA) reactors[39] with working volume of 150μL were mechanically multiplexed[4] using a translating optical head. Repeatable, simultaneous batch growth of *E. coli* up to a cell density of approximately 2.9g-dcw/L, with

an estimated $k_L a$ of $0.04 s^{-1}$ was demonstrated, however, there was no pH or DO control, and the mechanical multiplexing did not take advantage of scaling through batch fabrication.

1.5 Shortcomings of previous approaches

From Sec. 1.3 we saw the key problem to solve was to provide the capabilities of a bench scale stirred tank bioreactor, including a high oxygen transfer rate with pH and dissolved oxygen control, with parallelism on par with shake flasks. In addition ease of use, and cost effectiveness were considerations.

1.5.1 Miniature stirred tanks

Approaches based on miniature stirred tanks, including most of the commercial offerings, are fabricated using conventional manufacturing technologies and have a well defined, but expensive path to scaling to larger numbers of reactors. Simply shrinking a stirred tank and operating them at a common station only provides minimal economies of scale for setup effort. All reactors need to be cleaned and sterilized, sensors need calibration, and in most cases, samples need to be removed for optical density measurements. On-line optical density measurements in stirred tanks are not reliable for two reasons. First, in stirred tanks, in order to achieve a high oxygen transfer rate many small air bubbles need to be dispersed through the medium, which scatters light and therefore disrupts the optical density measurement. Second at high cell densities, unless the optical path length is very small and care is taken to reject scattered light, the optical density underestimates the cell density. Fluorescence based optical sensors are an improvement as they can generally be operated calibration free, if properly designed. pH control, while possible with conventional technologies, becomes expensive as the number of reactors scales and in commercial systems is typically only offered optionally.

1.5.2 Hybrid approaches

Well plate based technologies depending on robotic sampling and pipetting for measurements and pH control could prove to be the most functional solution, however, they require expensive robotic automation and have an increased probability of contamination and require operation in a sterile incubator to minimize evaporation[3].

The Applikon μ-24 Bioreactor, as a shaken microtiter plate with integrated sensors, has the most favorable combination of throughput and capability, having individual control over pH, DO, and temperature. However, no cell density measurements are offered, which is a key phenotype to monitor for process optimization.

1.5.3 Microfabricated bioreactors

Given the shortcomings and perceived limitations of extending the conventional cell culture technologies, academic researchers have looked to microfabricated approaches which promise scalability through batch fabrication of reactors. However these have proven difficult to implement in parallel and in general, fall short of the required oxygenation and pH controlled performance. Low oxygen transfer rate has been largely due to poor agitation in microliter scale devices, while lack of pH control has been due to the difficulty of integrating pH actuation devices and pH sensors. In addition, no authors have taken advantage of the batch fabrication characteristics of microfabricated approaches, integrating multiple controlled bioreactors in a single module.

1.5.4 Summary

Figures 1-3 and 1-4 summarize the notions in this chapter, where parallel bioreactor systems along with the conventional cell culture technologies are schematically displayed along dimensions of capability and throughput and capability and complexity. The former captures the functional characteristics that are required and the latter, the fabrication and scaling. Clearly, the desirable areas in the figures are the upper right corner of capability and throughput and the upper left corner of capability and complexity.

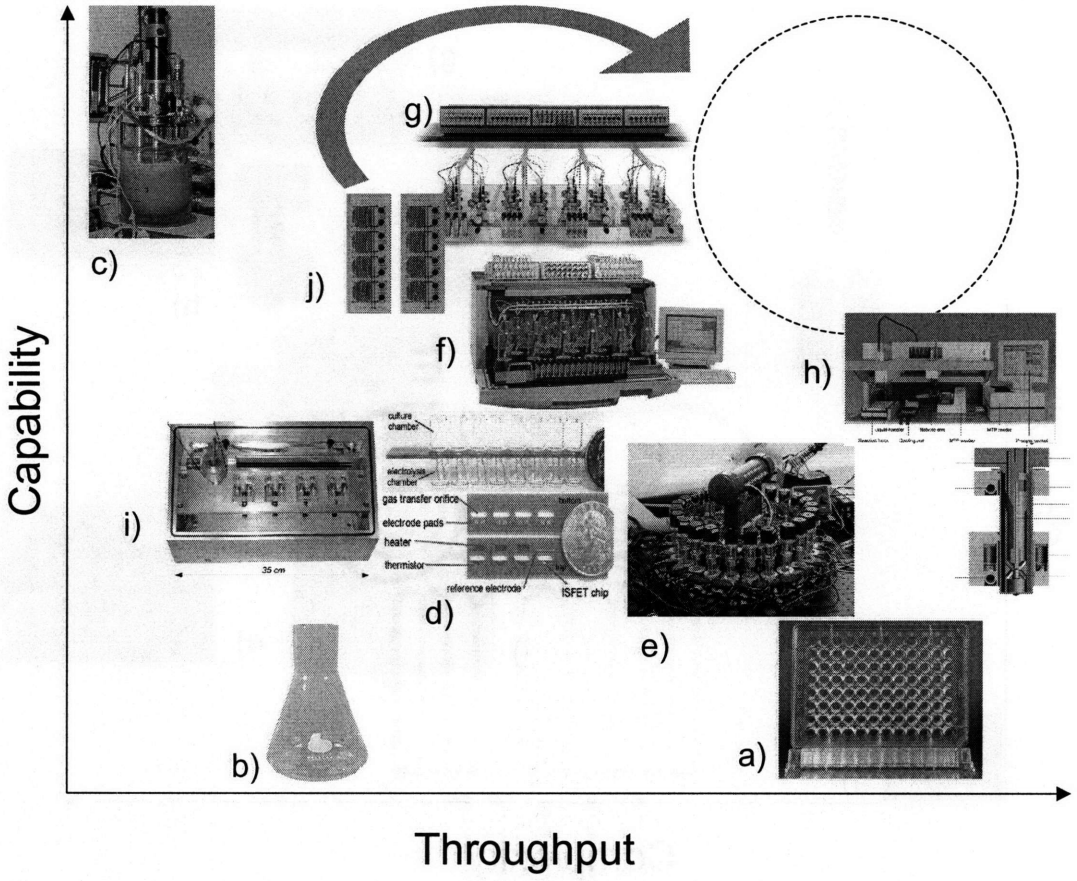

Figure 1-3: Capability vs. throughput for experimental platforms. a) Shaken microtiter plate, b) Shake flask, c) Bench scale stirred tank, d) Keasling[1] e) Rao[2] f) Infors Profors system, g) DASGIP Fed-batch Pro. h) Weuster-botz [3], i) Szita[4] j) Parallel integrated bioreactor array (this work).

1.6 Thesis preview

The approach taken in this thesis will be further exploration of microfabricated techniques, focusing on providing a high oxygen transfer rate, pH control, and parallel integration of multiple bioreactors in an easy to use package. The ultimate objective will be to deliver the required performance without resorting to expensive robotic automation, which is being pursued by other researchers.

Chapter 2 will describe the design tradeoffs in the overall system, Chapter 3 will de-

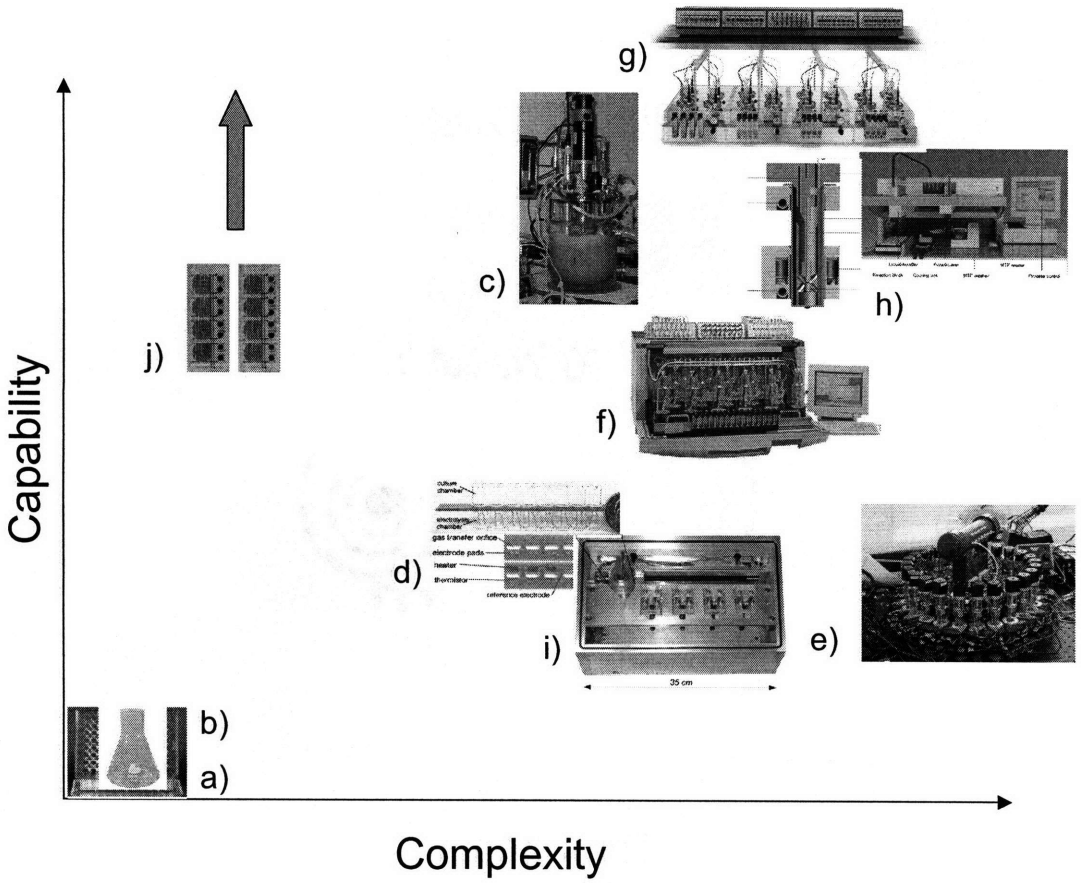

Figure 1-4: Capability vs. complexity for experimental platforms. a) Shaken microtiter plate, b) Shake flask, c) Bench scale stirred tank, d) Keasling[1] e) Rao[2] f) Infors Profors system, g) DASGIP Fed-batch Pro. h) Weuster-botz [3], i) Szita[4] j) Parallel integrated bioreactor array (this work).

scribe the fabrication processes used to construct the integrated bioreactors, Chapter 4 will discuss the integrated devices and supporting subsystems that enable pH control, Chapter 5 will discuss the integrated devices and supporting subsystems that enable DO control, Chapter 6 will describe the overall architecture of the system in more detail, with particular attention being paid to scaling, Chapter 7 will present a series of fermentation experiments, and Chapter 8 will discuss future prospects of this technology and additional directions to pursue.

Chapter 2

System design

From Chapter 1 we recognized a large gap in the capability and throughput of current cell culture technologies, as indicated by the empty upper right quadrant of Fig. 1-3. While a number of research projects and commercial offerings seek to fill this gap with parallel cell culture systems, none have succeeded and furthermore, none have sought the exploit the full potential of microfabricated systems. In this chapter, we will discuss some of the properties of an ideal cell culture system, outline the design tradeoffs in a microfabricated bioreactor array system, and then finally present an overview of our bioreactor design.

2.1 Properties of an ideal cell culture system

If we could peer into the minds of microbiologists and see the cell culture technology of their dreams and fantasies, we expect that it would have the following properties, in approximate order of priority, relative to the limitations of current technologies.

1. Online, high frequency measurement of cell density.
2. Online, high frequency measurement of pH.
3. Online, high frequency measurement of DO.
4. Individual control over pH.

5. High oxygen transfer rate for aerobic growth to high (>10g-dcw/L) cell densities.
6. Low likelihood of contamination.
7. Effort to operate does not scale with number of reactors.
8. Easy to setup and operate. < 30 minutes setup, < 30 minutes conclusion.
9. Scalability to large number of reactors (64-128).
10. Individual control over Temperature.
11. Individual control over dissolved oxygen.
12. Individually controlled substrate feeding.
13. Online, high frequency measurement of CO_2.
14. Online, high frequency measurement of substrate.
15. Online, high frequency measurement of products.
16. Automated sampling for gene expression experiments.
17. Disposable or easily sterilizable.
18. Small volume, capable continuous fermentation.
19. Small physical footprint, low power.
20. Inexpensive to operate and maintain.
21. Cost of system does not scale with the number of bioreactors.

While dreams and fantasies provide objectives to strive for, realistically, they are beyond the reach of available technology and we strive to achieve the highest priority objectives.

Table 2.1 summarizes the abilities of existing systems discussed in Sec. 1.4.

2.2 Design rationale

One of our first decisions is to explore microfabricated approaches, due to the minimal efforts by other reserarchers in this area. The promise of inexpensive parallel fabrication of

Manufacturer/Author System (Parallelism)	Description	Achieved Properties
Infors Sixfors (6)	Miniature stirred tanks.	4, 6, 10, 11, 12
DASGIP Fed-batch Pro (4-16)	Miniature stirred tanks, Shake flasks	4, 6, 10, 11, 12
Infors Profors (16-32)	Miniature stirred bubble columns.	4, 5, 6, 12
Fluorometrix Cell Station (12)	Mini-stirred tanks, optical sensors.	1, 2, 3, 6, 7, 11, 17, 19
Applikon μ-24 Bioreactor (24)	Shaken microtiter plate. Gas bubbling pH, DO control.	2, 3, 4, 7, 8, 9, 10, 11, 17, 19, 20, 21
Bioprocessors SimCell (up to 1512)	Industrial scale microbioreactors. Robotic multiplexing	4, 6, 7, 8, 9, 12, 16, 17, 21
Duetz [29] (96)	Shaken microtiter deep well plate	5, 7, 8, 9, 17, 19, 20, 21
Weuster-Botz [40] (8-48)	stirred well plate array, robotic fluid handling.	3, 4, 5, 9, 12, 16, 18, 19, 21
Rao [2] (24)	carousel of mini stirred tanks. online optical sensors	1, 2, 3, 6, 11, 19
Keasling [1] (8)	shaken well plate strip, electrolytic gas generation	1, 2, 3, 6, 7, 10, 11, 17, 19, 20 21
Jensen [4] (4)	mechanically multiplxed microfabricated stirred disc.	1, 2, 3, 6, 18, 19, 20

Table 2.1: Summary of commercial and academic parallel bioreactor systems.

complex functions offered by microfabrication satisfies scalability and inexpensive fabrication requirements. In addition, a microfabricated approach offers the potential for future integration with chemical analysis tools to realize a biotech micro-total-analysis system.

The three dominant functional characteristics that need to be implemented in a bioreactor array system are pH control, a high oxygen transfer rate, and online measurement of the cell (optical) density. Attempting to meet these objectives in a microfabricated device leads to a flat form factor bioreactor that is actively mixed and also optically clear.

The flat form factor is important to achieve a high oxygen transfer rate and online measurement of optical density, which works well to high cell densities. The flat form factor results in a high surface area to volume ratio, which is favorable for surface aeration and is a proven[34] method for oxygenating a bacteria culture. In this case, no bubbles are required for high oxygenation and on-line optical density measurements can be implemented. In addition, the short optical path length leads to a larger range where the relationship between optical density and cell density is linear.

How flat should be bioreactor be? This can be answered by analyzing the oxygen transport in a flat bioreactor and examining optical transport in an optical density measurement.

2.2.1 Oxygen transport in bioreactors

For *E. coli* batch growth on glucose at 37°C, the oxygen demand is approximately 20mmol/g-dcw/hr [24]. For a high cell density culture (50g-dcw/L) the oxygen demand is 1 mol/L/hr or 0.28mmol/L/sec, which must be provided by the bioreactor to prevent oxygen limitation.

In conventional bioreactors, oxygen is dispersed throughout the culture by sparging air bubbles into the medium and mixing. Oxygen diffuses from the air bubble into the liquid which is homogeonized through mixing. This is typically modeled with a 0-D dynamic model as shown in Fig. 2-1a).

A stagnant liquid film surrounding the air bubble presents the diffusion barrier for

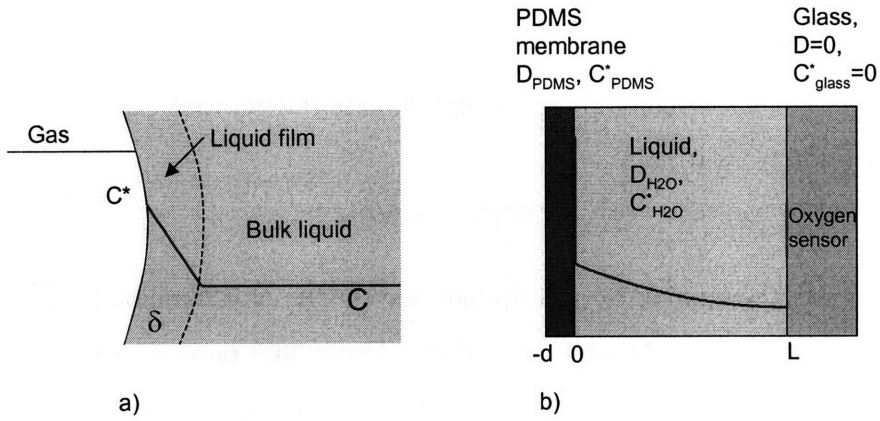

Figure 2-1: Schematic drawings of models used to calculate oxygen transfer coefficient. a) Oxygen diffusion from a bubble to the bulk liquid. Diffusion barrier is a stagnant liquid film. b) Oxygen diffusion through PDMS membrane into bulk liquid. The mixed region is modeled with an enhanced diffusion coefficient.

oxygen and the specific oxygen flux into the liquid is equal to

$$\frac{dC}{dt} = \frac{A}{V}\frac{D}{\delta}(C^* - C) \tag{2.1}$$

where A is the total surface area of the bubbles retained in the medium, D is the diffusion coefficient of oxygen in water, C^* is the saturation concentration of oxygen in water for the partial pressure of oxygen in the bubble, C is the average dissolved oxygen concentration in the bulk liquid, and δ is the thickness of the liquid film. Typically, $(A/V)D/\delta$ are combined into a parameter, k_La, the oxygen transfer coefficient, which depends on the stirring speed of the mixer, and the volumetric gas flow rate, which both effect the k_La through the specific surface area of the bubbles[26].

Using this film model, the dynamics of the oxygen concentration can be modeled with the following equation:

$$\frac{dC}{dt} = k_La(C^* - C) - OUR \tag{2.2}$$

where OUR is the specific oxygen uptake rate (mmol/L/s). $C^* = 0.21$mmol/L is the dissolved oxygen saturation concentration for water at 37°C in air ($p_{O_2} = 0.21$atm) and

can be up to 15% lower for growth media[27].

In steady state, the maximum oxygen uptake rate (OUR) that can be supported before oxygen limitation ($C \approx 0$) is

$$OUR_{max} = k_L a C^* \tag{2.3}$$

Thus, to support a maximum oxygen uptake rate (OUR) of 0.28mmol/L/s using air as the sparging gas, the $k_L a$ must be at least $1.33s^{-1}$. Using 50% pure oxygen, the $k_L a$ must be at least $0.53s^{-1}$, and using 100% pure oxygen, the $k_L a$ must be at least $0.27s^{-1}$. These requirements are relaxed somewhat in high cell density fed-batch cultures where the growth rate is slowed by reducing the feedrate, which is providing the growth limiting nutrients. In this situation, the oxygen demand is reduced.

2.2.2 Oxygen transport in microbioreactor

The oxygen transfer capacity for flat form factor surface aerated bioreactors can calculated by solving the diffusion equation 2.4 in steady state

$$\frac{\partial C}{\partial t} = \frac{\partial}{\partial z}\left(D(z)\frac{\partial C}{\partial z}\right) - OUR \tag{2.4}$$

for the geometry shown in Fig. 2-1b.

For a given OUR, the dissolved oxygen profile can be solved in closed form. We can arrive at a steady state $k_L a$, $k_L a_{ss}$ by calculating

$$k_L a_{ss} = OUR_{max}/C^* \tag{2.5}$$

as in Eq. 2.3, where OUR_{max} is defined as the oxygen uptake rate where the dissolved oxygen concentration equals zero at some point in the reactors. For the geometry in Fig. 2-1 this occurs at the bottom of the growth well at z=L. The $k_L a_{ss}$ is a function only of the

geometrical and physical parameters and can be expressed as:

$$k_L a_{ss} = \frac{1}{\frac{1}{k_L a_{mem}} + \frac{1}{k_L a_{diff}}} \tag{2.6}$$

where

$$k_L a_{mem} = \frac{D_p/K}{Ld} \tag{2.7}$$

$$k_L a_{diff} = \frac{2D_w}{L^2} \tag{2.8}$$

where D_p is the diffusion coefficient of oxygen in PDMS, D_w is the diffusion coefficient of oxygen in water, L is the depth of the growth well, d is the thickness of the membrane, and K is the partition coefficient, or the ratio of the dissolved oxygen saturations in water and PDMS.

Eq. 2.6 indicates that the total oxygen transfer coefficient is the parallel sum of the oxygen transfer coefficient due to the diffusion barrier provided by the membrane, and the diffusion through the water. $k_L a_{ss}$ and its components are plotted in Fig. 2-2. $k_L a_{ss}$ is dominated by the diffusion through the water. To achieve the 0.28 s^{-1} to support a 50g-dcw/L cell density using pure oxygen, a well depth of only 100μm is necessary. This is problematic because for a 100μL well volume, that is convenient for sampling and final analysis of the culture, an area of 3cm $\times$ 3cm would be necessary. This is an excessively large footprint that would make rapid lateral mixing necessary for pH control more difficult. Reducing the footprint to a more managable 1.5cm $\times$ 1.5cm would require a $500\mu m$ well depth. Unfortunately, the effective $k_L a$ for this well depth is only 0.015 s^{-1}, 18 times too small to support 50g-dcw/L.

Clearly, a strategy to reduce the diffusion barrier of the water is necessary. Mixing provides the answer since for the perfectly mixed case, the $k_L a$ will be equal to the contribution from the membrane alone, which is approximately equal to our target of 0.28 s^{-1} for a $500\mu m$ deep well. This highlights the importance of mixing in the parallel integrated

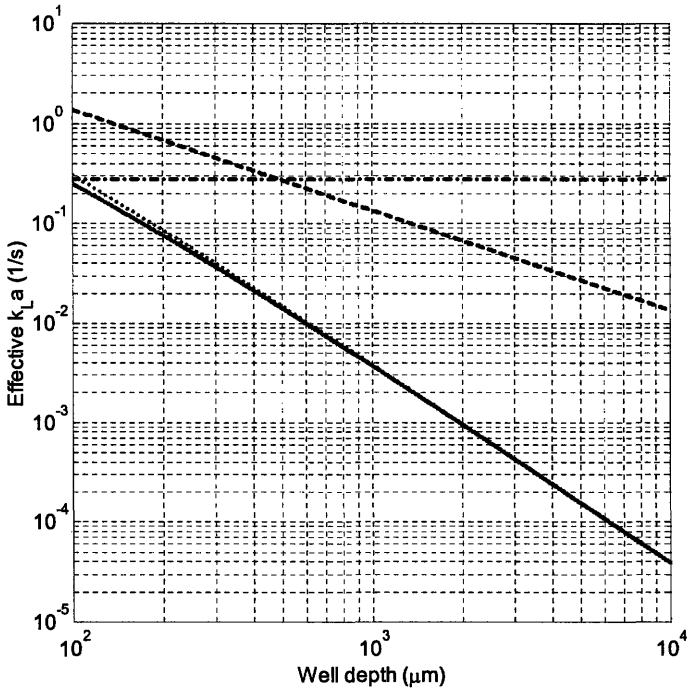

Figure 2-2: Theoretically calculated $k_L a_{ss}$ (solid) showing the contribution from a 60μm thick PDMS membrane (dashed), diffusion through water (dotted) for various well depths.

bioreactor array.

2.2.3 Mixing

Mixing is necessary for a number of reasons. First, because the optical sensors are local, and we would like their signal to represent the average value over the entire culture, we must ensure there are no inhomogeneities in the culture. Pure diffusion is two orders of magnitude (L^2/D = (1.5cm)^2/4.6 $\times$ 10^{-5}cm^2/s) = 13.6 hours) too slow and therefore in order for the local sensors to provide relevant information, the growth wells must be actively mixed. Second, because enzyme activity and gene expression is affected by pH, and the entire point of implementing pH control is for the cell culture to proceed under known conditions, large inhomogeneities in pH should not be allowed to persist. Therefore, for a pH control strategy based on local fluid injections, mixing is essential.

Additional reasons for implementing active mixing are, as will be discussed in more

detail in Chapter 5, the significant impact on the oxygen transfer rate, and also, the mechanical agitation of the cells that occurs inside stirred tank bioreactors can be important in determining cell morphology, and therefore can be important if the PIBA is to be used for scale up simulation[41].

Mixing in a flat form factor chamber is difficult to accomplish. Most microfluidic mixers in the literature are designed to mix fluids as the flow through a channel, which is a typical operation in a micro total analysis system. Examples are a mixer based on chaotic advection of the fluid as it flows through a microstructured channel [42], a serpentine channel mixer [43], a diffusive mixer[44], and a rotary mixer[45].

For mixing in a chamber, micro magnetic stirrers have been developed, however their fabrication is complicated[44],[39], and in addition, they require generating a rotating magnetic field to operate. This generally requires a permanent magnet and motor placed near the stirrer, which complicates the integration of other system components, such as optical sensor addressing.

Peristaltic mixer

One of the few examples of mixers designed to work in a chamber are peristaltic mixers, which have been analyzed [46],[47] and demonstrated with piezoelectricly or ultrasonically actuated membranes. Propagating waves along one wall of a chamber generates lateral and vertical flows in flat form factor chambers.

We are able to approximate this behavior using a series of deflectable membrane sections, which can be pressurized in a sequence to approximate peristaltic action. This method also has the additional advantage of improving the oxygen transfer rate, which will be discussed in more detail in Chapter 5. Fig. 2-3 shows the structure and function of a generic pneumatically driven membrane peristaltic mixer. There are seven tubes overlaying the growth well, which define seven membrane sections that can be deflected into the growth well. Because the membranes are supported at the edges of the growth well, the deflection of the tubes is incomplete at the edges and fluid can flow around the edges of the growth well

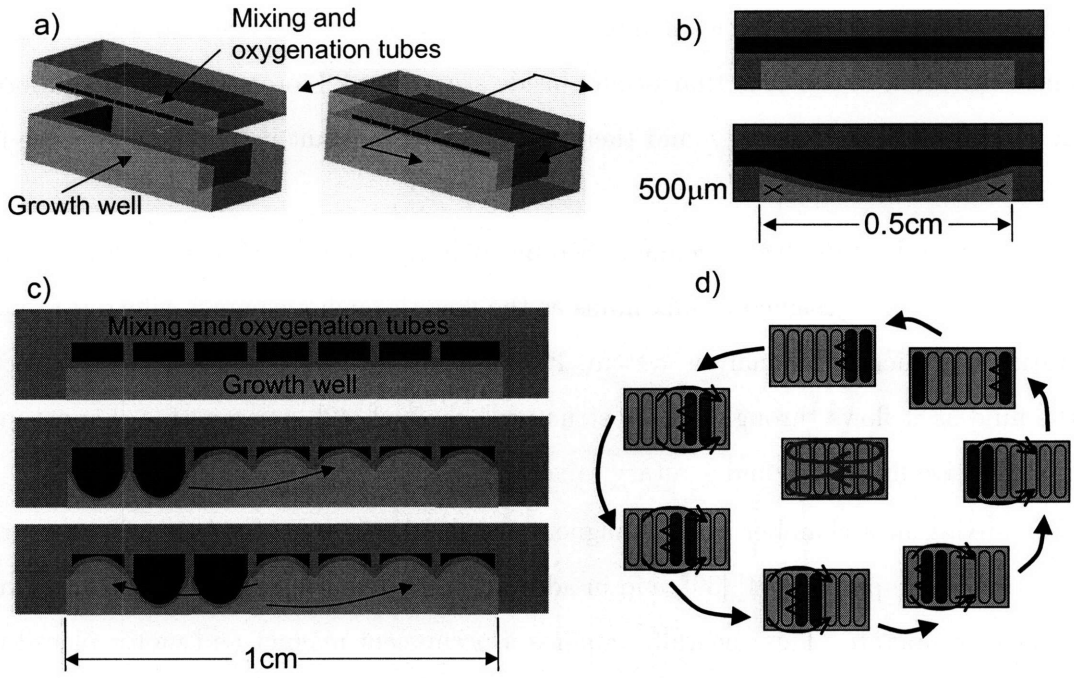

Figure 2-3: Schematic of generic peristaltic oxygenating mixer. a) Three dimensional view b) Cross-section along mixing tube. Unpressurized (top) and pressurized (bottom), note the deflection is more in the center and allows fluid flow around the edges. c) Cross-section across mixing tubes showing approximate peristalsis actuation pattern. d) Top view of peristalsis and approximate flow pattern.

(Fig. 2-3b) as the deflection pattern propagates. In this way, the propagating pressurization pattern drives fluid forward in the center of the growth well and back around the edges, generating a flow pattern with two circulation loops as shown in Fig. 2-3d.

Fig. 2-4 shows an early generation peristaltic mixer fabricated using a thick SU-8 process. The photograph shows eight growth wells integrated into a device that is sealed to a microscope slide. The image sequence shows the mixing of blue dye within the growth well and shows the long time required for diffusion to homogonize the well, and the mixing pattern that is approximately the same as predicted in Fig. 2-3d.

The last two frames also highlight a problem with the simple straight tube design. Because of the symmetry of the device and propagation pattern, in the form of a mirror plane through the center of each growth well, the fluid in the top and bottom half of the

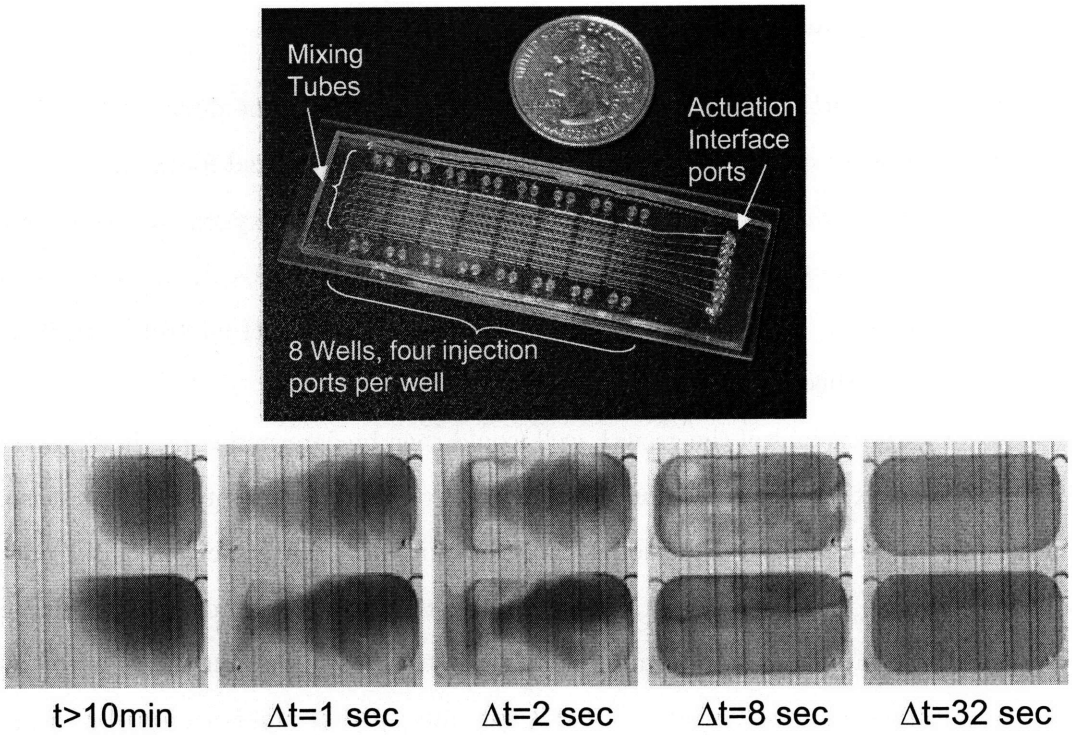

Figure 2-4: Photographs of first generation peristaltic oxygenating mixer fabricated using SU-8 photolithography. a) Eight mixers sealed to a microscope slide. b) Image sequence of two mixers showing fluid flow and mixing. Note the similarity of the flow pattern to the predicted pattern. Also note the the top and bottom half of the well does not mix together very well.

growth well will not mix together. In both growth wells, there is more dye in the top half because the initial injection ocurred in the upper right port. As a result, after mixing is complete, the top half of the well is clearly darker than the bottom half. This situation can be avoided by using non-uniform width mixing tubes to eliminate the symmetry as shown in Fig. 2-5. Tubes with varying width will have different amounts of deflection for a given actuation pressure, where the narrower regions will allow fluid to flow and generate fluid flow transverse to the peristalsis direction.

2.2.4 Size of growth well

At this point it is worth summarizing our options for the size of the device, which involves the interplay between oxygen transport, desired volume, and desired footprint.

From Sec. 2.2.2, theory indicates that for pure diffusion of oxygen, we would require a growth well thickness less than 100μm to achieve a k_La of 0.28 s^{-1}, needed to support 50g-dcw/L of *E. coli.* With mixing, which will be required for pH control, a thickness of less than 500μm is theoretically sufficient.

The lateral dimensions of the growth well would then be determined by the desired total volume, lateral mixing efficiency, and any physical constraints presented by the sensors to be described in Sec. 2.2.5. Additional considerations are the achievable fluid injection resolution, because for batch growth, it is preferable to keep the total change in volume due to any acid/base injections to a minimum. With injection volumes on the order of 100nL, using the injectors described in Sec. 4.3, and assuming a total number of injections on the order of 100, to keep the total volume change at less than 1% of the initial volume, would require an inital growth well volume of approximately 100μL, which is also comparable to the sample size that is convenient to work with in off-line chemical analysis.

The final consideration for the growth well size is the minimization of the footprint, whose motivation is related to the fabrication of the devices and the lateral mixing speed for homogenization of the pH. The lateral mixing time is expected to scale with the lateral dimensionis of the growth well, given similar fluid flow velocities generated by the mixer. Alignment between PDMS device layers is simply easier to accomplish with smaller overall devices, especially with the tendency of the flexible materials to distort as they are handled. Therefore, we strived for a 1.5cm $\times$ 1.5cm $\times$ 500μm growth well.

2.2.5 Sensors

The flat form factor and overall small volume also impacts the choice of sensor inside the bioreactor. Fluorescence quenching based sensors are chosen for their small size and equilibrium nature of their operation, meaning they do not consume or produce any byproducts

as part of their sensing mechanism. In addition, integrating optical sensors into the bioreactors was very simple. Oxygen sensors, made using Platinum-Octaethylporphyrine and polystyrene[48] on 5mm diameter glass disks were embedded into the device during molding and commercial pH sensors (Presens, HP5) were glued in place after demolding. An additional benefit of optical sensors was the simple optical interfacing through the optically clear devices. In addition, the optical access afforded by clear materials could also be important for future implementation of optical spectroscopies for chemical analysis[49].

For optical density measurements, the most serious deficiency of currently employed methods is their limited linearity. For optical density measurements to correspond to the cell density, an optical transmission measurement must only collect light that is not scattered at all, as any collection of scattered light will result in an apparently reduced optical density. This can be accomplished by satisfying two conditions. First, the optical thickness, defined by the product of the physical thickness and the total attenuation coefficient, must be less than 10. For optical thicknesses greater than ten, almost all light that passes through the sample will have undergone scattering. Second, the amount of scattered light reaching the photodetector must be minimized[50].

The first condition can be met by making the physical path length thin. For a 500μm thick device, to maintain the optical thickness less than ten, the optical density scaled to a 1cm path length must be less than 86, which would correspond to a cell density of approximately 28 g-dcw/L.

The second condition can be met by careful optical design to limit the numerical aperture collected by the photodetector and reducing the numerical aperture of the excitation beam. This is discussed further in Sec. 6.2.3.

Alternative sensors

Optical sensors, of course are not the only option for bioprocess sensing. For oxygen, micromachined Clark-type amperometric oxygen electrodes have been demonstrated [51],[52], pH, ion-sensitive field-effect transistors (ISFET) have been developed [53] and used in miniature

bioreactors [1], and for cell density, permitivity spectroscopy [54],[55],[56], to sense intact cells have been developed.

The Clark-type oxygen electrodes are not attractive for integration since they require careful packaging of an electrolyte solution and do not possess long term stability. Overall, these sensors do not provide any advantages over the optical oxygen sensors.

pH sensors based on ISFETs, however, do have some attractive properties. They can operate over a very large range of pH, unlike the optical sensors, and are therefore suitable for culturing microorganisms in a greater diversity of environments. In addition, being based on CMOS technology, they can be fabricated rather inexpensively. With these favorable properties and relatively simple operation, these sensors are good candidates for integration into future devices.

Permitivity based measurements to infer the cell density are based on the polarizability of intact cells. The proximity of viable cells to the electrodes of a capacitor will tend to increase its capacitance. These permitivity based measurements have the advantage of a wide linear range, unlike optical density measurements, where careful measures need to be taken to ensure linearity. In addition, the specific sensitivity to viable intact cells and tolerance of air bubbles provide some advantages over optical density based measurements. Such sensors, are however difficult to implement as permitivity measurements in the range of a few hundred kilohertz to a few megahertz are required, to account for the effects of medium conductivity on permitivity measurements.

2.2.6 Fabrication

The final structures of the devices to enable oxygenation, mixing, and fluid injection for pH control are intimitely related to the fabrication process used to make the device. Scalability dictates elements required for individual bioreactors should be batch fabricated and those elements that cannot be easily batch fabrictated should be shared or multiplexed as much as possible. Elements required for individual bioreactors include fluid injector valves, mixers, optical sensors, and waveguides.

In recent years, there has been a steady increase in the use of PDMS molding for microfluidic devices [57],[58],[59] due the ease of implementation and the opportunity to construct active devices by taking advantage of the material's compliance and pneumatic actuation[60],[61], [45]. Because of these favorable properties and the optical clarity of PDMS, we chose PDMS molding as the basis for our fabrication technology.

Because we required the integration of diverse types of devices, with multiple depths and profiles, we developed our own variation of a PDMS molding process that will be described in detail in Chap. 3.

2.3 Parallel Integrated Bioreactor Array (PIBA) overview

With the key drivers for the design of the microbioreactor array devices, and the basic approach for to meet our objectives, described in Sec. 2.2, we present the overall design of the parallel integrated bioreactor array system, including the microbioreactor array module, and the supporting subsystems that actuate the device. More details about the microbioreactor array module can be found in Chapters 4 and 5, while details about the supporting subsystems are in Chap. 6.

2.3.1 Integrated microbioreactor module

The PIBA is based around an integrated bioreactor array fabricated using a novel PDMS molding technique to be described in more detail in Chapter 3. It combines a peristaltic oxygenating mixer which provides mixing and enhanced oxygen transfer, with two fluid injectors to implement pH control and/or substrate feeding for fed-batch operation.

The molded PDMS device is interfaced to macroscopic subsystems which support shared pneumatic actuation resources, optical addressing of the optical sensors, pneumatic switch drive electronics, optical excitation and detection electronics, and the software to run the system.

A photograph of a module with four integrated reactors and a schematic and cross sectional view of the device is shown in Fig. 2-5

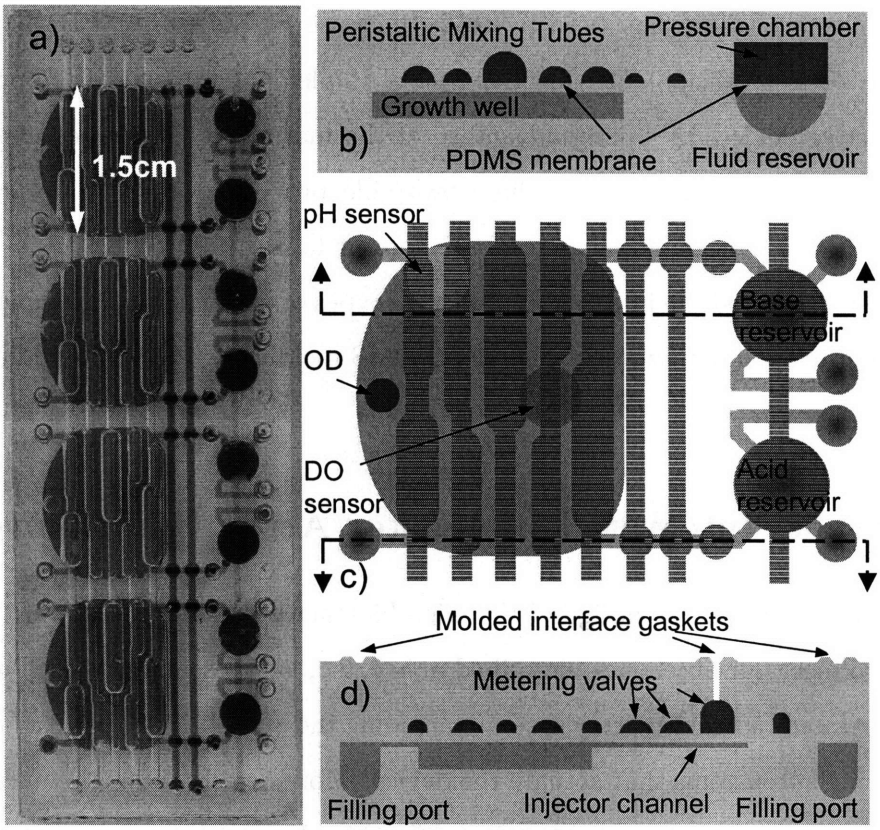

Figure 2-5: Photograph and schematic of Parallel Integrated Bioreactor Array device. a) Photograph of four reactors integrated into a single module. b) Cross-section showing peristaltic oxygenating mixer tubes and fluid reservoir with pressure chamber. c) Top view of schematic showing optical sensors and layout of peristaltic oxygenating mixer and fluid injectors. d) Cross-section showing the fluid injector membrane pinch valves.

The peristaltic oxygenating mixer is composed of a set of five deflectable membrane sections over the top of the growth well. Pressurizing the space, or tube, above the membrane section deflects it into the growth well. Pressurization in a sequence 00011, 00110, 01100, 11000, 10001, 00011, where 1 indicates pressurized and 0 indicates vented, approximates peristalsis inside the well, mixing the contents.

The fluid injectors are composed of a fluid reservoir and pressure reservoir, separated by a membrane, and three membrane pinch valves. A volume of fluid approximately equal to the total displacement volume of the center valve is injected per cycle, which is shown in

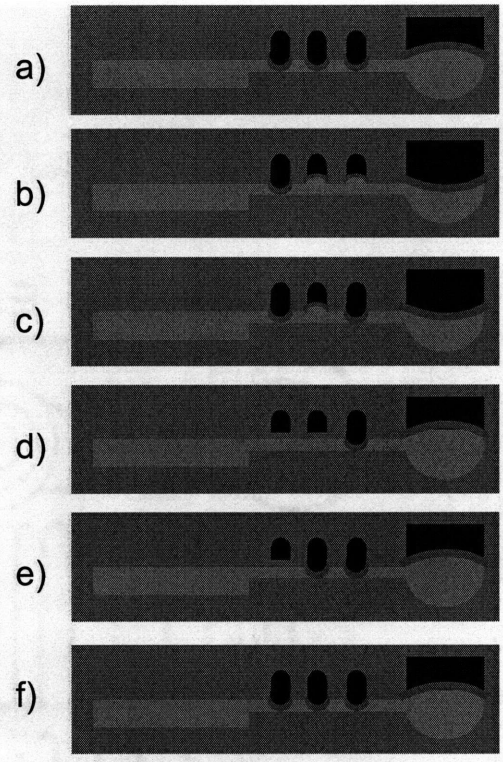

Figure 2-6: Fluid injector actuation sequence. a) Quiescent state. b) Load injector, pressurize reservoir, open all but last valve. c) Capture plug, close valve closest to reservoir. d-e) Injection, depressurize reservoir and open last valve. Close middle valve and then the last valve to complete injection.

Fig. 2-6. The reservoir pressurization serves to force open the valves which have a tendency to stick closed. It also allows the injectors to function against significant back-pressure, which is present when the peristaltic mixer is operating.

2.3.2 Supporting interfaces

A photograph of the overall system is shown in Fig. 2-7. The system currently supports two integrated bioreactor modules, for a total of eight individual bioreactors. The pneumatic actuation and interfacing scheme and the optical sensor interrogation scheme were integral to the PIBA system.

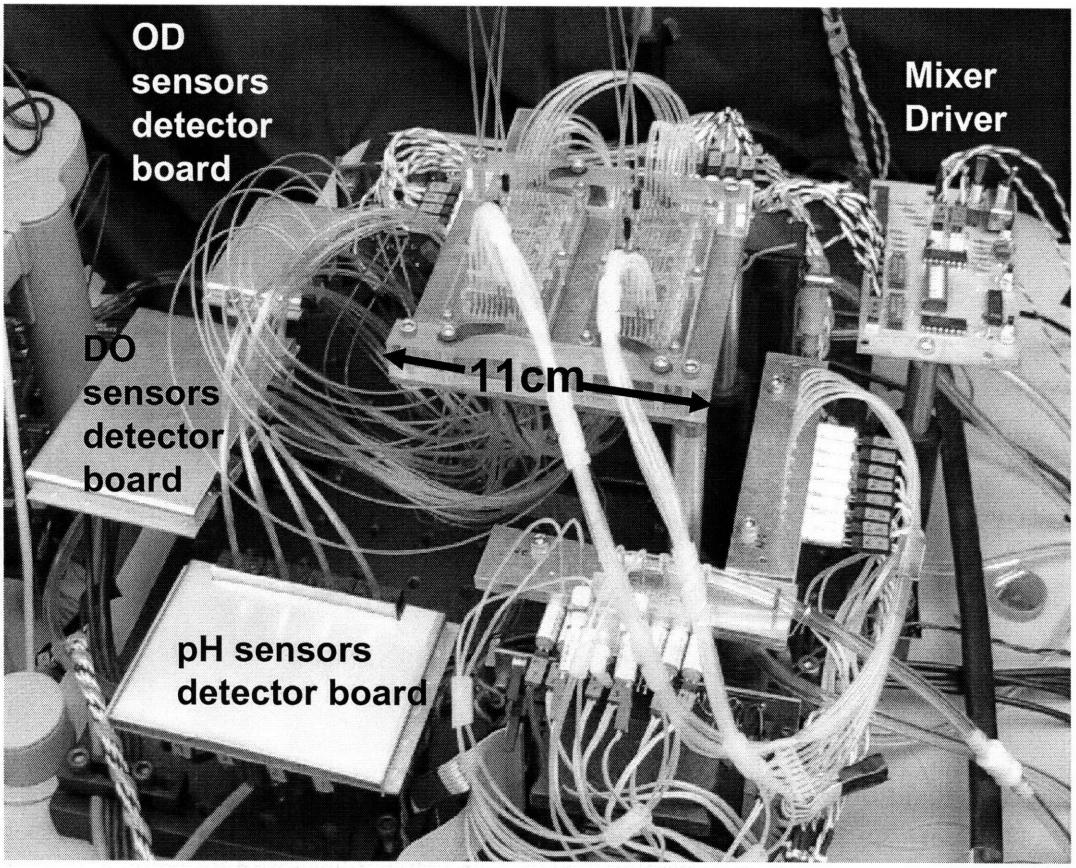

Figure 2-7: Photograph of PIBA system.

Pneumatic actuation

Pneumatic actuation lines are routed to the actuation ports through a manifold integrated into an interface plate as shown in Fig. 2-8. This allows a simple single step alignment and clamping procedure to mount the device, which is much simpler than individually attaching pneumatic actuation lines.

Pneumatic actuators are shared as much as possible because they are the most expensive individual elements in the system. Thus, in each module, the mixing actuators are shared across all reactors as are two of the injector valves. The third valve in each injector is independently controlled in each module, but shared across modules. This is discussed in more detail in Chapter 6.

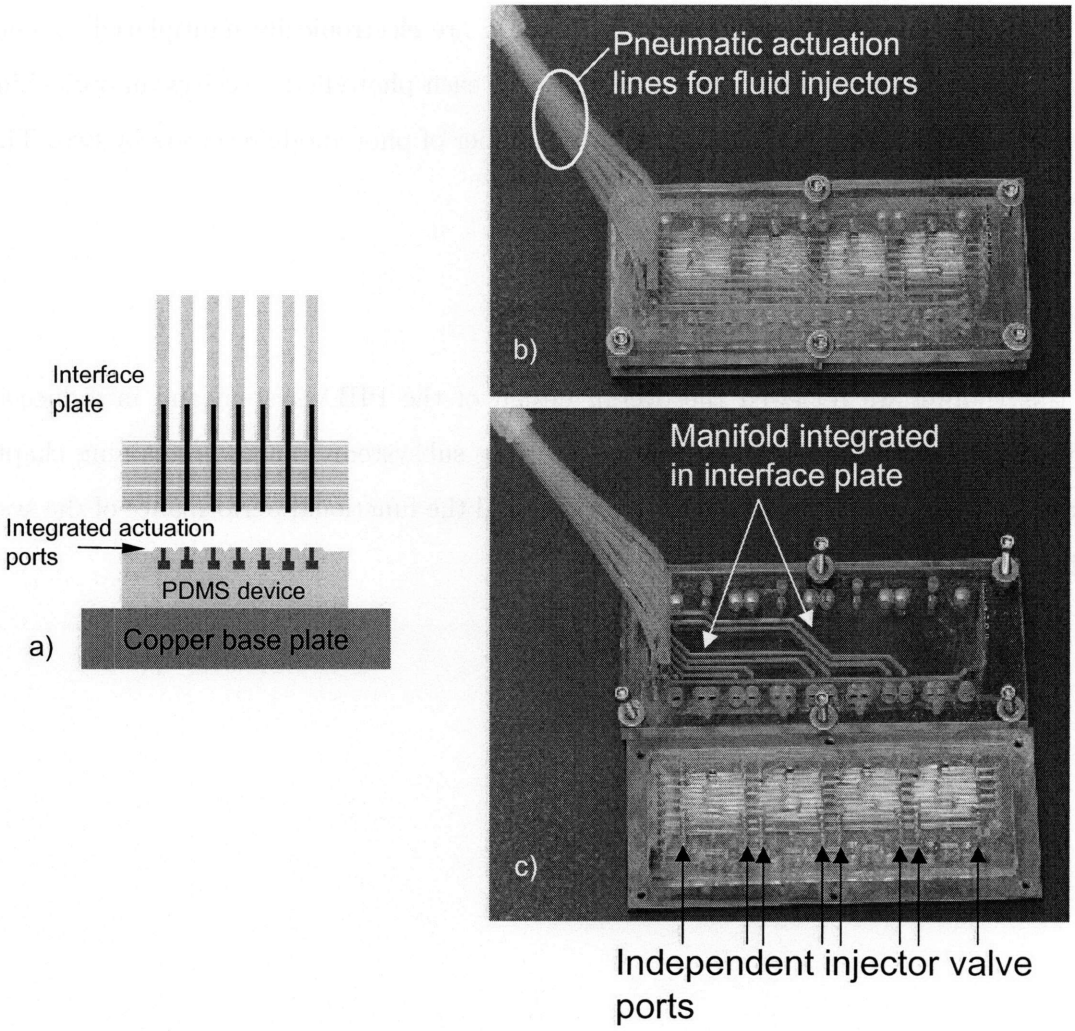

Figure 2-8: a) Schematic drawing of interface plate face sealing to integrated gaskets. b) PIBA device sealed under interface plate. Pneumatic lines are routed to one end for convenience. c) Unmounted interface plate showing the integrated manifold which routs the pressure lines to the independent injector valve ports.

Optical interrogation

Optical sensors are currently independently addressed with fiber bundles, because a suitable integrated waveguide fabrication technology has not yet been developed. Each fiber bundle, contains nine $500\mu m$ collection fibers surrounding a 1mm excitation fiber with integrated colorglass filters to remove long wavelength emission from the LED excitation.

Optical excitation and fluorescence detection are electronically multiplexed to share a single analog to digital converter. and currently, each photodiode receives an optical input from two sensors, thus cutting the required number of photodiode receivers by two. This is discussed in more detail in Chapter 6.

2.4 Summary

In this chapter we reviewed the overall design of the PIBA system and introduced the physical structure of the devices and supporting subsystems. In the remaining chapters, details of the fabrication process are provided and the functional performance of the system will be described and verified.

Chapter 3

Device Fabrication

3.1 Introduction

As outlined in Section 2.1, the design objectives are quite challenging and require implementing high density, complex functions such as mixing, oxygenation, and metered fluid injections in an integrated device. While many fabrication technologies are available to accomplish each of those functions independently, we are interested in developing one which can accomplish all of those functions in an integrated device inexpensively.

A number of candidate processes were evaluated before the design of the polycarbonate mold transfer process to be described in this chapter.

Surface[62] and bulk[63] micromachining processes provide exquisite dimensional control and enough process flexibility to fabricate a wide range of devices from accelerometers, motors, movable mirror arrays, valves, mixing devices, and more. However, due to the relatively large size ($\approx 2 \times 3$cm) of the envisioned devices and the inclination towards disposable devices, such processes were ruled out as being too expensive.

Polymer micromolding technologies[64], in contrast, are much more amenable to mass fabrication, due to their simple single step molding, however they do not offer nearly the process flexibility of micromachining. In these types of micromolding processes, a mold is fabricated using photolithographically defined features, where the final molds can be a

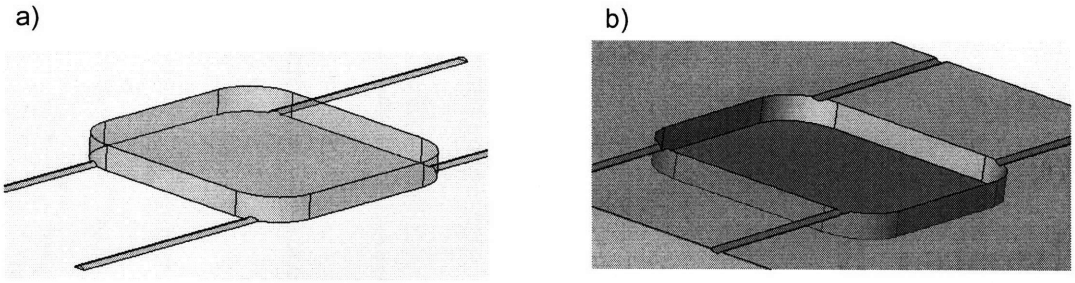

Figure 3-1: a) Multiple depth and profile mold. Well is 500μm deep with square profile and channels are 100μm deep with round profile. b) Corresponding device.

micromachined silicon wafer[65], photoresist patterns on a wafer[61], or electroplated photoresist patterns[66]. From the mold, many negative replicas can be fabricated using either injection molding, hot embossing, or liquid polymer casting. For laboratory prototyping, the latter is most often used because it requires no capital equipment and is quite simple to achieve nanometer scale pattern replication[67]. Unfortunately, the simplicity of these processes also limit their flexibility as devices typically consist of a single material with no moving parts. By taking advantage of elastomeric materials, which can be deformed under pneumatic pressure, numerous authors have circumvented this limitation and fabricated functional, active devices[60],[61] using micromolding technologies.

For mold making, a major disadvantage of photolithographically defined epoxy, or resist is the difficulty in fabricating devices with widely varying surface features, such as those shown in Fig. 3-1. where semicircular channel cross sections are shown along with a chamber that is 3 times deeper than the channels. Rounded channels have been achieved[60] by thermally reflowing photoresist, and multiple level features have been achieved by multilayer lithography[58], however their combination is difficult if both rounded and square features are desired. In addition, photolithographically defined resists can only be made with limited thickness before film stress due thermal mismatch with the substrate causes failure of the mold.

In this chapter, we describe a method that combines conventional computer numeric controlled (CNC) machining and microfabrication techniques that overcomes some of the

shortcomings of the previously described methods, that is particularly well suited to fabricate the devices required for the bioreactor array.

3.2 Polycarbonate mold transfer

For in laboratory prototyping and device fabrication, the polycarbonate mold transfer process described in this section meets all of our requirements. In brief, as outlined in Fig. 3-2 we use conventional CNC machining of polycarbonate master molds using various square and ball endmills to produce features ranging from the growth wells to microchannels for fluid injection. The resulting positive molds are then vapor polished to achieve optical clarity and drastically improve mold release. Numerous negative molds can then be cast out of PDMS from the positive master to allow fabrication of identical devices at the same time. The negative molds are surface treated with a fluorosilane compound to prevent adhesion and finally used to cast the device layers, with embedded optical sensors. Additional polycarbonate molds define external features. Finally, layers are then bonded together using a partial cure bond.

3.2.1 CNC machining

Computer numeric controlled machining of the polycarbonate master molds is performed using an inexpensive table top milling machine. (Sherline with FlashCut CNC). Because this system is an open loop system with stepper motor drive of the three axes, repeatability in positioning is limited by the backlash in the screws. Compensation in software reduces this error to approximately 25-75μm. More expensive commercial production machines and/or services offer better than 5μm precision (Eastern Plastics, Bristol CT).

The dominant source of error that was experimentally determined is the tool runout due to non-concentricity of the tool upon mounting in the headstock. By measuring the width of milled slots, using a microscope and micrometer controlled stage, and comparing the slot width to the end mill diameter, the runout ranged between 25μm and 280μm. This means that instead of the endmill spinning on axis, it moves in a circle with a diameter equal to

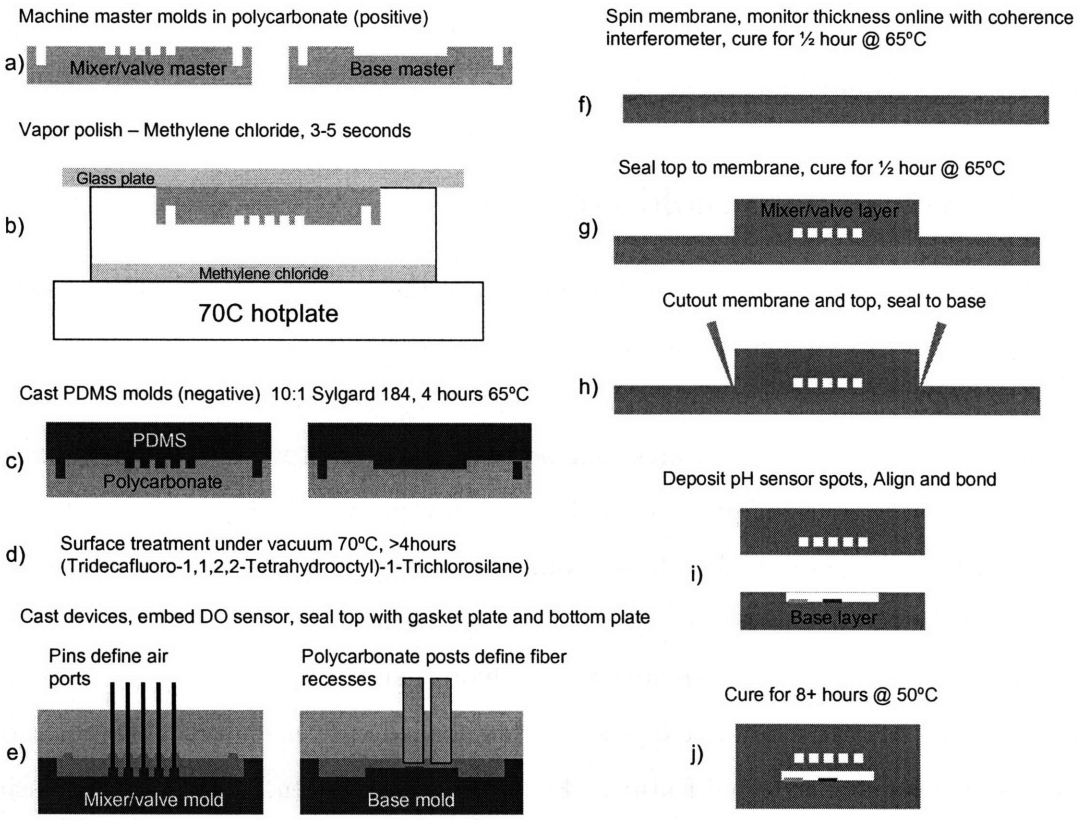

Figure 3-2: Device fabrication steps. a) Machine positive master molds with a computer numeric controlled milling machine. b) Polish molds in methylene chloride vapor to eliminate microscopic tooling marks for optical clarity and easy mold release. c) Cast negative device fabrication molds from PDMS. d) Treat the surface with a fluorosilane compound to prevent adhesion to PDMS. e) Cast the devices using the negative PDMS molds, which define internal device features, and polycarbonate molds, which define external device features. Embed oxygen sensors into base layer and cure for 1 hour at 65°C f) Spin coat a fluorosilane treated silicon wafer with PDMS, monitoring the thickness with a low coherence interferometer. Cure for 30min g) De-mold mixer and valve device layer and bond to partially cured membrane. Cure for 30min h) cut the excess membrane and peel mixer and valve device layer from the silicon wafer. i) De-mold the base layer. Deposit pH sensor in base layer, align with mixer and valve layer and seal. j) Cure for 8 hours at 50°C.

the runout. The amount of runout was strongly dependent on the care taken to mount the tool into the milling machine headstock using collets. Runout measurements using a dial indicator were consistent with the range of observed channel widening.

One other source of error is the thickness non-uniformity in the polycarbonate sheets

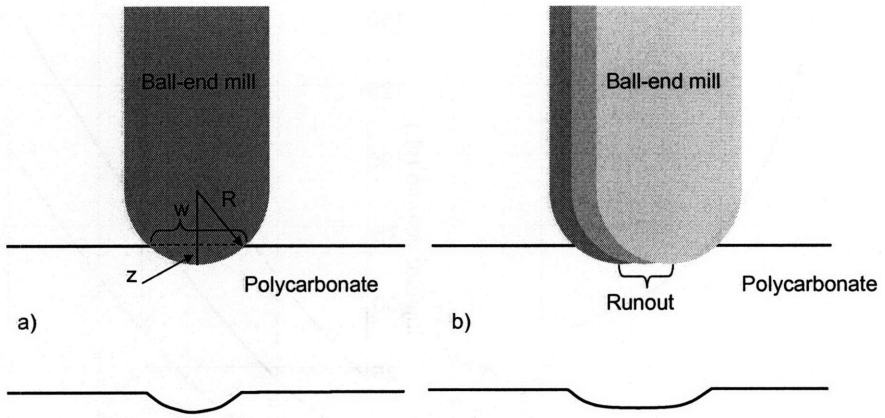

Figure 3-3: a) Schematic of cutting geometry to define rounded channels in the master mold. b) Illustration of impact of end-mill runout on channel width and profile.

used to fabricate the molds. This is in the range of 25-50μm, which leads to depth variaions of the channels and wells of that order and limits the minimum sized channels that can be reliably fabricated to 100-150μm.

These errors, are most critical in defining the fluid injector channel dimensions, as they directly effect the injected volume. The variation in channel width and cross sectional area due to errors in the z-depth can be evaluated as diagramed in Fig. 3-3a. The channel width is given by

$$w = 2\sqrt{R^2 - (R-z)^2} \tag{3.1}$$

and the cross-sectional area, not accounting for runout by

$$A = R^2 \tan^{-1}\left(\frac{\sqrt{z(2R-z)}}{R-z}\right) - (R-z)\sqrt{z(2R-z)} \tag{3.2}$$

The error in the cross-sectional area of the channel due to an error in the z dimension simplifies to

$$\Delta A = 2w\Delta z \tag{3.3}$$

The percentage error in the injected volume and nominal injected volume for channels cut using a 1/32 inch ball end mill, with a z-depth error of 50μm, assuming a 1.6mm long valve

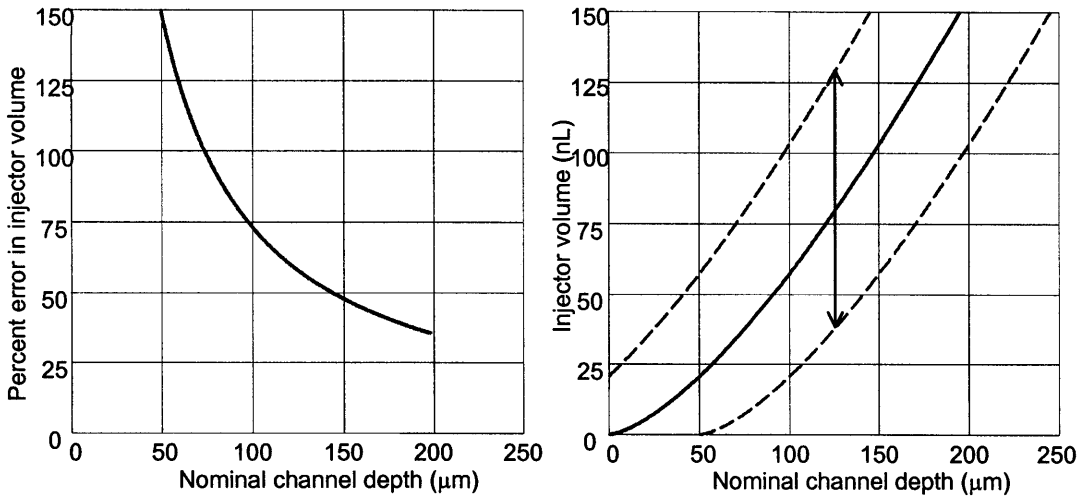

Figure 3-4: Percentage error in injected volume due to a 50μm uncertainty in the channel depth along with the expected injector volumes. The arrow indicates the nominal channel depth for the bioreactor devices.

is shown in Fig. 3-4.

Runout error will add a constant term to the overall volume by enlarging the cross sectional area by the size of the runout and the channel depth as shown in Fig. 3-3b. For a nominally 175μm deep channel with a 100μm runout, and a 1.6mm long valve section, the channel volume will be approximately 100nL.

The surface finish is dependent on machine vibrations, end mill design and feedrate and generally results in a smooth, but frosted surface. Microscopic examination of machined polycarbonate master molds indicate a frostiness consistent with the microscopic imperfection in the machine tools and the imperfect, cutting of the tool as shown in Fig. 3-5.

Measurements of the surface roughness with a Dektak [5] indicate the roughness average is approximately 900nm before vapor polishing as shown in Fig. 3-6 for low polishing vapor concentration.

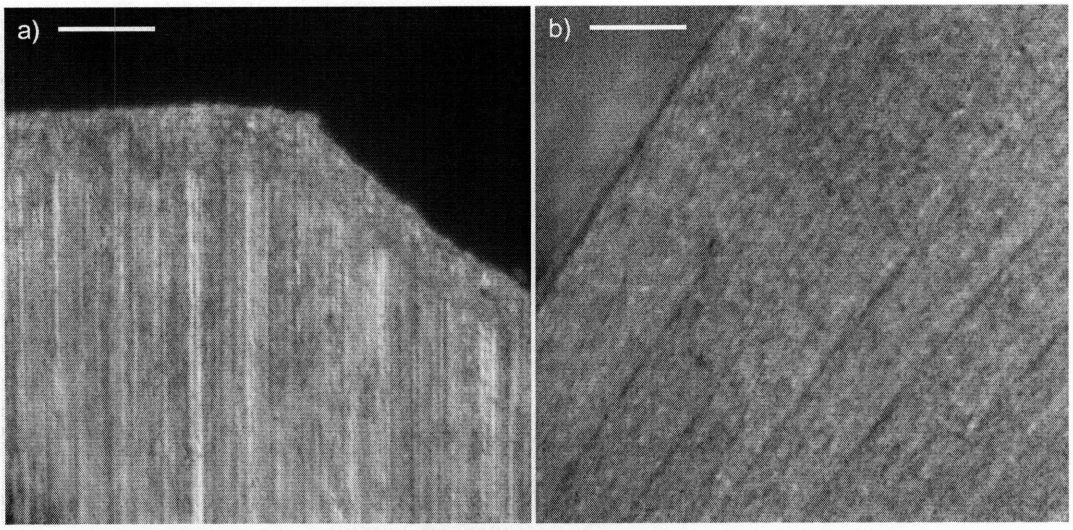

Figure 3-5: a) Photograph of a 1/4 inch end mill cutter and b) corresponding mold surface. Scale bar is 100μm. Vertical lines in the end mill cutter photograph are tool imperfections due to grit size of the grinder used to make the tool. These create a serrated edge on the cutting surface, which is transfered to the mold.

3.2.2 Vapor polishing

The imperfections resulting in a frosted mold surface is both detrimental to addressing the optical sensors and also to mold release due to the large surface area of the micro scratched surface. Vapor polishing smooths these micro scratches by dissolving the materal and allowing surface tension of the liquified surface to smooth the scratches[68],[69].

Polycarbonate is particularly amenable to this process using methylene chloride gas. The quality of the polishing is dependent on processing parameters. Excessive polishing results in condensation of the methylene chloride gas onto the surface, resulting in a spotted surface and loss of resolution. Excessive humidity has can also result in a hazy surface. Repeatable processing can be accomplished by controlling the temperature and partial pressure of the methylene chloride gas, as described in detail in[5], where vapor polishing was shown to reduce the roughness average from 900nm to 100nm as shown in Fig. 3-6[5]. However, for our purposes, simply suspending the mold faces to be polished, approximately 2.5 inches from boiling methylene chloride, as shown in Fig. 3-2, for 3-5 seconds was sufficient.

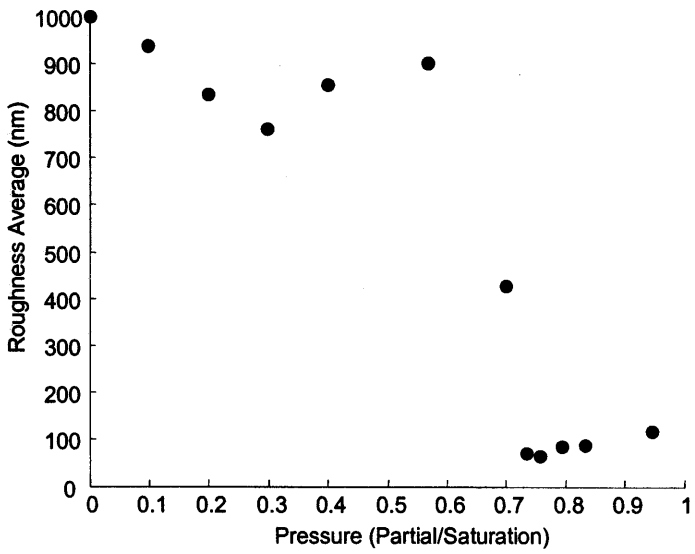

Figure 3-6: Roughness average measurements[5] for polycarbonate roughened with 400 grit sandpaper after 3 minutes of vapor polishing in methylene chloride vapor at 36°C as a function of parital pressure vs. saturation pressure. Above 0.7, the roughness average drops from 900nm to less than 100nm.

Fig. 3-7 shows two negative PDMS molds cast from a master before and after vapor polishing, showing the optical clarity that was achieved in the molds, although circular veritcal scalloping is visible.

While vapor polishing is essential for obtaining a smooth surface finish, it also introduces some distortions into small features. Measurements of channels of similar dimensions to the fluid injector channels revealed that the width

3.2.3 Negative molds

Numerous negative molds can cast from the same master mold, allowing identical device to be fabricated for repeatability. PDMS is also the material of choice for the molds becase it easily demolds from polycarbonate without mold relase agents. In addition, the flexibility of the mold is useful when demolding the devices. However, in order to prevent the PDMS devices from adhering to the mold, the surface must be treated with a fluorosilane compound [58]. This is accomplished by placing the molds in a vacuum chamber (Fig. 3-8),

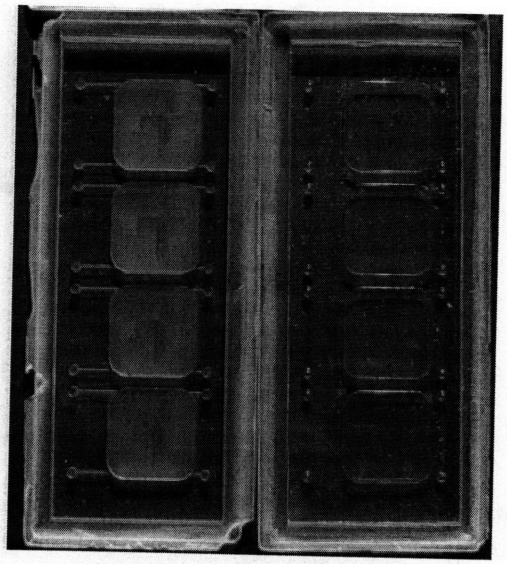

Figure 3-7: PDMS molds cast from a master mold before and after vapor polishing.

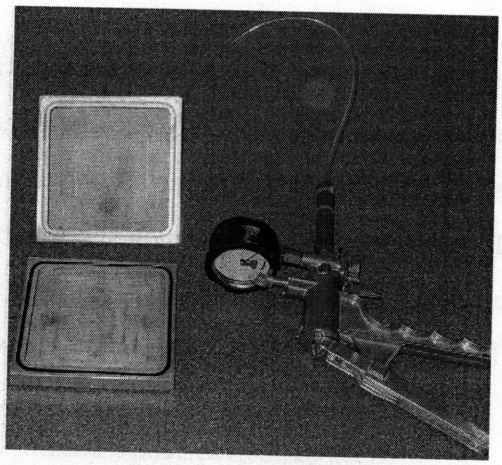

Figure 3-8: Vacuum chamber for surface coaging PDMS molds. A manual vacuum pump achieves 25mmHg vacuum and a hot plate is used to raise the temperature to 70°C.

initially pumped down to 25mmHg vacuum, at 70°C with 5-6 drops of (Tridecafluoro-1,1,2,2-Tetrahydrooctyl)-1-Trichlorosilane (United Chemical Technologies T2492) for 4-12 hours. Surface coating at 70°C increases the vapor pressure of the fluorosilane gas to increase surface coating density.

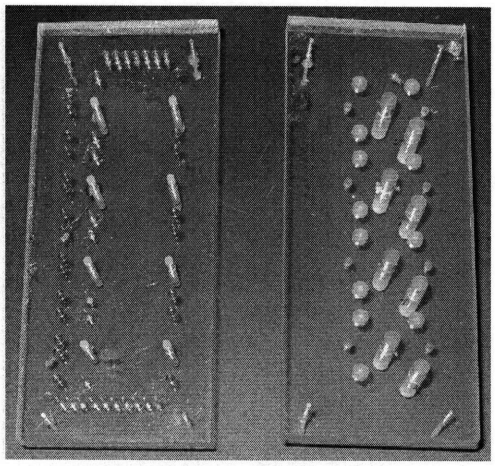

Figure 3-9: Polycarbonate molds to define the external features. Top mold is on the left, which defines the interface gaskets. Bottom mold is on the right, which defines the fiber bundle recesses.

3.2.4 External molds

In addition to the machined microstructured molds, external molds are utilized to produce surface features on the outside of the device. These features include gaskets around all fluid injection and air actuation ports to allow easy face sealing to a manifold, and recesses to accept optical fibers to address the sensors. These molds were fabricated by CNC machining polycarbonate and vapor polishing. Guide pins at the corners align the features with the negative PDMS mold. The external molds for the mixer/valve mold and base mold are shown in Fig. 3-9.

3.2.5 Membrane fabrication

The membranes (40μm - 200μm) were made by spin coating PDMS onto a fluorosilane treated silicon wafer. In contrast to spin coating photoresists, where solvent evaporation plays an important role in film formation and reliable calibrations between spinning speed and resist thickness are commonly used [70], because PDMS does not have a solvent and the viscosity of the polymer remains constant during the entire coating process, the thickness depends on the volume of initial polymer deposited, spinning parameters, and spinning

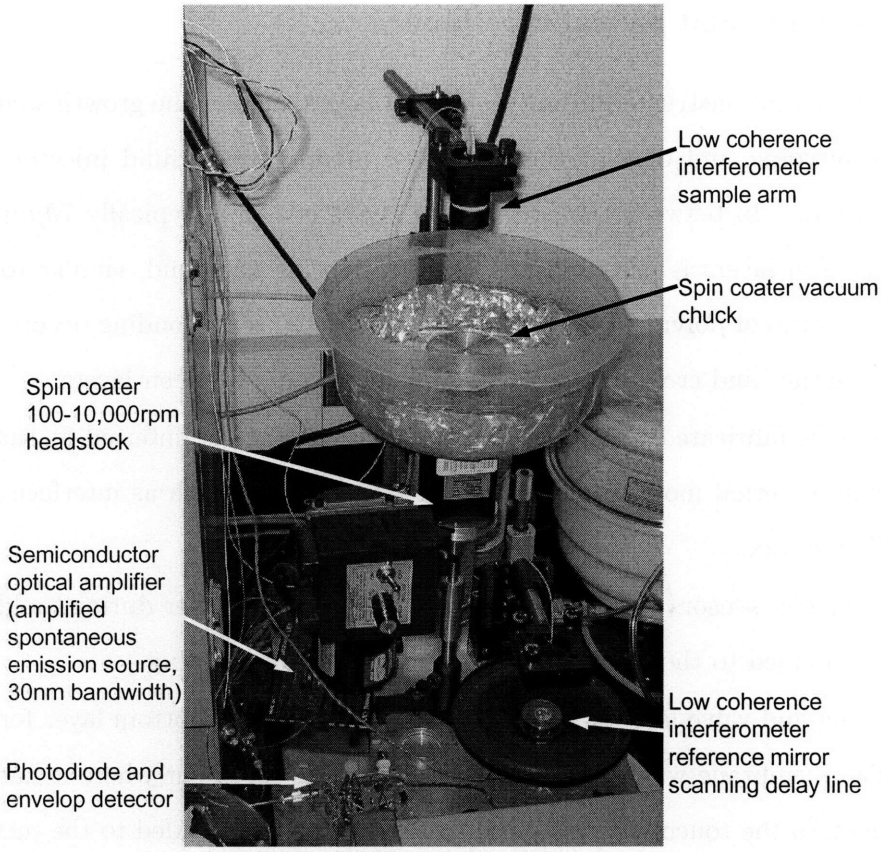

Figure 3-10: Photograph of the polymer spin coater with low coherence interferometer for on-line film thickness monitoring.

time [71]. Therefore, calibration of film thickness open loop is not as reliable and closed loop monitoring of the film thickness during spinning using a low coherence interferometer (LCI) [72] allows fabrication of repeatable membrane thicknesses. A photograph of the spin coater with the LCI is shown in Fig. 3-10. The output of the LCI is an oscilloscope trace where the time dimension corresponds to optical pathlength and the voltage corresponds to the reflectivity. At the dieletric interfaces between PDMS and air and PDMS and silicon, there are peaks in the reflectivity and the separation between these peaks indicates the film thickness. After an initial film thickness calibration, or measurement of the index of refraction of the material, consistent membrane thicknesses were achieved.

3.2.6 Assembly and partial cure bond

The PIBA device is constructed from two molded layers, one for the growth wells, channels, and fluid reservoirs; and one for the peristaltic mixing tubes, fluid injector valves, and pressure reservoir. In between the two molded layers is a thin, typically 70μm membrane. Bonding between layers is accomplished using a partial cure bond, similar to[60], except the same 10:1 ratio of polymer base and curing agent are used. Bonding occurs when layers are sealed together and cross-linking of the polymer occurs between layers.

Each layer is fabricated using one PDMS mold defining the internal features, and one polycarbonate external mold to define the external features, such as interface gaskets and fiber bundle recesses.

Optical oxygen sensors were embedded into the chamber layer during molding and pH sensors were bonded to the inside of the chambers after de-molding.

The mixing and valve layer was cured for one hour and the bottom layer for 50 minutes at 65°C. The membrane was cured for 20-30 minutes to the point where it had just gelled and was tacky to the touch. At this point, the top layer was bonded to the membrane and allowed to cure for an additional 30 minutes. Then, the top layer/membrane were aligned and bonded to the bottom layer and allowed to cure for another 8 hours at 50°C.

The complete device fabrication required approximately 3.5 hours of work for a set of three devices containing four bioreactors each. Further details are given in Appendix A.

3.3 Conclusions and future work

In this chapter, we described a fabrication process useful for integrating fluidic devices requiring cross-sections with various depths and profiles that is suitable for rapid prototyping using equipment that can be purchaced for less than $6000. While the precision in fabrication was not optimal, due to the selection of inexpensive machine tools, improved precision is available through contract manufacturing services.

The fabrication of positive master molds from polycarbonate simplified mold fabrication

by allowing a minimal removal of material. In addition, vapor polishing was introduced as a simple way to remove microscopic roughness, which was the key to enabling mold release from device fabrication molds cast from the master.

While the process proved to be functionally sufficient, there remains a number of interesting areas to explore. With CNC machining, the minimum feature size that can be reliably fabricated is on the order of 50μm-100μm. To achieve a wider range of surface features, the current process could be combined with hot-embossing of photolithographically defined features[73], which would allow this process to be the basis of a smooth macro to micro interface. In addition, improved characterization of the partial cure bond between PDMS layers, including optimization of the curing schedule, and quantifying the bond strength would be of interest.

To look beyond rapid prototyping and consider large scale fabrication of these devices, different fabrication processes would be required, including injection molding of the device layers and a method to bond an oxygen permeable actuation membrane. Along these lines, there remains an entire spectrum of materials to be considered such has hydrophillic thermoplastics, and membranes with high acid/base resistance that could improve the device performance.

Chapter 4

pH control

The ability to control pH is one of the most important capabilities of the stirred tank bioreactor that needs to be duplicated on any bioreactor array system. It is critical to achieving high cell density growth, and for model development because enzyme activity is pH dependent [74]. In this chapter we will review different methods for pH control in miniature bioreactors and then discuss the design and implementation of a pH controller based on microfluidic injectors.

4.1 Background

The pH is a measure of the hydrogen ion, or proton concentration and is defined as $-\log([H^+])$, where $[H^+]$ is the molar concentration of hydrogen, or hydronium, H_3O^+ ions in solution. Therefore, a low pH indicates a high hydrogen ion concentration and a high pH indicates a low hydrogen ion concentration. The hydrogen ion concentration is determined by thermodynamic equilibrium between all species in solution. An example of such an equilibrium reaction is

$$[HA] \underset{K_+}{\overset{K_-}{\rightleftharpoons}} [H^+][A^-] \tag{4.1}$$

where K_- can be interpreted as the probability that an acid, HA will dissociate into its conjugate base, A^- and a proton H^+, and K_+ can be interpreted as the probability that a

collision between a proton and a conjugate base molecule will result in a dissociated acid molecule. The time rate of change of the acid concentration can then be captured by

$$\frac{d[HA]}{dt} = -K_{-}[HA] + K_{+}[H^{+}][A^{-}] \tag{4.2}$$

In steady state, we find the following relationship holds

$$\frac{K_{-}}{K_{+}} = K_A = \frac{[H^{+}][A^{-}]}{[HA]} \tag{4.3}$$

K_A is termed the dissociation constant for the acid. To deal with more conveient numbers, the $pK_A = -\log(K_A)$ is typically used and tabulated. Taking the $-\log$ of Eq. 4.3 and using the definition of pH and pK_A gives us

$$pH = pK_A + \log\left(\frac{[A^{-}]}{[HA]}\right) \tag{4.4}$$

which is called the Hendersson-Hasselbach equation and describes the concept of a buffer. A buffer is a solution which contains approximately equal concentration of an acid, HA and its conjugate base, A^{-}. In this condition, additions of acid or base, lead to much smaller changes in the pH as long as the molar concentration of added acid is less than the concentration of the buffer components. The addition of a strong base ($pK_A >> pH$), B, to a buffer solution will result in a pH given by

$$pH = pK_A + \log\left(\frac{[A^{-}]}{[HA]}\right) + \log\left(\frac{1 + \frac{[B]}{[A^{-}]}}{1 - \frac{[B]}{[HA]}}\right) \tag{4.5}$$

where $[A^{-}]$ and $[HA]$ refer to the initial buffer component concentrations. The change in pH due to a molar addition of acid is given by

$$\Delta pH = \left(\frac{1}{[HA]} + \frac{1}{[A^{-}]}\right)\frac{\Delta[B]}{1 - \left(\frac{[B]_o}{[HA]}\right)^2} \tag{4.6}$$

where $[B]_o$ is cumulative concentration of base added to the solution. We can see that the sensitivity of pH changes to base additions is inversely proprotional to the buffer concentration, and also that when the total amount of added base approaches the concentration of the buffer, the change in pH grows very large.

4.2 pH control alternatives

The standard method for pH control involves the addition of high molarity (3-5M) acid or base into bioreactors using a peristaltic pump in a proportional-integral control loop. For an array of bioreactors, such a method is expensive to implement. Previous workers have utilized an array of 2×2 valves and a syringe pump for common sources of acid and base[32], which allowed intermitent addition of controlled amounts of acid or base. The array of valves essentially allowed multiplexing of the injector into 9 different shake flasks. Other approaches include robotic pipetting of acid and base[3] into an array of 7 bioreactors, which again scales on the principle of sharing the expensive resource (metering fluid) among many bioreactors using a form of mechanical multiplexing.

Thus far, there have been no demonstrations of an array of microfabricated pH controllers. Previous approaches involving pH control or manipulation with microfabricated components include a microfluidic CO_2 gas diffusor[75], electrolytically generated CO_2[1], and electrolytically generated protons or hydroxyl ions [76].

The microfluidic gas diffusor[75] was fabricated using a microfluidics in printed circuit board technology [77] technique. A pH sensor based on measuring the absorbance of a pH indicator dye in solution and CO_2 gas diffusor composed of a microfluidic channel and a silicone membrane was combined to demonstrate pH control of a bicarbonate buffer solution flowing through the diffusor. Such a system would not be amenable for integration into a bioreactor, however due to the requirement for continuous flow through a narrow channel, relatively large size of device, sensitivity of the pH sensing scheme to biomass, and most importantly because carbon dioxide diffusion can only produce carbonic acid, and cannot neutralize organic acids produced in *E. coli* fermentations.

Electrolytically generated carbon dioxide[1] was also recently used to manipulate the pH in an array of microbioreactors. Electrolytic oxidation of formic acid produced carbon dioxide, which diffused through a silicone membrane into the bioreactor. The pH was measured in one bioreactor using an ISFET sensor, which was inconvenient enough to implement that only one reactor was capable of pH measurement. In addtion, as mentioned, this method is unable to compensate organic acids produced in the bioreactor and must be combined with a method to introduce ammonia to achieve pH control in a bioreactor. The toxicity and corrosive nature of ammonia gas makes such an approach difficult.

Carbon-dioxide in equilibrium with water ($K_{eq} = 1.7 \times 10^{-3}$) forms carbonic acid, which has a pK_A of 3.6. Assuming the dissociation of carbonic acid to bicarbonate and proton and the subsequent neutralization of a hydroxyl ion is fast, the response time is limited by the slow reaction rate from CO_2 to carbonic acid of $0.039s^{-1}$ giving a time constant of approximately 25 seconds. This is fast, however, compared to any biological base generation rate. The maximum dosage rate will be approximately 1.3mM of equivalent acid per second, based on the saturation concentration of carbon dioxide (33mM) and the forward reaction rate ($0.039s^{-1}$). This should also be sufficient to neutralize biologically produced bases. The method described in[75] was for a flow through system, presumably to adjust the pH of a fermentation medium in a continuous bioreactor. For a batch reactor [1], the accumulation of bicarbonate ions and the limited solubility of carbon dioxide in water would limit the total amount of base that could be neutralized while maintaining the pH at 7 to 140mM. For ammonia gas, which is abundantly soluble in water, there would be no similar limitation.

The most sophisticated pH control system implemented using microfluidic components was in a miniature bioreactor designed to operate in space[76]. This system was miniature continuous bioreactor with a 3mL working volume. pH control was implemented using electrolytic generation of hydroxyl ions through cathodic electrolysis of water at a titanium electrode. A silver counter electrode in a potassium choloride solution separated by a Nafion membrane, which allowed the transport of potassium ions, completed the circuit. While this method is conceptually attractive and proven effective in a system that flew in space,

implementation of an array of such devices is complicated by the fabrication of the counter electrode and integration of the Nafion cation exchange membrane.

A final pH control method worth mentioning was based on a pH sensitive hydrogel[78], which stabilized the pH of a stream of fluid flowing through the device. The pH sensitive hydrogel was arranged to control the flow of a basic compensating pH stream. Under acidic conditions, the hydrogel would contract and allow more compensating fluid to mix with the input stream, and when the pH was basic, the compensating stream was reduced or turned off. Of course, such a system is strongly dependent on the properties of the hydrogel and sensitive to operating conditions, and not immediately useful for pH control in a microbioreactor array, however the innovative combination of pH sensing and actuation in a material provides an avenue of investigation fundamentally different than previously mentioned approaches.

4.3 Microfluidic fluid injectors

Our strategy for implementing pH control is with acid/base injections because it is relatively simple to implement over gas diffusion or electrolytic methods, and is a proven technique. In addition, it is the same method that is used in stirred tank reactors, and permits duplicating the small scale pH control algorithm in the stirred tank, which is important to allow transfer of results between small and large scale systems[32].

The fluid injector structure was introduced in Sec. 2.3.1. Key requirements for the design included the ability to deliver small, metered amounts of fluid, open loop, without flow sensors. This was important for simplicity to allow a disposable device, ease of operation, and compatibility with the fabrication of the peristaltic oxygenating mixer. The last requirement led to the use of membrane pinch valves and shallow $100\mu m$ deep, rounded channels for valve sealing.

The design evolved from a simple channel with three pinch valves interfaced to an injection port, where the injected fluid could be fed, to a device with an integrated reservoir and pressure chamber. The latter two components were developed in response to the need

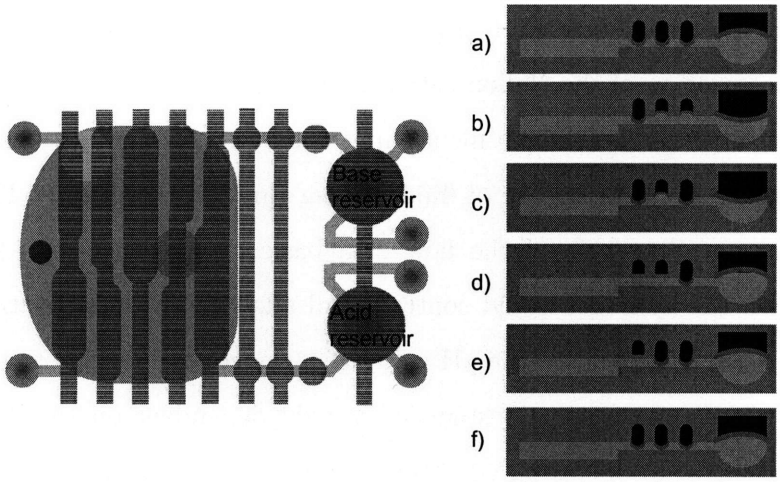

Figure 4-1: Schematic of fluid injector and cross-sectional views showing actuation sequence.

to keep the injected fluid sterile and also to be able to force open closed valves. The shape of the fluid reservoir is hemispherical in order to minimize the dead volume and is an example of the diverse mold profiles required to fabricate the device.

4.3.1 Operation

Fluid injection is accomplished by depressurizing/pressurizing the valves and pressure reservoir in the pattern shown in Fig. 4-1. To reiterate, all but the last valve is opened and the pressure reservoir pressurized. This forces fluid into the channel dead ended by the last closed valve. The pressurization serves to force open the membrane pinch valves, which were found to seal shut if they are not opened for long periods of time. To prevent this from occuring, a valve refresh cycle was executed every three seconds which involved pressurizing the fluid reservoir and opening all except the last valve.

A side effect of the reservoir pressurization was that it also caused the membrane pinch valves to bulge outwards, thereby increasing the amount of fluid that is trapped under the center valve after the first valve is closed (Sec. 4.3.2). This lead to a pressure dependence on the injected volume, which, as will be discussed in Sec. 4.5.2, has implications on the pH control algorithm.

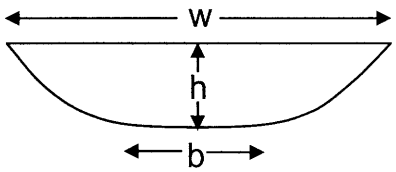

Figure 4-2: Channel cross section and measured dimensions. w=840μm, h = 200μm, b = 280μm. Dimensions were measured using a microscope, x-y-z translation stage, and needle probe as the position reference. b represents the flattened bottom that is due to tool runout.

To avoid the injection of air bubbles, the fluid injectors must be loaded and primed by executing injections until fluid fills the channel and a liquid injection occurs into the empty growth well.

4.3.2 Injected volume

The injected volume is approximately equal to the volume of fluid trapped under the center valve when the first valve is closed. Nominally, this volume should be equal to the volume of the channel underneath the valve plus any bulging in the membrane.

Measurements of the width, height, and approximate shape of the injector channel mold, indicated the channels were rounded trapezoids, as shown in Fig. 4-2, that were 200μm deep, 840μm wide at the top and 280μm wide at the bottom. This was the result of channels nominally 178μm deep, fabricated with a 1/32 inch ball end mill, with a tool runout of 140μm, assuming vapor polishing caused a 5% increase in the measured channel width. The channel volume under a 1.6mm long valve for this geometry would be 175nL.

The membrane bulge due to reservoir pressurization, mentioned in Sec. 4.3.1 can be estimated using approximate expressions for the load-deflection of rectangular membranes. One expression, derived using a variational, energy minimization approach which ignores the strain energy due to bending, is given by Eqn. 4.7[79].

$$P = C_1 \frac{4\sigma t d}{W^2} + C_2 \frac{16Ed}{W^4} \Delta z^3 \tag{4.7}$$

where P is the pressure, E = 750kPa is the Young's modulus, d = 70μm is the membrane

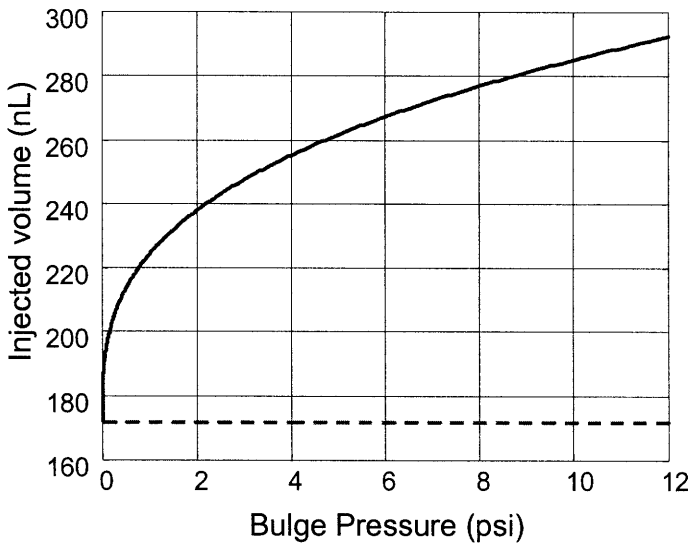

Figure 4-3: Expected injected volume for different hydrostatic pressures. Hydrostatic pressure due to reservoir pressurization causes the valve membrane to bulge, increasing the injected volume. Dashed line indicates injected volume determined by channel dimensions.

thickness, W is the width of the membrane, Δz is the center deflection, and C_2 is a numerical constant dependent on the aspect ratio of the rectangular membrane and the Poisson ratio, which is equal to 0.5 for elastomeric PDMS. The C_1 term accounts for the contribution of residual stress, σ, in the membrane, which we assume to be insignificant. For the 840μm wide and 1.6mm long elastomer membrane $C_2 = 1.29$. From the center deflection given by Eqn. 4.7, the volume of the membrane bulge can be estimated by assuming the trial form of the membrane deflection was

$$w = \frac{\Delta z}{4}\left[1 + \cos\left(\frac{2\pi x}{W}\right)\right]\left[1 + \cos\left(\frac{2\pi y}{L}\right)\right] \tag{4.8}$$

which results in a bulge volume of $LW/4\Delta z$. Results are plotted in Fig. 4-3. For a hydrostatic pressure between 2 and 6 psi, the injected volume is expected to be between 240nL and 268nL.

This is consistent with estimates of the injected volume from titration curve measurements. For a known buffer composition consisting of a weak acid and its corresponding salt

in solution, the pH change with molar concentration of added acid or base is well known and can either be calculated or measured separately using conventional laboratory equipment. The injected volume can be estimated by fitting the change in pH per injection with the slope of the titration curve (Eq. 4.10),

$$\frac{\Delta pH}{\frac{V_{inj}}{V_{well}}M} = \frac{dpH}{dM} \tag{4.9}$$

$$V_{inj} = \frac{(\Delta pH)(V_{well})}{\frac{dpH}{dM}M} \tag{4.10}$$

or more generally, aligning the fluid injector titration curve with one measured conventionally. Fig. 4-4 shows an example of such an alignment where 100mM dibasic phosphate buffer is titrated with 1M hydrochloric and 1M NaOH. The reservoir pressure was 6psi and the valve pressure was 12psi.

For an initial volume of the growth well of $V_{well} = 90\mu\text{L} \pm 10\mu\text{L}$, titration curve slope $dpH/dM = 18.5 \pm 0.5$, concentration of injected acid/base $M = 1 \pm 0.1$, and a measured change in pH due to injections of $\Delta pH = 0.056 \pm 0.005$, yields an injected volume of V_{inj} = 270nL $\pm$ 40nL. The measurement technique is insensitive to absolute pH measurement errors, which are the most likely type of error for the fluorescence based sensors. The most significant source of error is the uncertainty in the initial volume of the well which is limited by the precision of the syringe used to fill the well.

An additional consideration that impacts the stability of the injected volume is the work required to deflect the reservoir membrane as the reservoir empties, and also the work done by a stretched membrane when the reservoir is overfilled. The same variational, energy minimization technique applied to a circular membrane in large deflection[80], results in a similar expression as Eqn. 4.7.

$$P = C_1\frac{\sigma td}{R^2} + C_2\frac{Ed}{R^4}\Delta z^3 \tag{4.11}$$

Where for a membrane with a 0.5 Poisson ratio, $C_2 = 3.524$. Again neglecting the effect of

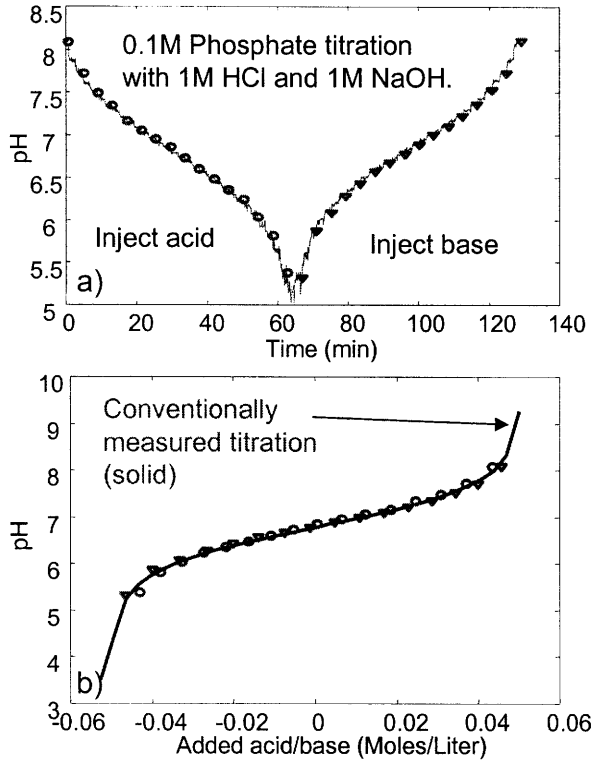

Figure 4-4: a) Titration curve of 0.1M dibasic phosphate measured with integrated fluid injector devices. Injections of acid or base occur every 2 minutes. The sharp steps in the pH confirm rapid mixing. Markers indicate every other injection. b) Alignment with conventionally measured titration curve allows extraction of injected volume of 270nL ± 50nL

residual stress, results are plotted in Fig. 4-5 and explains observed phenomena where the reservoir capacity falls short of what we expect and large initial injections. Because reservoir pressure is spent to deflect the membrane, the hydrostatic pressure available to drive open the injector valves, and cause the injected volume variation due to valve membrane bulge, varies with the volume remaining in the reservoir. For a typical reservoir pressure of 4psi, the hydrostatic pressure will vary from 4psi to 0psi which results in an injected volume variation of approximately 60nL. Also, when the reservoirs are overfilled (1mm-1.5mm bulge), the reservoir membrane contributes 1-3psi to the overall actuation pressure, which can increase the injected volume by up to 20 nL.

Some additional problems with the fluid injectors are the introduction of bubbles through

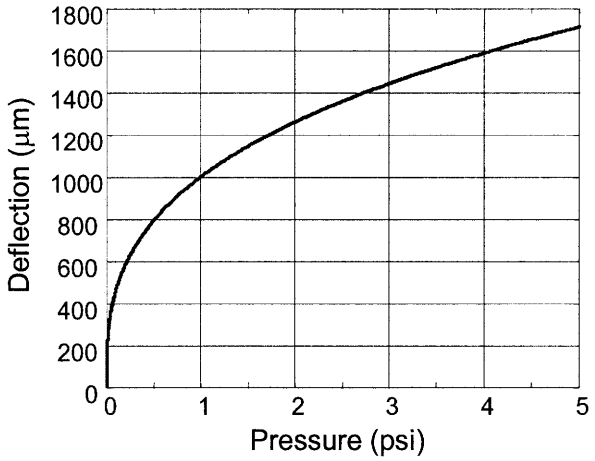

Figure 4-5: Central deflection of reservoir membrane at given pressure differential across the membrane. The curve covers the entire deflection all the way to the bottom of the reservoir.

air diffusion through the valve membranes, which are closed with high pressure, and the valves sticking closed and missing injections. The problem with air bubbles can be reduced by filling the valve cavity with a dilute gel (0.02% carbomer in water) and permanent valve sticking was reduced by limiting the maximum molarity of the base to less than 3M and using a surfactant (1% weight Pluronic F108) in the base solution.

4.4 Mixing

4.4.1 Mixing characterization

Mixing in the peristaltic mixing devices was characterized using a number of methods. The first was a colorimetric measurement where a small amount of blue food coloring was injected into one half or one quadrant of the growth well. During mixing, images of the growth well, syncrhonized with the peristaltic actuation, were taken and used to calculate the color intensity throughout the growth well. The maximum color contrast defined by the maximum minus the minium pixel value of blue was used to characterize the homogeneity of the well. The initial color contrast was normalized to one to correct for variaitons in

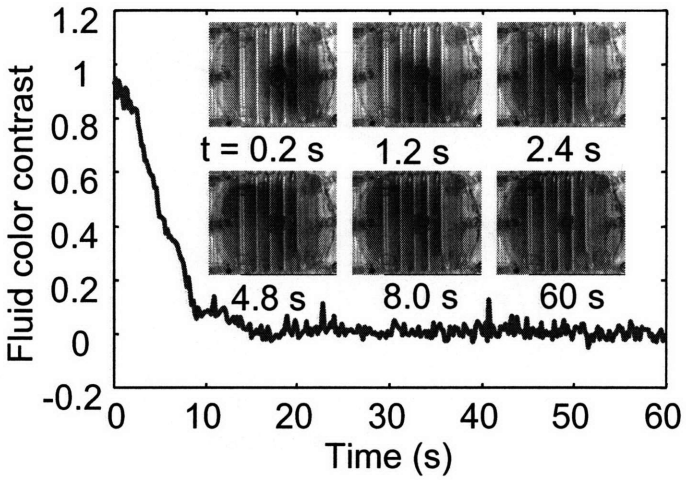

Figure 4-6: Peristaltic mixing in an earlier generation device, without fluid injectors. Fluid color contrast is the normalized maximum difference between pixel intensities, corrected for imaging artifacts. Zero indicates fully mixed.

dye injection and the final color contrast was scaled to zero to correct for non-uniformity in lighting. Fig. 4-6 shows the fluid color contrast and also an image sequence showing the mixing performance of a 500μm deep well with seven straight mixing tubes actuated at 40Hz and 6psi actuation pressure. Mixing occurs in approximately 10-15 seconds, which is typical.

Another method was based on observing the color change in a solution of pH indicator inside of the growth well. The well is filled with a 0.3mM solution of bromothymol blue and acid/base injections using the fluid injectors induce a color change in the indicator. Fig. 4-7 shows two image sequences, one after an acid injection and one after a base injection which shows mixing again in 10-15 seconds. Actuation conditions were 25Hz and 3psi. Also of note is an indication of the flow pattern inside the growth well which is much more intricate than the case with the straight tubes.

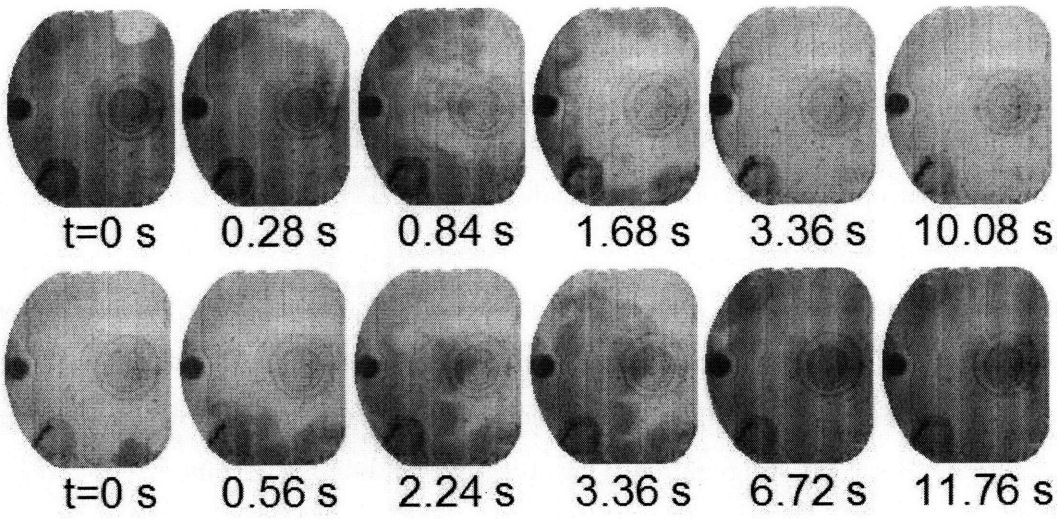

Figure 4-7: Image sequence after an acid injection (top) and a base injection (bottom). The growth well contained 85mL of 0.3mM bromothymol blue pH indicator. Actuation pressure was 3psi with a 25Hz update rate. Peristalsis was to the left.

4.5 pH control implementation

4.5.1 Modeling

A model for the pH inside the microbioreactor is given below.

$$\frac{dX}{dt} = \mu X \tag{4.12}$$

$$\frac{dpH}{dt} = -\alpha r X + b \tag{4.13}$$

$$\frac{db}{dt} = \frac{-b}{\tau_m} + \frac{B^{inj}}{\tau_m} \tag{4.14}$$

$$\frac{dS}{dt} = \frac{-S}{\tau_s} + \frac{pH}{\tau_s} \tag{4.15}$$

where X is the cell density (g-dcw/L), pH is the pH of the culture medium, b is the time rate of change in the pH due to to added base, which captures the mixing in the growth well, and S is the pH as measured by the sensor. r is the specific acetate secretion rate (moles/g-dcw-L), $\alpha = dpH/dM$ is the change in pH due to a molar change in the acid, B^{inj}

represents the pH change equivalent of a base injection, τ_m is the time constant for mixing in the growth well, and τ_s is the response time of the pH sensor.

Due to the nature of the fluid injectors, the pH will be controlled intermitently by injections of discrete volumes of base or acid, therefore B^{inj} will be a sequence of impulses with magnitude $N_{inj}M_{acid/base}\alpha(V_{inj}/V_{well})$. Where $M_{acid/base}$ is the molarity of the acid or base solution. Negative valued impulses will model acid injections. We will measure the pH sensor output, S, intermitently, approximately every 60 seconds. The time will fluctuate because the time between samples will depend on how many injection cycles, each taking approximately 1 second, are required. Our objective will be to determine N^{inj} at each time step in order to maintain the pH as close to the setpoint as possible, while also minimizing the chance of extreme pH errors, which can be detrimental to the cell culture, and take a long time to be corrected if we do not implement an acid injector for the sake of increased base capacity.

Because the biological dynamics of pH changes are quite slow, where the maximum observed change in pH with time was approximately 1.5 pH units per hour, and because of the coarse nature of the fluid injectors, we will forego classical control systems analysis in favor of a direct solution of the model equations and a heuristic approach.

Non-ideal characteristics of the injectors need to be accounted for to successfully execute the pH controller. The first is the injected volume is not precisesly known, and in general, the buffer capacity is not known precisely, so the change in pH due to an injection, B^{inj} is not precisely known. Thus, part of the pH controller will be to estimate the future change in pH due to an injection. In addition, as mentioned previously, the PDMS membrane pinch valve has a tendency to stick to the PDMS channel and therefore, on occasion an injector cycle will not result in an injection and it was necessary to detect such an occurance and ignore it for the purposes of estimating the pH change per injection.

In addition, we do not have precise values for the mixing time, $\tau_m \approx$ 10sec; sensor response time, $\tau_s \approx$ 30sec; growth rate, $\mu \approx 0.5\text{hr}^{-1}$; acid production rate, $r \approx 0.01$; or slope of the titration curve $\alpha \approx 14$ (defined medium) or $\alpha \approx 60$ (modified Luria-Bertani); and

therefore we chose the experimental conditions to minimize the effects of these uncertainties. The impact of these uncertainties can be judged by the exact solution for the pH and the pH sensor at time t after the previous injection.

The pH is given by

$$pH(t) = pH_{n-1} + \frac{\alpha r X_{n-1}}{\mu}(1 - e^{\mu t}) + B^{inj}_{cum}(1 - e^{-t/\tau_m}) \tag{4.16}$$

where $B^{inj}_{cum} = \sum_{k=0}^{n-1} B^{inj}_{k} e^{-(n-k-1)\Delta t/\tau_m}$ is the weighted sum of the cumulative injections and pH_{n-1} is the previously sampled pH. The zero of time corresponds to the time of the previous injection. In this model, the decrease in the pH is proportional to the growth rate, assuming acetate is produced by the cells at a constant rate. The response of the pH to a base injection is a rising exponential, which captures the time required to mix the injected base into the growth well.

For the sensor output, the time response is

$$\begin{aligned} S_t &= pH_{n-1}(1 - e^{-t/\tau_s}) + \frac{\alpha r X_{n-1}}{\mu}(1 - \frac{1}{(1+\mu\tau_s)}e^{\mu t}) + B^{inj}_{cum}(1 - \frac{\tau_m}{\tau_m - \tau_s}e^{-t/\tau_m}) + \dots \\ &\dots + (S_{n-1} - \frac{\alpha r X_{n-1}\tau_s}{(1+\mu\tau_s)} + \frac{B^{inj}_{cum}\tau_s}{\tau_m - \tau_s})e^{-t/\tau_s} \end{aligned} \tag{4.17}$$

where S_{n-1} is the previously sampled sensor output. As expected, in the limit as $\tau_s \to 0$, $S_n \to pH_n$.

Because we sample the pH at intervals, Δt, precise knowledge of the model parameters is not required as long as

$$\begin{aligned} 5 &\leq \tfrac{\Delta t}{\tau_m} \leq \frac{1}{\mu} \\ 5 &\leq \tfrac{\Delta t}{\tau_s} \leq \frac{1}{\mu} \end{aligned} \tag{4.18}$$

In this case, the exponential terms in Eqns. 4.16 and 4.17 can be ignored with less than 1% error and the equations simplify to

$$S_n = pH_n = pH_{n-1} + \alpha r X_{n-1} \Delta t + B_{n-1}^{inj} \quad (4.19)$$

$$pH_{n-1} + \alpha r X_{n-1} \Delta t + N_{n-1}^{inj} M_{acid/base} \alpha (V_{inj}/V_{well}) \quad (4.20)$$

where we have also used the fact that $B_{cum}^{inj} = B_{n-1}^{inj}$ for $\Delta t >> \tau_m$. This highlights the importance of achieving rapid mixing within the bioreactor. The 10-15 second mixing time indicates that sampling times between 50 and 75 seconds will satisfy the requirement. In fact the time constraint imposed by the sensor response of 15-30 seconds imposes a more strict limit of 75 to 150 second sampling intervals, which is still relatively fast compared to the biological time constants. With a maximum acid production rate causing a pH change of approximately 1.5units/hour in a typical medium, a 150 second sampling time will result in a maximum error of only 0.06 pH units.

4.5.2 pH control algorithms

Even with fast mixing and a fast pH sensor, Eqn. 4.20 still contains parameters that are not precisely known. α, the change in pH due to a molar change in acid or base, can be measured ahead of time through a titration curve of a sample of the medium with an approximate 10% error; V_{well} is controlled during innoculation and is known within 15%; V_{inj} was measured as described in Sec. 4.3.2 and known to be within a range of 50 to 300nL; the acetate production rate, r was estimated from previous fermentation data to be on the order of 0.01 (mols/g-dcw/hr), but with very little certainty; the cell density, X_{n-1} can be inferred from optical density measurements, however due to the need for an endpoint calibration, as discussed in Sec. 6.2.3, measurements are in error by up to a factor of two.

Therefore, we are unable to simply calculate the number of injections required from Eqn. 4.20

$$N_{inj} = (pH_{target} - S_{n-1} - \alpha r X_{n-1} \Delta t) \frac{V_{well}}{V_{inj} \alpha M_{acid/base}} \quad (4.21)$$

A simple solution is to estimate the unknown terms, $\alpha r X_{n-1}$, which is the time rate

of change of the pH with respect to time, dpH/dt, due to the metabolic processes of the cells, and $\frac{\alpha M_{acid/base} V_{inj}}{V_{well}}$, which is the change in pH due to a single injection, ΔpH. These parameters can be estimated quite simply if the sampling time constraints of Eqn. 4.19 hold. For the time derivative of the pH, we calculate

$$\frac{dpH}{dt} \approx \frac{S_n - S_{n-1}}{\Delta t} = \alpha r X_{n-1} \tag{4.22}$$

when there is no base injection, and for the change in pH due to an injection, we calculate

$$\Delta pH \approx \frac{1}{N_{inj}}(S_n - S_{n-1} - \frac{dpH}{dt}\Delta t) = \alpha M_{acid/base}\frac{V_{inj}}{V_{well}} \tag{4.23}$$

for samples before and after a base injection has occured. With the estimates of these two parameters, Eqn. 4.21 is in terms of known parameters

$$N_{inj} = \lfloor (pH_{target} - S_{n-1} - \frac{dpH}{dt}\Delta t)\frac{1}{\Delta pH} \rfloor \tag{4.24}$$

Where $\lfloor \cdot \rfloor$ indicates rounding towards zero. To encode acid or base injections, $N_{inj} > 0$ indicates a base injection is required and $N_{inj} < 0$ indicates an acid injection is required.

An intermittent pH control algorithm based on Eqn. 4.24 is illustrated in Fig. 4-8. pH measurements are taken every 30-120 seconds and injections are permitted before every other measurement to guarantee time slots to estimate dpH/dt. Estimates of the natural change in pH and the change in pH due to each injection are low pass filtered to reduce noise and any change in pH due to an injection below a given threshold are assumed to be due to a missed injector. The pH is controlled by predicting the pH at the next injection window, assuming the pH trajectory is linear. If the pH will cross either a low, or high preset threshold around the setpoint, base or acid is injected to bring the pH within the opposing threshold.

Because one of our objectives is to avoid extreme deviations from the pH setpoint, there is a maximum number of injections permitted at each interval. This maximum number of

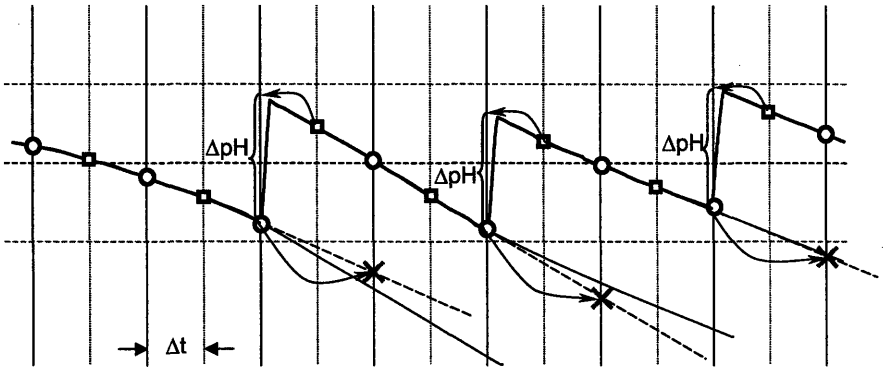

Figure 4-8: pH control algorithm: The pH is sampled at approximately Δt time intervals. The time required to make injections causes a small variation in sampling intervals. Injections are permitted every other sampling interval to allow estimation of the natural change in pH due to metabolic processes of the cells. This estimate of dpH/dt is used to predict the pH at the next injection window to decide if base injections are necessary. It is also used to improve the estimate of the change in pH due to each injection by removing the effect of the natural change in pH.

injections is reduced for the following conditions:

1. When the pH error is small. Assuming the pH does not change very much over the measurement time interval, this minimizes problems due to rare glitches in the pH measurement electronics. For example, a glitch where a pH of 4 was indicated which could cause a large number of erroneous injections to restore the pH to 7.

2. When the pH is at the extreme range of the pH sensors. When the pH is greater than 7.5 or less than 5.5, the uncertainty in the pH is very large because it is out of the linear range of the pH sensors. Reducing the maximum number of injections minimizes the chance of extreme errors.

3. If a titration curve of the growth medium can be measured or calculated, the maximum number of injections is scaled inversely to the slope of the titration curve. Thus, when the change in pH due to an injection is high, the maximum number of injections is reduced.

The last two conditions are relevant when the pH controller is first activated and guarantees

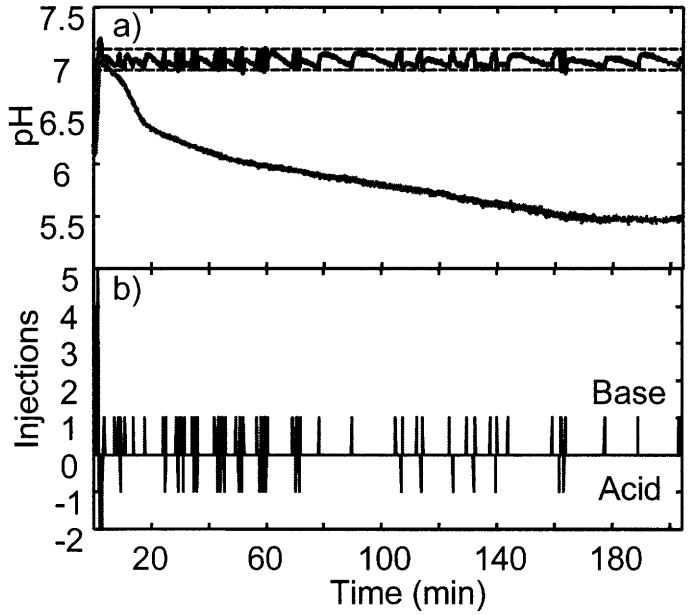

Figure 4-9: a) pH with and without control during a 100mM sulfite oxidation in 24mM phosphate. For both cases, pH was brought initially to pH 7.0. Afterwards, the controller maintains the pH at 7.0 ± 0.1 b) Injections by the controller. Positive for base and negative for acid.

a slower approach to the setpoint with minimal overshoot. This effective damping of the pH controller is especially important when the acid reservoir is eliminated in favor of an additional base reservoir. In this case, pH overshoots cannot be corrected and depend on the microbially generated acids to bring down the pH.

Fig. 4-9 shows an example of pH control of a sulfite oxidation. A 100mM sodium sulfite solution with 24mM of sodium phosphate, initially adjusted to a pH of 6 was loaded into a bioreactor device. 1M HCl and 1M NaOH are used as the acid and base control solutions. The pH setpoint was 7.0 and high/low thresholds are set 0.1 pH units away. As sulfite ions are oxidized into sulfate ions, the buffer capacity of the solution is reduced and the pH decreases. In this example, both acid and base injections are used during the control because occasional overshoots in the pH require acid injections to correct.

Fig. 4-10 shows an example of pH control of an *E. coli* bioreaction in an enriched Luria-Bertani medium with phosphate buffer and glucose. Initially, two injections are requred

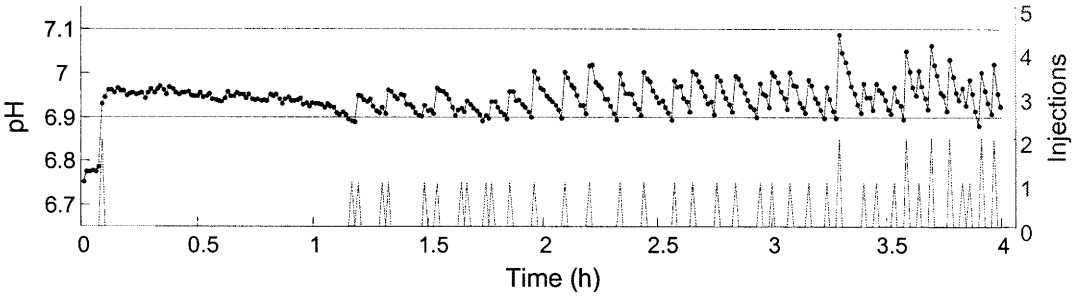

Figure 4-10: pH control example of an E. coli bioreaction on modified LB medium. Initially, two injections bring the pH within the dead band of the controller. Note initial injections are inconsistent due to bubbles in the base reservoir or valve sticking. Because the acid reservoir is not used, to prevent over injection of base, the maximum allowable injections is reduced proportional to the pH error, which is why there is a bias towards the lower pH threshold.

to bring the pH witin the deadband of the controller. Close inspection of the controller injections between 1 and 1.7 hours shows evidence of valve sticking when the first injection yields no change in pH or some injections which do not change the pH very much. The latter was traced to small bubbles invading the injector reservoir that were eventually flushed out. Regardless of these non-idealities of the fluid injectors, the pH was maintained near the setpoint and above the lower threshold while base remained in the injector reservoir.

This implementation of pH control in a microbioreactor array was the key enabling technology to realize growth to high cell densities in a microbioreactor array as will be discussed in Chapter 7.

Optimal pH control algorithm

The previously described and implemented algorithm used preset thresholds, which set the average error of the pH controller. Such fixed dead band operation of pH controllers is typical in bioreactors, and controllers with acid and base actuators to prevent pH oscillations. In fact, the acid and base injections observed during the sulfite oxidation experiment in Fig. 4-9, where only base injections should have been necessary was indicative of this issue, which arose because the thresholds were set very close to the resolution of the injectors.

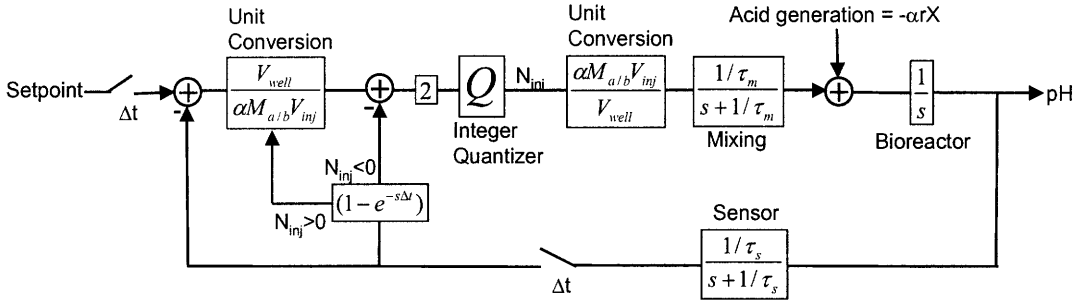

Figure 4-11: Block diagram of pH control model. T is the sampling interval and model parameters are as given in Sec. 4.5.1. The integer quantizer models the discrete injections. The factor of two before the quantizer causes the low pH threshold to be one half the injector resolution. The differencing block $(1 - e^{-sT})$ provides an estimate of the change in pH due to an injection when an injection was administered in the previous time slot, and estimate of the acid production otherwise.

For cases where only compensations of acid are necessary, as is common in *E. coli* fermentation, setting a wide deadband to avoid oscillations is unnecessary and tighter control over the pH is possible. In this case, the error of the pH controller is fundamentally limited by the discrete nature and fixed resolution, set by the minimum injected volume, of the injectors. The best possible pH error will be one half the pH resolution, or

$$pH_{error} = \frac{\alpha M_{acid/base}}{2} \frac{V_{inj}}{V_{well}} \tag{4.25}$$

This accuracy can be achieved by adaptively setting the pH threshold to be equal the minimum error. For typical values of $M_{base} = 2.5$M, $\alpha = 20$, $V_{inj} = 250$nL, and $V_{well} = 100\mu$L, the minimum pH error is 0.06, which is within the ± 0.1 expected for bioreactor pH controllers. A block diagram illustrating this type of controller is shown in Fig. 4-11.

4.5.3 Error analysis

The pH control algorithm described in Sec. 4.5.2 is quite robust, even for the non-ideal case where Eqns. 4.19 are not satisfied. In this situation, the pH will not have fully responded to the base injection, and also the sensor response will not track the pH exactly. The primary

consequence of these non-idealities will be underestimation of the change in pH due to each injecton through Eqn. 4.23, and also erroneous estimates of the time rate of change in the pH through Eqn. 4.22. Fig. 4-12a plots Eqn. 4.16 and Eqn. 4.17 for $\tau_m = 10$s and $\tau_s = 20$s, which are typical for PIBA devices. Samples of the sensor response for different Δt along with linear extrapolations back to the time of injection indicate the error in estimating ΔpH, which is shown vs. sampling time in Fig. 4-12b. The key limitation is the sampling time must be longer than the full rise time of the sensor, otherwise large underestimates of ΔpH will occur. Beyond the peak, the estimate is insensitive to the sampling time, but the error, which is dominated by the phase lag introduced by the sensor, can be calculated from the long time difference between Eqn. 4.17 and Eqn. 4.16 response time.

$$E_{\Delta pH} = \frac{\alpha r X_{n-1} \tau_s}{1 + \mu \tau_s} \tag{4.26}$$

This problem can be overcome by simply waiting for the peak in the response before computing estimates for the change in pH, however this is not always possible if the acid production rate is high, for example, near the end of a fermentation. Fortunately, the consequences of these errors are low, because the algorithm reduces the maximum number of injections when the pH error is small. An illustration of the insensitivity to these types of errors, and in fact, the minimal performance improvements available by using the optimal algorithm is shown in Fig. 4-13 where the results are compared with the simplest possible algorithm, where a single injection is administered whenever the pH is below a fixed threshold, in this case 6.9.

While the overall performance of the optimal algorithm is better in terms of the zero average error and tighter overall bounds given by $\Delta pH/2$, it comes at the cost of a more complicated algorithm. The simple algorithm maintains the pH within the desired range, except near the end of the fermentation when the acid production rate is high. Even in that case, the excess error is minimal. Disadvantages of the simple approach are the average error of [(low threshold) $- \Delta pH/2$], and the slow approach to the pH set point, if the initial

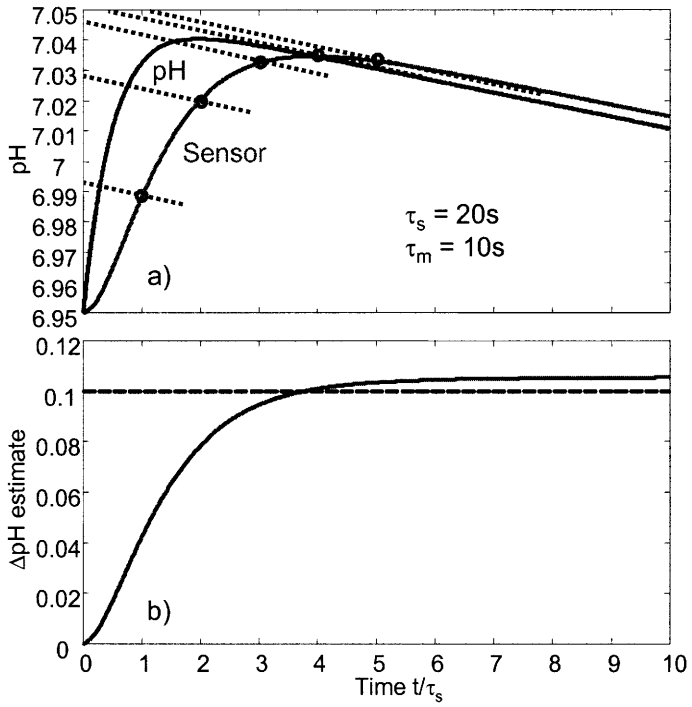

Figure 4-12: pH and sensor response due to a base injection for sensor time constant, τ_s = 20s, and a mixing time, τ_m = 10s. Markers indicate possible sampling times and the dashed lines lead to the estimated change in pH due to an injection, based on extrapolating to the time of injection assuming a linear decrease in pH with time. Precision is best after the sensor response peaks and there is a small error due to the phase lag introduced by the sensor response time.

pH were far below the set point.

The performance of the simple algorithm also indicates the robustness of the optimal algorithm to gross under estimates of dpH/dt and ΔpH. As long as the maximum number of injections when the pH error is small is set equal to 1. In this case, the optimal algorithm behaves as the simple algorithm with the low threshold set to the pH setpoint.

4.5.4 pH controller capacity

A final issue to address is the capacity of the pH controller, or the maximum amount of acid that can be neutralized. As will be discussed in Sec. 7.3.1, this was a limiting factor in the performance of the pH controllers.

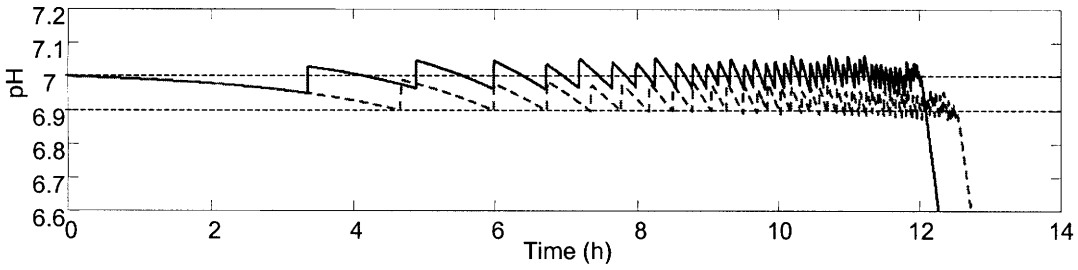

Figure 4-13: Comparison between two pH control algorithms. The solid line is the optimal algorithm described in the text. The dashed line is a simple algorithm where one injection is administered if the pH crosses the low threshold. Model parameters correspond to an *E. coli* fermentation on defined medium. The emptying of the base reservoirs was incorporated. While the performance of the optimal algorithm is slightly better as far as zero average error, the simple algorithm performs admirably, but with steady state error given by (low threshold)-$\Delta pH/2$.

The capacity of the pH controller is determined by the volume of base in the fluid reservoir and its molarity since this product gives the total moles of base available to neutralize biologically produced acids. Assuming that we want the maximum possible controller capacity, the molarity of the base is determined primarily by the desired pH resolution, which is in turn affected by the by a number of factors including the buffer capacity of the growth medium, the fluid injection volume, and total volume. The buffer capcity determines the change in pH per molar injection of base, which is equal to the product of the molarity of the base solution and the ratio of the fluid injector volume to the total volume. Thus, the maximum molarity of the base controller solution is given by:

$$M_{max} = \Delta pH \frac{dM}{dpH} \frac{V_{init}}{V_{inj}} \tag{4.27}$$

where ΔpH is the sum of the high and low thresholds, or total dead band, dM/dpH is the reciprocal slope of the titration curve of the medium at the pH setpoint, V_{init} is the initial volume of the growth well, and V_{inj} is the fluid injector volume. For a ΔpH of 0.2, $dM/dpH = 0.02$, and $V_{init}/V_{inj} = 330 - 1000$ we obtain a maximum molarity range between 3.8M and 1.3M. Beyond these performance constraints, as mentioned in Sec. 4.3.2,

the molarity is also limited by the base resistance of the PDMS to less than 3M to reduce the tendency for the membrane pinch valves to seal shut. Finally, in order to avoid the introduction of an excessive volume of fluid, which dilutes the cell culture, we would like to use the highest molarity base solution possible, with the highest resolution fluid injectors possible, pushing the design of the fluid injectors to base resistant materials with smaller feature sizes.

4.6 Conclusions and future work

In this chapter, we described the design and demonstration of pH control in the PIBA. pH control within 0.1 pH units was achived using microfluidic injectors integrated with a peristaltic mixer.

In operating the pH controller over many bioreactions, a number of deficiencies became apparent that could be improved in future iterations. One is an improvement in the resolution and capacity of the pH controller, and elimination of the valve sticking problems.

Near term, the capacity of the pH controller could be improved by enlarging the fluid reservoirs at the cost of larger device area and also dilution of the growth medium with injected base. A better approach would be to increase the molarity of the base while reducing the volume of each injection.

Improved pH resolution can be accomplished by fabricating smaller injector channels. This was limited by device yield issues, as smaller channels were found to be sealed closed in a number of cases. This was hypothesized to be due to overcompression of the device layers during bonding, which was indirectly related to end-mill runout that produced wider aspect ratio channels than expected.

Valve sticking was presumed to be due to the concentrated acid/base reacting with the PDMS [81],[82] and allowing the surfaces to bond through interdiffusion of polymer chains [83] with dimethyl-vinyl ends and dimethyl-hydrogen ends, which are then cross linked by the platinum catalyst remaining in the elastomer[84]. However the specific nature of this interaction should be the subject of further research.

Both of these issues could potentially be resolved by fabricating the devices from materials with higher acid/base resistance, and improved dimensional stability, such as cyclic-olefin-copolymer thermoplastics for the channels and perfluoropolyethers [85] for the membrane. Such a change in materials could also be more favorable to scaling the device fabrication for mass production.

Chapter 5

Oxygenation

Providing a high oxygen transfer rate is paramount for any high cell density culture system to ensure that the bacteria do not grow under oxygen limited conditions. Ideally, it should be possible to maintain the dissolved oxygen concentration above a set threshold. In this chapter we will discuss the oxygenation performance of the peristaltic oxygenating mixer and a method for dissolved oxygen control.

5.1 Oxygen transfer measurement

In Sec. 2.2.2 we discussed an analytical method to calculate the steady state oxygen transfer coefficient $k_L a_{ss}$, which characterizes the maximum oxygen uptake rate (OUR) that can be supported in a bioreactor. Because it is difficult to generate a range of known oxygen uptake rates in a liquid, direct measurement of this parameter is not possible. In conventional stirred or shaken bioreactors, measurements of the $k_L a$ using dynamic methods[26], which we will call $k_L a_{dg}$, are equivalent to the steady state $k_L a_{ss}$ given by Eqn. 2.5. This can be seen by inspection of Eqn. 2.2, which is repeated below.

$$\frac{dC}{dt} = -k_L aC + k_L aC^*(t) - OUR \tag{5.1}$$

When OUR = 0 and there is a step change in C^* due to a change in the actuation gas, the time response of the dissolved oxygen follows an exponential whose time constant is the k_La (Eqn. 5.2. In steady state when C = 0, $k_La = OUR/C^*$. In this case, both results are the same and $k_La_{dg} = k_La_{ss}$.

The equivalence between the k_La measured using a dynamic gassing method, k_La_{dg}, through fitting the measured dissolved oxygen for a step change in C^* to a function of the form

$$C(t) = C^*(1 - e^{-k_La_{dg}t}) \tag{5.2}$$

and the k_La as defined by Eqn. 5.1 in steady state with C = 0,

$$k_La_{ss} = \frac{OUR_{max}}{C^*} \tag{5.3}$$

is not generally true for flat form factor bioreactors, where the oxygen concentration is not uniform inside the liquid. For this case, where the geometry is shown in Fig. 5-1b the appropriate physical model is

$$\frac{\delta C}{\delta t} = \frac{\delta}{\delta z}\left(D(z)\frac{\delta C}{\delta z}\right) - OUR \tag{5.4}$$

Where D(z) is the diffusion coefficient of PDMS (-d<z<0) or water (0<z<L).

The k_La extracted from a dynamic gassing measurement, k_La_{dg}, can be calculated by reducing Eqn. 5.4 into Eqn. 5.1 through an eigenmode expansion, keeping only the lowest order mode. For a PDMS membrane of thickness d, a water layer of thickness L, and a glass, oxygen impermeable base, we have

$$k_La_{dg} = D_w\lambda^2 \tag{5.5}$$

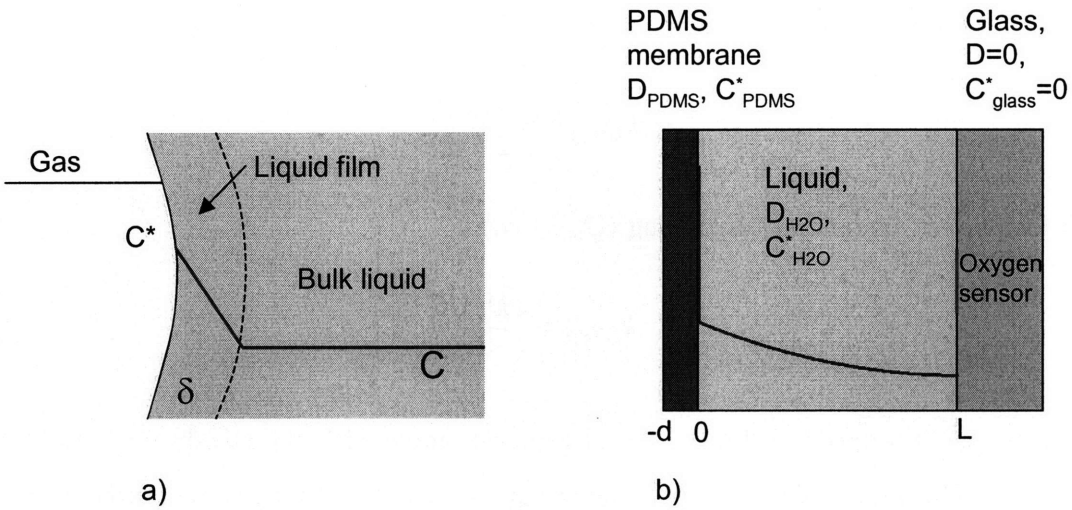

Figure 5-1: a) Schematic of all PDMS device model. b) Finite difference calculation of oxygen concentration at the bottom of the device for the all-PDMS case (dotted) and a glass bottom case (solid). Due to the absorption of oxygen into the bulk PDMS, a single exponential response is not observed in this case and dynamic gassing measurement of kLa is not possible. c) Zoom-in view of b) showing the single exponential response of the glass bottom case, allowing characterization of the kLa with the dynamic gassing method.

where λ is the smallest eigenvalue corresponding to eigenfunction solutions of the form

$$C_i(z) = \begin{cases} a_{i1}\cos(\lambda_i z) + a_{i2}\sin(\lambda_i z) & 0 < z < L \\ b_{i1}\cos(\sqrt{\frac{D_w}{D_p}}\lambda_i z) + b_{i2}\sin(\sqrt{\frac{D_w}{D_p}}\lambda_i z) & -d < z < 0 \end{cases} \tag{5.6}$$

Satisfying the boundary conditions determines λ through

$$\sqrt{\frac{D_w}{D_p}} K \tan(\lambda L)\tan(\sqrt{\frac{D_w}{D_p}}\lambda d) = 1 \tag{5.7}$$

where D_w (2.19×10^{-5}cm^2/s[86]) is the diffusion coefficient of oxygen in water, D_p ($2.15x \times 10^{-5}$cm^2/s[87]) is the diffusion coefficient of oxygen in PDMS, and K (0.3) is the partition coefficient, or ratio of oxygen saturation concentrations in water, C^*, (0.27mM[88]) and PDMS, C_p^*, (0.9mM) in an oxygen partial pressure of 0.21atm.

Two limiting cases are amenable to an analytical solution. When diffusion through

water (L≫d) is dominant we have

$$k_L a_{dg} \approx (\frac{\pi}{2})^2 \frac{D_w}{L^2} \tag{5.8}$$

and for perfect, instantaneous mixing ($D_w \rightarrow \infty$)

$$k_L a_{dg} \approx \frac{(D_p/K)}{Ld} \tag{5.9}$$

Note that the forms of Eqn. 5.8 and Eqn. 5.9 agree with the steady state cases from Eqn. 2.8 and Eqn. 2.8 This is important because it indicates that $k_L a$ measurements using dynamic gassing, with devices having the geometry shown in Fig. 5-1, will be representative of the $k_L a$ derived under steady state conditions, which indicate the maximum oxygen uptake rate that can be supported. Unfortunately, this is not the case for the devcies fabricated using the standard processs described in Chap. 3, where the bottom of the device is made of an approximately 3mm thick layer of PDMS. Because oxygen is soluble in the base layer, we find that reduction of the time response to a single lowest order eigenmode is no longer accurate, as there is a slow tail to the response due to the absorption and desorption of oxygen from the base layer.

This was verified using a finite difference calculation solution of Eq. 2.4 for the geometry shown in Fig. 5-2. Also shown in Fig. 5-2 are the time responses of the oxygen concetration at the bottom of the growth well for two cases, one where the bottom of the well is a thick PDMS layer (dotted) and one where the bottom of the well is glass and impermeable to oxygen (solid). This demonstrates the problem with using the dynamic gassing method on all PDMS devices. Because the bulk PDMS that forms the growth well absorbs a significant amount of oxygen, the time response measured at the bottom of the growth well has a slow component, and exponential fitting to the dissolved oxygen profile does not yield meaningful results and the $k_L a_{dg}$ is not well defined. In addition, the long time response, and parasitic oxygen absorption from the surrounding air, makes it very difficult to drive the dissolved oxygen concentration in the growth well to zero, which prevents a full scale change in the

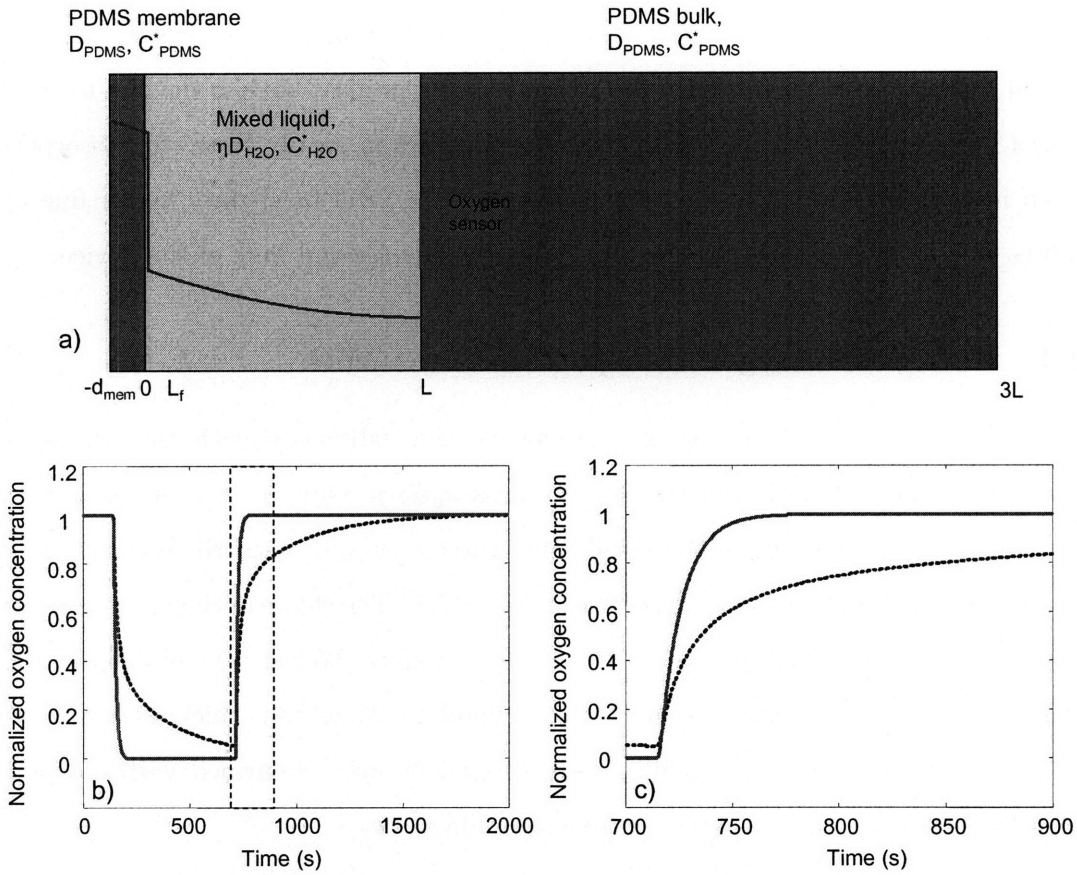

Figure 5-2: a) Schematic of all PDMS device model. b) Finite difference calculation of oxygen concentration at the bottom of the device for the all-PDMS case (dotted) and a glass bottom case (solid). Due to the absorption of oxygen into the bulk PDMS, a single exponential response is not observed in this case and dynamic gassing measurement of kLa is not possible. c) Zoom-in view of b) showing the single exponential response of the glass bottom case, allowing characterization of the kLa with the dynamic gassing method.

DO, which is helpful for sensor calibration. Thus, special devices where the bottom is made from glass are necessary to measure the $k_L a$ using the dynamic gassing method.

To summarize, for flat form factor bioreactors, where diffusion is significant in the oxygen transport, the $k_L a_{dg}$ measured using dynamic gassing methods is not the same as the steady state $k_L a_{ss}$ used to characterize the maximum supported oxygen uptake rate for a given saturation concentration. They are however approximately equivalent for devices where oxygen flux only enters through one surface, such as the glass bottom, geometry shown in

Fig. 5-1, but for some geometries, including the all-PDMS bioreactor devices, the $k_L a_{dg}$ is not well defined. We can however, use measurements in glass-bottom devices to estimate the $k_L a_{ss}$ in the all-PDMS bioreactor devices, becauses in steady state, the absorption of oxygen into the PDMS is not important. In fact, $k_L a_{ss}$ will be slightly higher due to the small (<15× membrane flux) oxygen flux through the base and bulk of the device.

5.1.1 Devices for oxygen transport measurements

The devices for oxygen transport measurements were fabricated with all-glass bottoms, made using 16mm×16mm×1mm die saw cut glass squares. Oxygen sensors were fabricated into the center of these devices by roughening the center spot with HF etchant and then depositing the PtOEP sensor, as described in Sec. 6.2.1. The shape of the mixing wells were 15mm×15mm with corners rounded with a 3.2mm radius. Well depths of 500μm, 750μm, 1000μm, 1500μm were fabricated into the same module. Membrane thicknesses were 70μm and 160μm for two separate modules. All dimensions were confirmed with independent measurements using a micrometer controlled probing stage.

5.1.2 Results

Oxygen transfer coefficients were measured for both devices under a variety of mixing conditions. Fig. 5-3 shows the measured dissolved oxygen profiles for the 70μm and 160μm devices when the actuation gas is switched between nitrogen and air with and without mixing, showing the quality of the single exponential fits, in agreement with the lowest order eigenmode expansion discussed in Sec. 5.1. Also, the dependence of the $k_L a$ with depth and the dramatic improvement in the $k_L a$ with mixing is evident.

The calculated $k_L a$ from Eqn. 5.5 and Eqn. 5.7 using the parameters shown in Tab. 5.1 as a function of well depth for the unmixed and mixed case are shown in Fig. 5-4, along with measurements from glass bottom devices with 500μm, 750μm, 1000μm, and 1500μm depths, and 70μm and 160μm thick membranes.

The agreement between theory and experiment is very good for the unmixed case, where

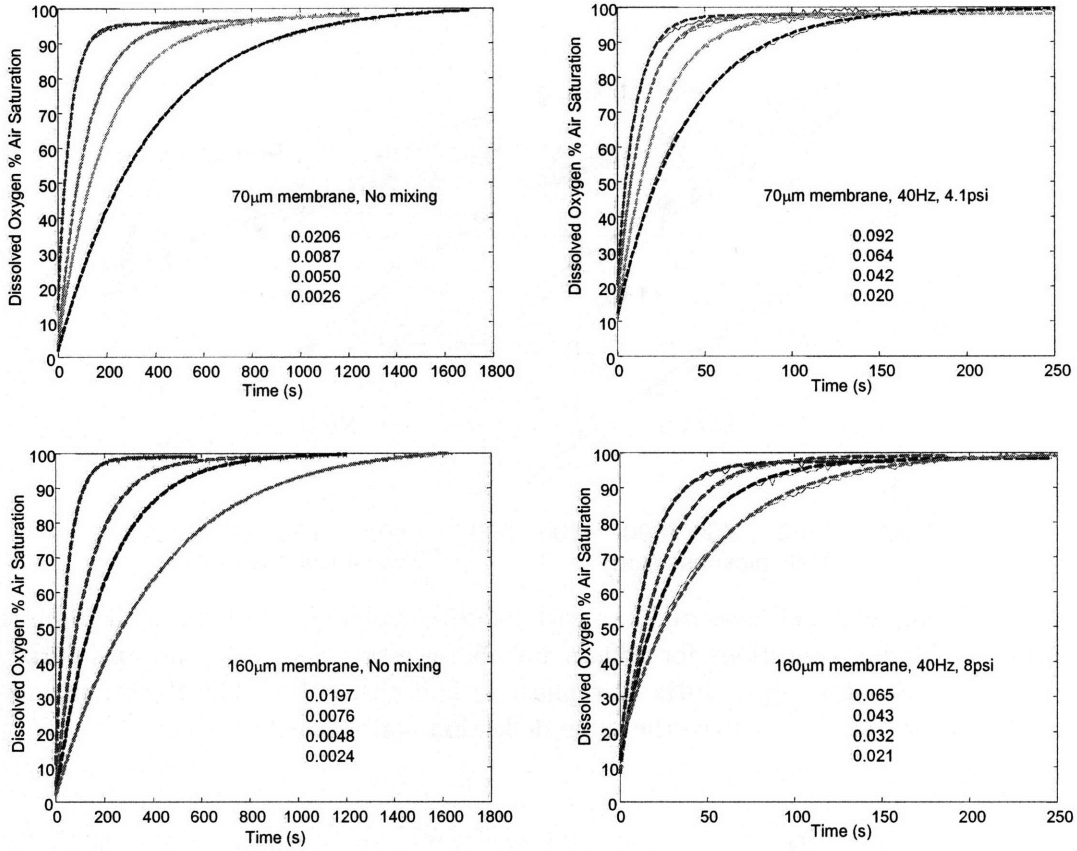

Figure 5-3: Time response of the dissolved oxygen concentration (solid) along with exponential fits (heavy dashed) for four different conditions. No mixing, and 20Hz, 40Hz, 60Hz, with 4.1psi actuation pressure.

there are essentially no fitting parameters. The average percent error is given in Tab. 5.2

For the mixed case, however, the measured $k_L a$ does not agree with the expected perfectly mixed $k_L a$, especially for the thin membrane. This was hypothesized to be due to imperfect mixing since only instantaneous mixing would result in the $k_L a$ calculated in Eqn. 5.9 and the lateral mixing times were on the order of 10 seconds.

In order to model imperfect mixing within the framework developed in Sec. 5.1, we use an effective diffusion coefficient by introducing a diffusion enhancement factor, η, such that $D'_w = \eta D_w$. This concept has been used previously to approximate transport in periodic, two dimensional flows [89],[90], and although the flow pattern inside the peristaltic

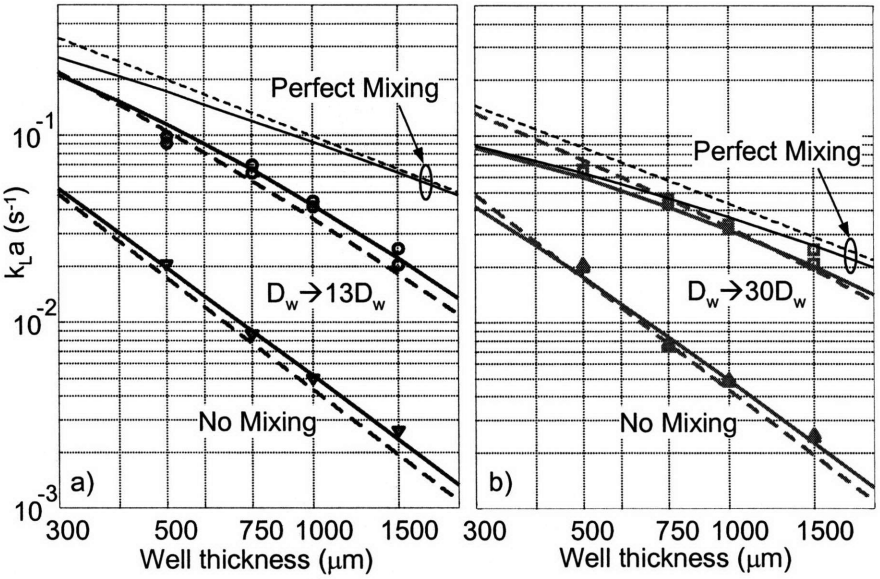

Figure 5-4: Comparison of measured k_La with model calculation for 160μm and 70μm thick membranes. Mixing conditions for 160μm membrane were 8psi-40Hz and 8psi-60Hz and for the 70μm membrane 4psi, 40Hz (2 replicates) and 4psi 60Hz. The thicker membrane required more pressure to achieve the same deflection and mixing efficiency.

	D_w (cm^2/s)	D_p (cm^2/s)	C_w^* (mmol/L)	C_p^* mM (mmol/L)	K	η
160μm	2.19×10^{-5}	2.15×10^{-5}	0.27	0.9	0.3	30
70μm						13

Table 5.1: Parameters for k_La calculation.

oxygenating mixer is likely more complicated due to the large membrane deflections, such an approach yields intuitively reasonable results, without the need for numerical solutions of the flow pattern inside the mixer.

The best fit diffusion enhancement factors were $10 < \eta_{70\mu m} < 16$ and $20 < \eta_{160\mu m} < \infty$ for the thin and thick membranes, respectively. Percentage errors are shown in Tab. 5.2. The thick membrane results are much less sensitive to imperfect mixing because the membrane contribution to the k_La dominated for diffusion enhancement factors above 20 and there would be little difference in the overall k_La with further improvements in mixing. For the

		500μm	750μm	1000μm	1500μm
Unmixed	160μm	-14.5	9.8	0.01	-9.6
	70μm	-3.8	4.1	3.4	-11.5
Mixed	160μm, $\eta = 30$	-6.3	-3.5	-1.6	-10.4
	70μm, $\eta = 13$	17.4	-1.1	-1.9	-5.9

Table 5.2: Percentage error between theory and experiment.

70μm thick membrane, where the actuation pressure was not as high, the k_La was limited by the mixing efficiency and therefore a narrower range of $\eta_{70\mu m}$ enveloped the measured data. The difference in η between the thin and thick membranes was the result of different mixing conditions due to different membrane deflections and actuation conditions for the two devices (70μm: 4psi, 40Hz, 160μm: 8psi, 40Hz). Overall, the improvement in k_La due to mixing is evident, with an average 8X increase in k_La for the 70μm thick membrane and 6.25X increase in k_La for the 160μm thick membrane.

These measurements were performed at room temperature with water with the primary purpose of validating the theory that formed the basis for the reactor design. The results can be applied to the all-PDMS microbioreactor devices with 500μm growth wells and 70μm thick membranes because the contribution of the 3mm thick bottom to the steady state oxygen flux is negligible. Assuming similar temperature dependencies for the diffusion coefficients and oxygen solubility for water and PDMS, the expected k_La_{ss} calculated by Eqn. 5.3 in the microbioreactors is $0.13s^{-1}$.

Dependence on mixing conditions

Because our model now incorporates conditions ranging from no mixing, $\eta = 0$ to perfect mixing, $\eta \rightarrow \infty$, we expect the k_La measurements to depend on any parameters that impact the mixing, including the volume of liquid injected into the well, which can vary due to the compliance of the mixing membrane, the actuation pressure, the well depth, and the actuation frequency. Mixing is affected by all of these parameters, because they impact the membrane deflection into the well per unit time. Fig. 5-5 illustrates the dependence of the

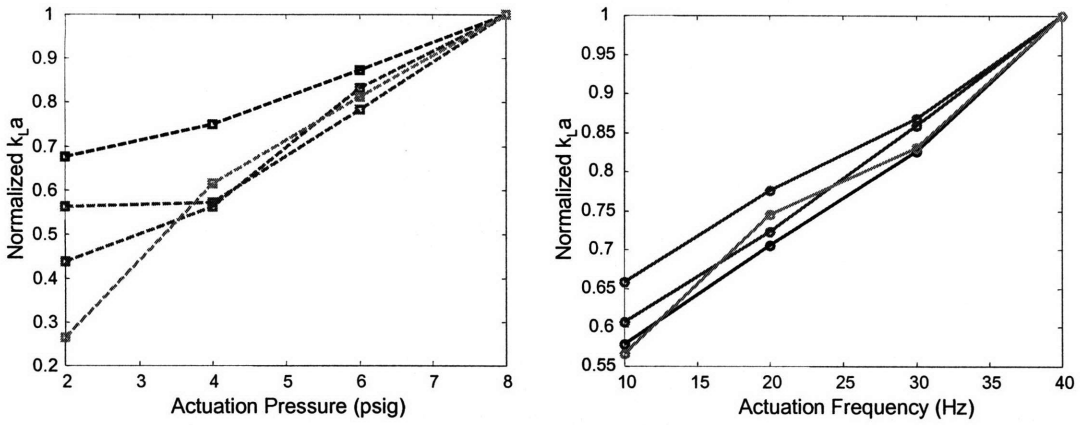

Figure 5-5: The k_La has been normalized to the maximum for each well depth for this figure. a) Normalized k_La vs. pressure for 160μm thick membrane device. b) Normalized k_La vs. actuation frequency for 70μm thick membrane. Increasing actuation pressure leads to increased k_La, as does increasing actuation frequency, presumably due to improved mixing.

k_La on actuation pressure in a 160μm thick membrane device and on actuation frequency in a 70μm thick membrane device. The k_La normalized to the highest pressure/frequency is shown for the four well depths of 500μm, 750μm, 1000μm, and 1500μm, indicating an approximately linear relationship between k_La and pressure/frequency.

Membrane deflection

The utility of variable width mixing tubes was indicated in 2.2.3 where narrower regions where the membranes deflect less provide paths for fluid to flow and generate more complex mixing patterns. To estimate the difference in deflection for these mixing membranes, we will use the same approximate solutions used for the fluid injector valves Eqn. 4.7 and represent the variable width membrane sections of each mixing tube as an individual rectangular membrane segment, as shown in Fig. 5-6. The load deflection curves for each mixing tube section are shown in Fig. 5-7 for two membrane thicknesses, 70μm and 160μm. The curves indicate that for each numbered mixing tube, there are membrane sections fully deflected and partially deflected for a 4psi actuation pressure and the 70μm membrane. For the 160μm membrane, at 4psi, the membrane deflection is much smaller, and for tubes 2

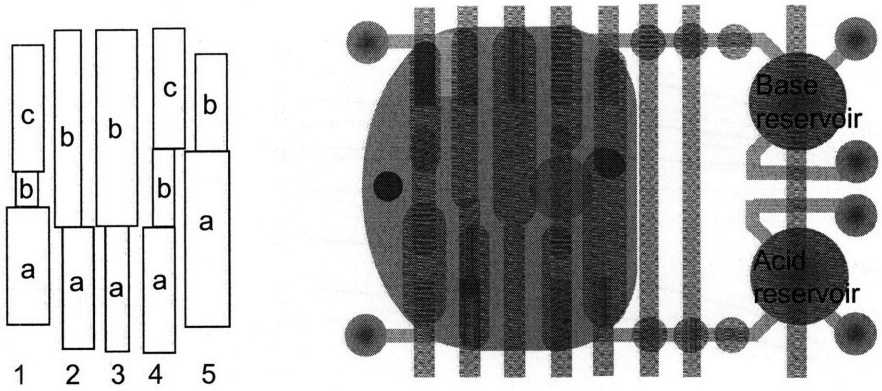

Figure 5-6: Approximation of variable width mixing tube membranes as individual rectangular membrane segments.

and 4, no segment is fully deflected. At 8psi, the deflections were comparable to the 70μm membrane, which was consistent with observed mixing efficiencies and k_La measurements with actuation pressure.

More detailed studies and optimization of the mixing tube patterns will require finite element calculations of the membrane deflection along with an improved understanding of fluid flow during mixing.

5.2 Dissolved oxygen control

Dissolved oxygen control is an important function to implement in the PIBA to achieve high cell density growth, especially in light of the limitations in the maximum k_La discussed in Sec. 5.1.2 and the requirements in Sec. 2.2.1. As the cell density increases, pure oxygen will be necessary to oxygenate the system. Because excessive concentration of oxygen is toxic to cells[91], pure oxygen cannot be used as the actuation gas during the entire fermentation. Rather, the oxygen concentration of the actuation gas should be increased to meet the demand.

In a conventional bioreactor system, the most common method for implementing DO control is to increase the agitation rate, or stirrer speed in response to deficiencies in the dissolved oxygen. Essentially, the k_La is controlled by modifying the agitation. One side

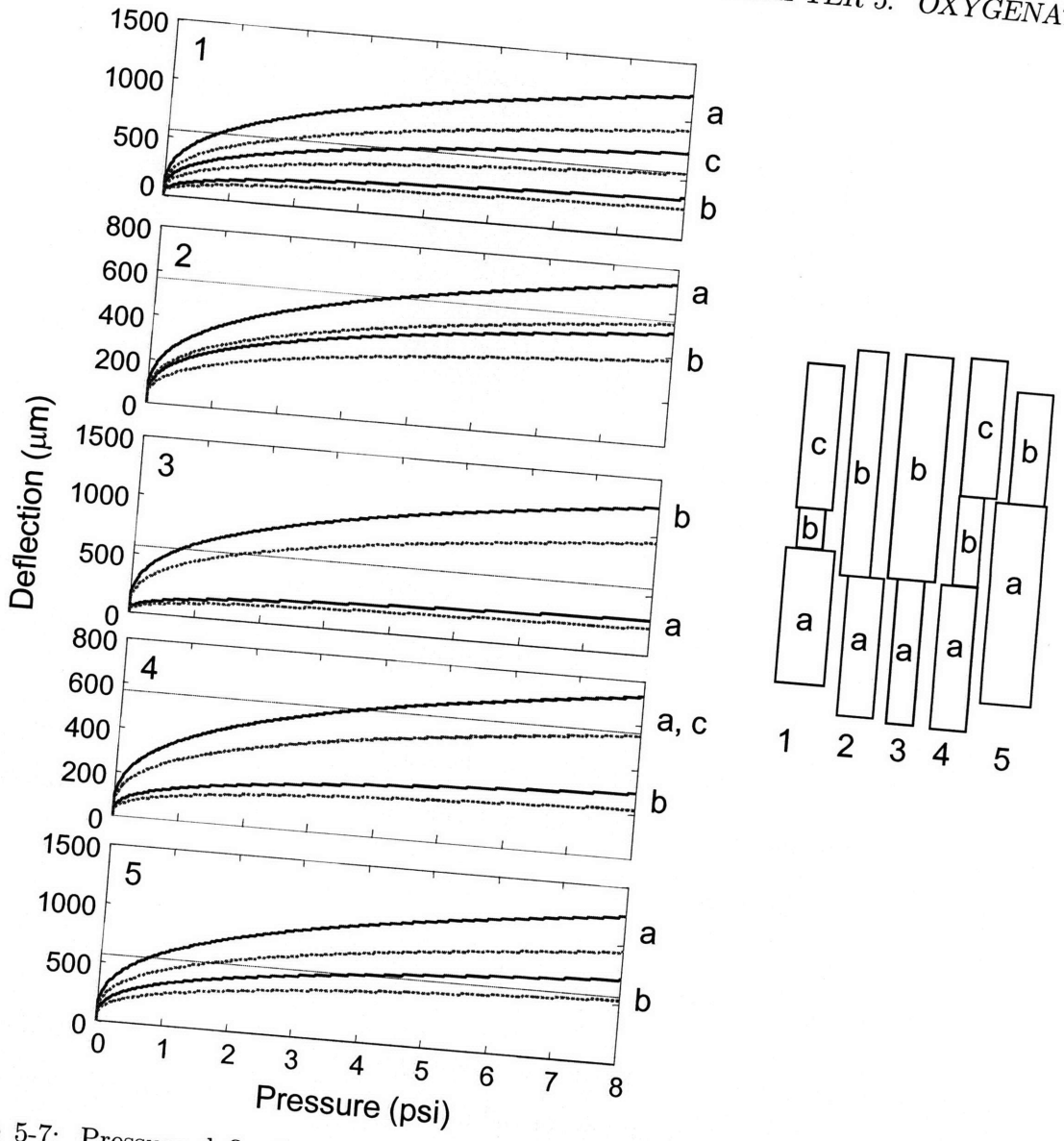

Figure 5-7: Pressure deflection curves for the mixing tubes approximated as individual rectangular segments. Solid line are results for a 70μm thick membrane and dotted lines are for a 160μm membrane. The dashed line indicates the well depth, which was measured to be 560μm. The membrane segment widths have enough variation such that each tube has fully and partially deflected segments, which encourages fluid flow transverse to the direction of peristalsis.

effect of this method of control is the shear forces on the cells is coupled to the oxygenation, which can complicate process development. When increasing the stirring speed is not suf-

ficient to meet the oxygen demand, pure oxygen is often added to the gas mixer through a gas mixing device. One reason why stirring speed is the primary actuator for a DO control system is the expense of using pure oxygen at a rate of a few liters per minute into a 5-10L bench scale stirred tank.

In the PIBA, because of the small working volume, the quantity of pure oxygen is relatively small and we will exclusively use the latter method in order to decouple the oxygenation with the physical forces experienced by the cells.

Because the mixing tubes of the individual bioreactors are shared in a given module, we are only able to implement DO control on a per module basis, meaning we can ensure that the minimum DO in any bioreactor does not go below a set threshold.

5.2.1 DO controller model

In order to avoid the expense of a gas mixing apparatus incorporating mass flow controllers, we have devised a simple and inexpensive method to implement a gas mixer. We simply use a 3-way solenoid switch whose normally closed port is connected to pure oxygen and normally open port is connected to air. By turning the swtich on and off at a few hertz, with varying duty cycle, the oxygen concentration of the pressure reservoir that drives the mixer can be adjusted. The duty cycle setting is determined by the output of a PID controller whose error signal is derived from the threshold DO and the minimum DO in all of the bireactors in a given module, and allows us to use the relatively imprecise gas mixer.

Parameters for the dissolved oxygen in the bioreactor can be derived using the model shown in Fig. 5-8. To model the dissolved oxygen concentration we use Eq. 2.2 and to model the saturation concentration at the air/membrane interface, we assume that it is proportional to the oxygen concentration in the reservoir, whose oxygen concentration is governed by Eq. 5.11

$$\frac{dC}{dt} = k_L a(C^* - C) - OUR \tag{5.10}$$

$$\frac{dC^*}{dt} = \frac{F}{V_R}(C_{in} - C^*) \tag{5.11}$$

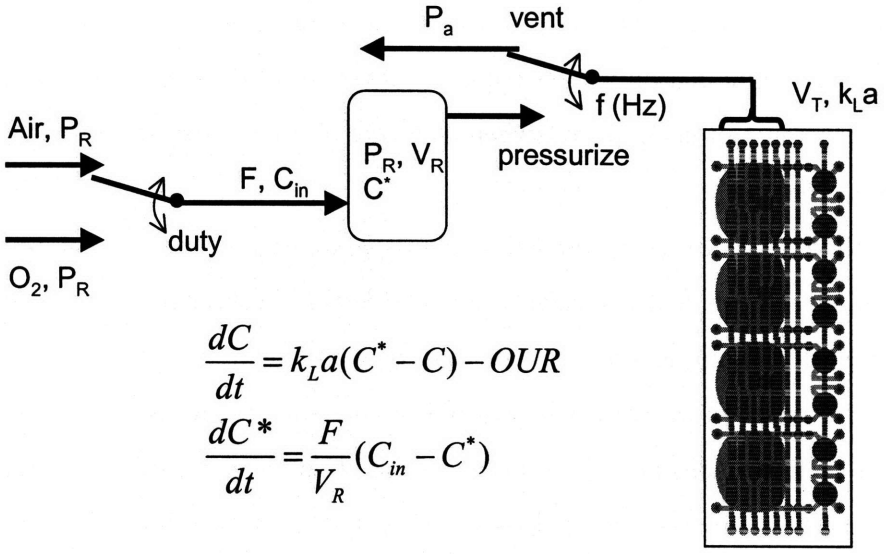

Figure 5-8: Model for dissolved oxygen controller. Objective is to maintain C above a setpoint by setting the duty cycle of the gas mixing switch which determines Cin. The gas mixer is characterized by the reservoir pressure, PR, the reservoir volume, VR, the flow rate F, and the input and reservoir oxygen concentrations, Cin and C*. F is determined by the mixing tube volume, VT and the mixer refresh frequency, f.

where F is the gas flow rate into and out of the reservoir at a pressure P_R, V_R is the volume of the reservoir, and C_{in} is the oxygen concentration at the input of the reservoir, which depends on the duty cycle of the gas mixer switch. Equations 5.10 and 5.11 describe a simple system with two real poles at $k_L a$ and F/V_R.

The gas flow rate, F, can be estimated from the average volume of the peristaltic mixing tubes, assuming an ideal gas. The moles of gas that fill a mixing tube at every actuation step is given by

$$\Delta n = \frac{(P_R - P_a)V_t}{RT} \tag{5.12}$$

where P_a is the normally open pressure of the mixing switches, R is the universal gas constant, and T the temperature. The flow rate is then the volume of gas that flowed into the mixing tube multiplied by the actuation frequency,

$$F = \frac{V}{\Delta t} = \frac{\delta n RT}{P_R} f = \frac{(P_R - Pa)V_t}{P_R} f \tag{5.13}$$

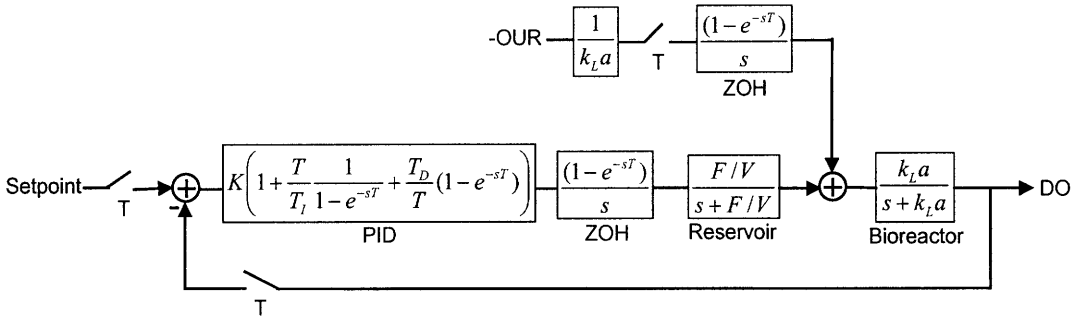

Figure 5-9: Block diagram of dissolved oxygen control model. T is the sampling frequency, K, TI, and TD are the PID controller parameters, ZOH is a zero-order hold, F/V is the dilution rate of the gas mixing reservoir, k_La is the oxygen transfer coefficient, OUR is the oxygen uptake rate. A sampler and zero-order hold is placed after the OUR in order to allow modeling as a discrete transfer function to calculate the response to a change in the OUR.

For a 4psi actuation pressure and 25Hz actuation frequency, the flow rate is approximately 1.1mL/sec.

A block diagram representing Eqns. 5.10 and 5.11 along with a PID controller is shown in Fig. 5-9, which can be used to calculate the discrete transfer function of the system from the setpoint to the output and a change in the oxygen uptake rate to the output. A few points deserve to be highlighted. The first is that the choice of PID parameters depends on the sampling time, the second is the k_La determines the magnitude of the initial error due to changes in the oxygen uptake rate, and finally the time response of the controller is insensitive to the k_La and F/V when the sampling period is longer than $1/k_L a$ and V/F.

That the PID parameters depend on the sampling time makes intuitive sense in that the maximum speed that the controller can respond to errors in the DO is the sampling time and any errors due in the duty cycle are essentially integrated over the sampling time. Thus, for a given sampling time, the PID gain must remain lower that a certain threshold to ensure stability. This is complicated by the fact that the error in the conversion between duty cycle and reservoir oxygen concentration, which depends on the relative pressure in the pure oxygen and air ports and flow resistance in these ports, is not precisely known and contributes directly to an uncertainty in the PID gain. Thus, we must choose the PID

parameters such that the system will remain stable and have a fast transient response over a range of gains and also sampling times, since this varies somewhat depending on how many fluid injections are required.

The $1/k_La$ dependence of the initial error in DO due to a step change in OUR is important because this indicates degree of error in the DO. The $1/k_La$ dependence arises because the OUR change occurs inside the bioreactor and the k_La determines the maximum rate the controller can respond. This highlights the importance of maximizing the k_La, even if oxygen demand could be met by using pure oxygen.

Because typical sampling times of 20-40 seconds are longer than $1/k_La$ and V/F, the response of the controller is dominated by how fast samples are acquired and not by the natural response time. As a result, typical response times of the controller are 100-300 seconds. This can be improved by decreasing the sampling time, at least for the oxygen sensors to 5 seconds, at the cost of increased photobleaching of the oxygen sensor.

5.3 DO control performance

Fig. 5-10 shows dissolved oxygen curves from two *E. coli* bioreactions that are described in more detail in Sec. 7.3 and Sec. 7.4. The light line is the minimum DO, which is the controlled variable and the heavy line shows the approximate oxygen concentration in the reservoir, C*, assuming the duty cycle of the gas mixer switch is exactly proprotional to the fraction of added pure oxygen. Fig. 5-10a shows data from a modified LB fermentation where the gas mixing reservoirs were approximately 70mL in volume leading to a flow rate to volume ratio of $0.01s^{-1}$ which gives a 100 second gas mixing limited response time. Consequences of the slow response are indicated by the large deviations from the setpoint precipitated by brief decreases in the oxygen demand. Fig. 5-10b, shows data from a defined medium fermentation where the gas mixer was modified to have a volume of only 0.75mL. In this case, the flow rate to volume ratio is approximately $1.4s^{-1}$ and the response time is limited by the sampling period of 40 seconds since the k_La of $0.1s^{-1}$ is high enough such that it is not limiting. In this case, the DO is maintained at approximately 40% air

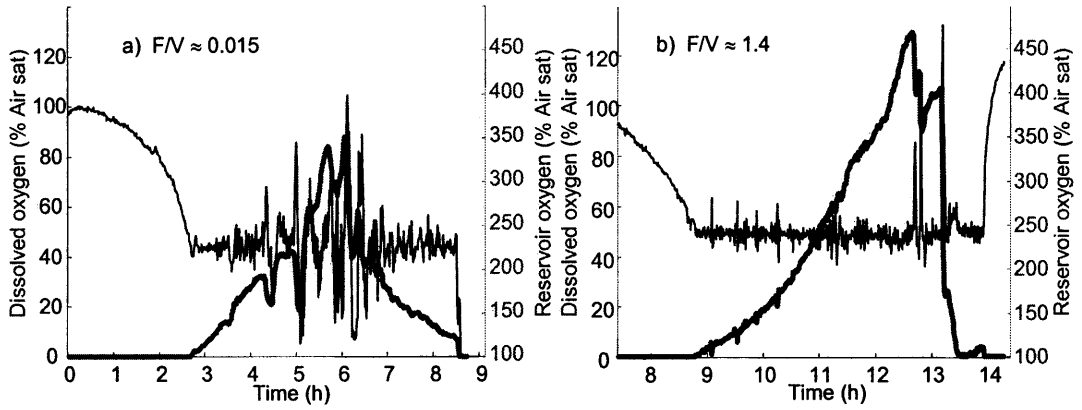

Figure 5-10: Minimum dissolved oxygen of four bioreactors in a PIBA module along with the approximate oxygen concentration in the oxygen reservoir, assuming that the duty cycle of the gas mixing switch is exactly proportional to the fraction of added pure oxygen. a) Large gas mixing reservoir, F/V≈0.015s^{-1}. b) Small gass mixing reservoir, F/V≈1.4s^{-1}

saturation after the controller is activated. The large spikes in the DO near hour 13 occur as the glucose is consumed in the different bioreactors and the oxygen demand decreases, and the recovery from these events is relatively fast.

5.4 Conclusions and future work

In this chapter we characterized the oxygen transport in mixed and unmixed flat form factor bioreactors and developed a dissolved oxygen control system for the PIBA system, capable of maintaining the dissolved oxygen in a module above a set threshold.

Given the results from Sec. 5.1, we can expect a k_La of approximately 0.1s^{-1}. With this k_La, assuming an oxygen uptake rate for *E. coli* of 20mmol/g-dcw/h[24], the system will be able to support growth up to 3.8 g-dcw/L (OD≈12)using air and 18.9g-dcw/L (OD≈58) using pure oxygen. This is short of our original design goal of 50g-dcw/L using pure oxygen, however it is still 2.5 times larger than previous microfabricated bioreactors.

Improving on this result will require improving the mixing efficiency of the devices, or fabricating thinner devices. A first step for improving mixing will be to understand the fluid flow inside the mixer and how it may be impacted by different membrane section

design. Key to this process would be a method to image the velocity field of the fluid inside the bioreactor, perhaps using particle imaging velocimetry. Beyond that, more accurate numerical modeling of the device may yield additional insigh.

Although the performance of the DO controller was much improved over existing DO control schemes for microfabricated bioreactors, because of small differences in the culture conditions in each bioreactor in a module, the dissolved oxygen was only controlled in one reactor per module, while the other reactors experienced excess oxygen, resulting in a rising dissolved oxygen concentration. While this did not appear to be detrimental to cell growth, it is clearly not desirable, especially if different growth media are to be used. Individual DO control capability would be a significant upgrade in the capability of the PIBA. This would simplify interpretation of experimental results, offer better repeatability of experiments, and avoid excessive dissolved oxygen in reactors operating under slower growing conditions.

This can be accomplished using a modified mixing tube architecture that provides isolated gas exchange for each individual reactor, but shared peristaltic actuation, as shown in Fig. 5-11. The mixing tubes are now a singly connected structure with membrane pinch valves on either side. To pressurize a mixing tube, the output side valves are closed while the input side valves are opened. To vent a mixing tube, the input side valves are closed and the output side valves are opened. This architecture has the added advantage of allowing input and output gas concentration measurements for estimation of the oxygen uptake rate, and also carbon dioxide generation.

Its implementation will require adding a device layer and a single gas mixing switch per bioreactor, with ten peristalsis valves that to be shared across all bioreactors. Fortunately, this scheme has better scaling properties as well since the actuation control valves can now be shared among all bioreactors.

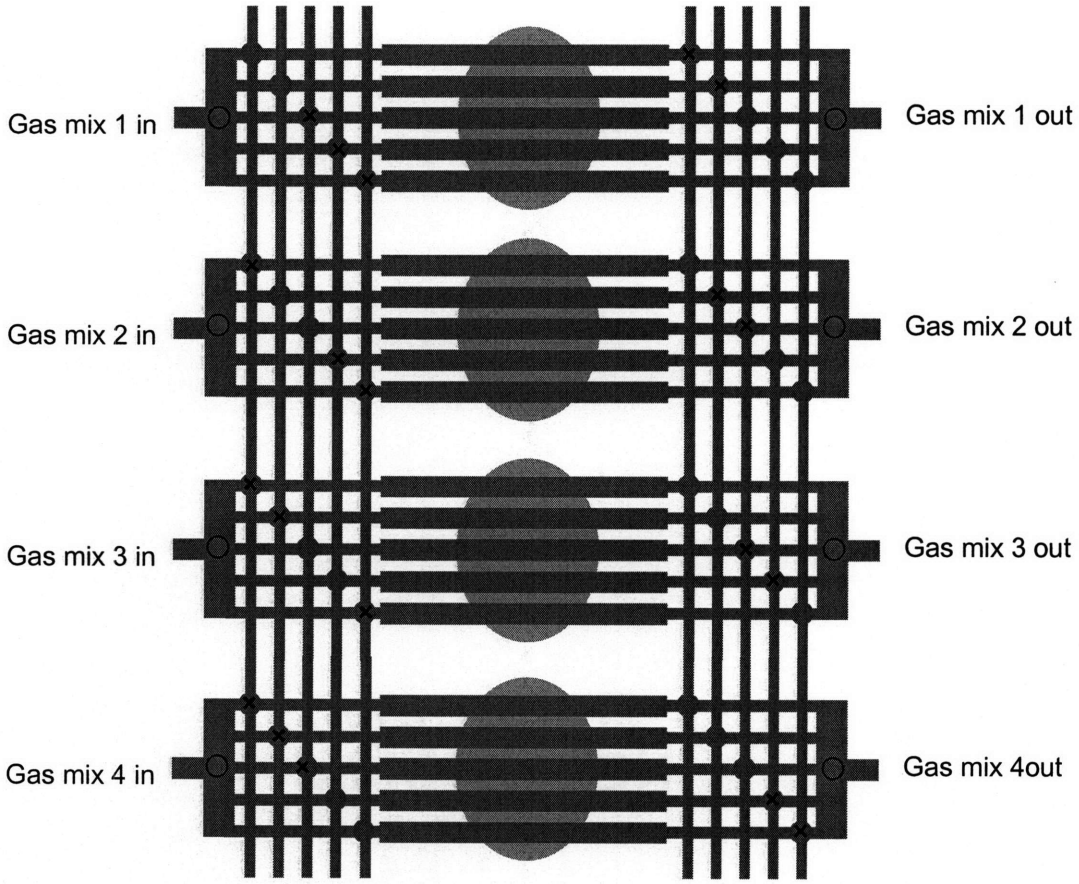

Figure 5-11: Oxygenating mixer architecture to allow independent dissolved oxygen control. Each reactor has independent input and output for the actuation gas, which can be independently controlled. Peristaltic mixing is accomplished by opening and closing (X) valves on either side of the mixing tube, as indicated. The number of valves required, is 10 + X, where X is the number of independently controlled oxygenation conditions. Oxygen uptake rate can be estimated by comparing the oxygen concentration of the input and output gas. In the diagram, the X indicates a closed valve and illustrates a sequence of valve closing by which the same approximate peristalsis pattern is achieved. Note that in actual operation, the state of each control valve would be the same across a module.

Chapter 6

System architecture and scaling

In Chapter 2 we described the rationale for exploring microfabrication technologies to realize a bioreactor array system. Parallel fabrication of complex functions in an integrated device that could be scalable to large numbers of reactors was a key motivator. Just as a microprocessor integrated circuit requires supporting external components and subsystems to build a useful system, such as a personal computer, microfluidic devices require supporting systems to realize their usefulness. In this chapter, we will discuss the macroscopic supporting subsystems that support the PIBA module and impact the scalability of the system.

6.1 Pneumatic actuation scheme

The peristaltic oxyenating mixer requires pneumatic actuation of its deflectable membranes, as do the membrane pinch valves. As mentioned in Sec. 2.3.2, pneumatic switches are the most expensive resource in the system and should be shared as much as possible. This is illustrated in Fig. 6-1 which shows the logical pneumatic connections to to PIBA modules.

The mixing tubes are shared among four reactors in a module, requiring only five pneumatic switches to actuate twenty mixer sections, plus one gas mixing switch, requirng a total of 6 switches per oxygenation condition. However, as discussed in Sec. 5.4, the sharing

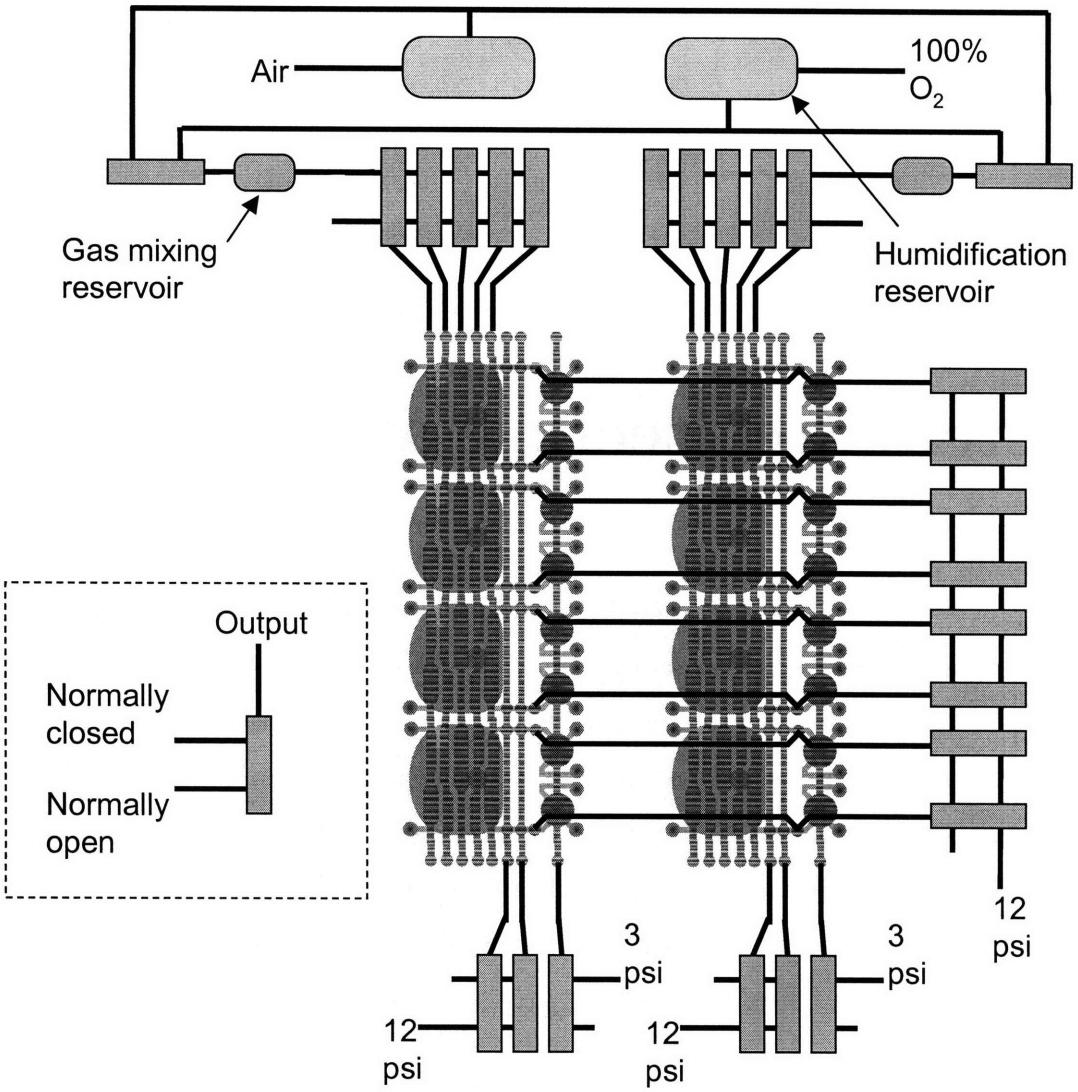

Figure 6-1: The pneumatic switches that control the pressure of the actuation lines are shared between multiple bioreactor modules, as indicated by the lines connecting the actuation ports, such that the required number of pneumatic switches scales as 3M + 2R + 6X, where M is the number of modules, R is the number of bioreactors per module, and X is the number of oxygenation conditions. This compares with 7MR pneumatic switches if there were no sharing between individual reactors. The current configuration, which supports eight bioreactors, requires 24 switches.

did limit the flexibility of the DO controller.

The valves for the fluid injectors are shared in a way to allow near optimal use of the

pneumatic switches. Each fluid injector reqires four pneumatic signals, three for the valves over the injector channel, and one for the pressure reservoir. As shown in Fig. 6-1, two of the channel valves and the pressure reservoir are shared along each module, while the third is shared across each module. Thus the fluid injectors require $3M + 2R$ switches to operate, where M is the number of modules and R is the number of bioreactors per module. An optimally shared case could eliminate two pnuematic switches by sharing the pressure reservoir switch and last channel valve switch between modules. Individual control would still be allowed through a combination of the first and middle channel valve.

6.2 Optical sensors

The optical sensors used to measure physical parameters such as dissolved oxygen and pH are based on fluorescence measurements, while the optical density measurements are based on light scattering. Their basic principles of operation and measurement techniques are described in the following sections.

6.2.1 Dissolved oxygen

In the dissolved oxygen case, a single dye, Platinum-octa-ethyl-porphyrin (PtOEP) dissolved in polystyrene [48] is used. Because the fluorescence is quenched by molecular oxygen, the amount of fluorescence is related to the amount of dissolved oxygen. The fluorescence quenching can be modeled with a simple first order differential equation, assuming that the excitation is weak and the absorption does not saturate.

$$\frac{dN^*}{dt} = P - \frac{N^*}{\tau_o} - K[O_2]N^* \tag{6.1}$$

where N^* is the concentration of excited state dye molecules, P is the rate at which molecules are pumped into the excited state, τ_o is the excited state lifetime with no oxygen, and $K[O_2]$

is the quenching frequency. From Eq. 6.1, we can see that the quenched lifetime is equal to

$$\tau = \frac{\tau_o}{1 + \tau_o K[O_2]} \tag{6.2}$$

The dynamics described by Eq. 6.1 is captured by the transfer function.

$$H(\omega) = \frac{\tau}{j\omega\tau + 1} \tag{6.3}$$

We can easily see from Eqns. 6.2 and 6.3 that the ratio of the unquenched and quenched intensity is equal to the ratio of the unquenced and quenched lifetimes which is linear in the oxygen concentration,

$$\frac{I_o}{I} = \frac{\tau_o}{\tau} = 1 + \tau_o K[O_2] \tag{6.4}$$

which is the Stern-Vollmer relationiship for fluorescence quenching.

From Eq. 6.4 we can measure the oxygen concentration by fluorescence intensity ratios or lifetime ratios. In practice, the former requires careful normalization of the intensity to ensure that other factors do not influence the measured fluorescence. For measurements inside of a bioreactor, this proves difficult due to the changing scattering conditions as the cell density increases. For this reason, we are more interested in fluorescence lifetime based measurements, as they are theoretically insensitive to amplitude variations. Direct measurements of the lifetime are not simple to do. In the frequency domain, the transfer function can be sampled in frequency and the data fit to a modified version of Eq. 6.3, where an additive constant to account for a contribution from autofluorescence with short lifetime from color glass filters.

$$H_{fit}(\omega) = \frac{\tau}{j\omega\tau + 1} + \beta \tag{6.5}$$

An example is shown in Fig. 6-2 where the transfer function for fabricated PtOEP in polystyrene sensors is compared to the transfer function for a commercially available fluorescence sensor (Presens PSt3). Measurements were performed by modulating a 380nm

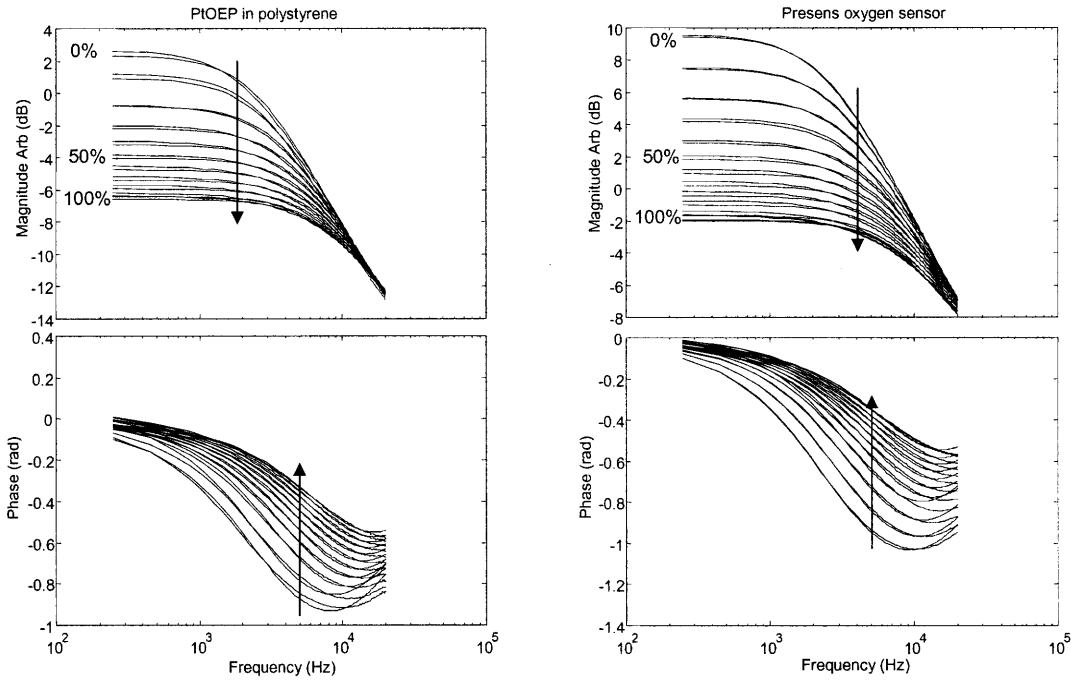

Figure 6-2: Frequency response for a range of oxygen concentration spanning 0% to 100% air saturation in 10% increments for a) PtOEP in polystyrene oxygen sensors and b) commercially available oxygen sensor from Presens (PSt3). Dashed lines are theoretical fits to a single pole with additive constant model (see text).

LED for a series of frequencies and measuring the magnitude and phase of the detected fluorescence using the system to be described in Sec. 6.2.4. The magnitude and phase of the modulated LED was also measured and used as the reference magnitude and phase to calculate the transfer function. The oxygen concentration was varied by using a gas mixing switch similar to the one used in Sec. 5.2.1 for the dissolved oxygen control. The results from the parameter extraction are shown in Fig. 6-3 where Eq. 6.4 is plotted versus oxygen concentration. The unquenched lifetime is 56μs for the PtOEP-ps sensors and 59μs for the Presens sensors. The quenching coefficient, K = 443 [1/%Air Sat] for the PtOEP-ps sensors and K = 409 [1/%Air Sat] for the Presens sensors.

Measurement of the entire transfer function in order to estimate the dissolved oxygen concentration is not practical. Instead, we will estimate the dissolved oxygen concentration from phase measurements at a single frequency, chosen to give the best sensitivity. For the

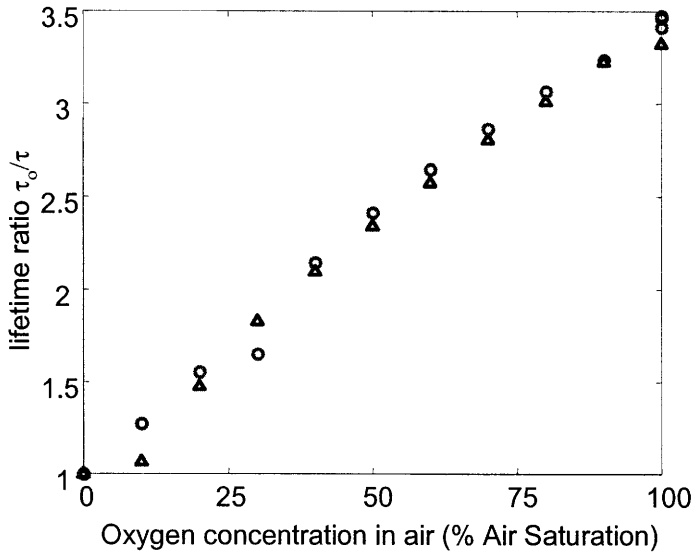

Figure 6-3: Stern-Vollmer plot of lifetime ratio extracted from the single pole model fits for both the PtOEP in polystyrene sensors (circles) and the commercial Presens (PSt3) sensor (triangles). The relationship is approximately linear, as expected from theory, with the dominant error likely due to the inaccuracy of the oxygen concentration. The unquenched lifetime is 56μs for the PtOEP-ps sensors and 59μs for the Presens sensors. The quenching coefficient, K = 443 [1/%Air Sat] for the PtOEP-ps sensors and K = 409 [1/%Air Sat] for the Presens sensors.

PtOEP-ps sensors, 5kHz works well and is indicated by the upward arrow in Fig. 6-2.

6.2.2 pH

The optical pH sensors are also fluorescence based, however the mechanism is different than fluorescence quenching. The sensor used two dyes, one that is pH sensitive and one that is not. The pH sensitive dye has a short lifetime ($\approx$10ns) and a different absorption and emission spectrum in its protonated and deprotonated form. The resultant fluorescence is more intense under basic conditions (pH>7) and almost completely gone under acidic conditions (pH<4). Because the lifetime is so short, a frequency domain phase measurement would require a modulation frequency on the order 15MHz, and require expensive, high speed detection electronics. Used alone, intensity based fluorescence measurements would have the same internal referencing problems as the oxygen sensors. This problem was

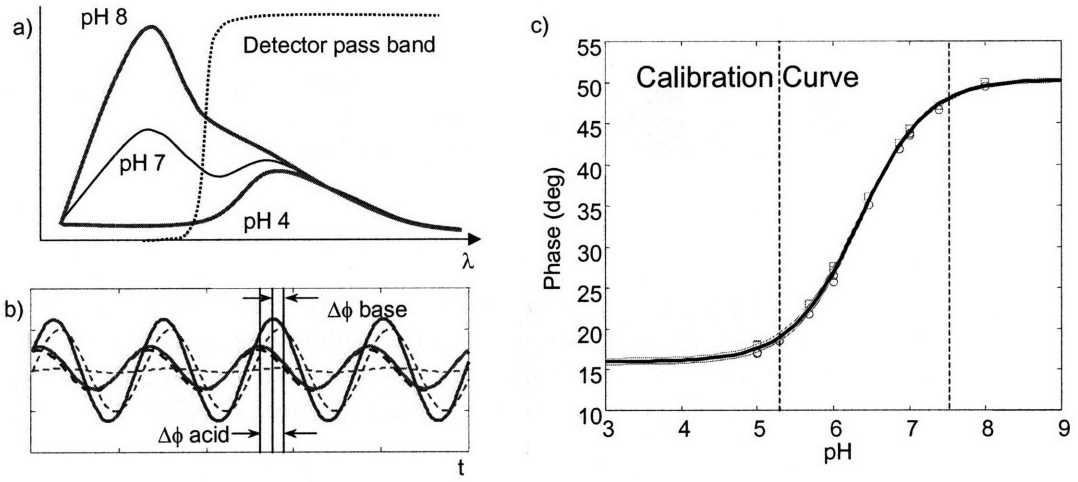

Figure 6-4: Optical pH sensor from Presens. a) Schematic of fluorescnece spectrum of two dyes for different pH. Optical filter selects the appropriate amount of both dyes to give a good phase shift vs. pH. b) Schematic of fluorescence for sinusoidal excitation. Dashed lines represent the fluorescence of the individual dyes. Solid lines are the total sum fluorescence, showing different phase shift for different pH. c) Calibration curve for the pH sensors. Note, $-\Delta\phi + \phi_o$ is shown to make the phase proportional to the pH.

overcome by [92] using a technique known as dual lifetime referencing, where a second dye, insensitive to pH, but with a long lifetime ($\approx 5\mu$s) is incorporated into the sensor with the same excitation spectrum and a similar emission spectrum. As the amplitude of the pH sensitive dye, with short lifetime changes, a phase change is measured in the combination fluorescence. This method allows a single excitation wavelength and simple wavelength independent fluorescence measurements to accomplish internal amplitude referencing. For these sensors, an optimal measurement frequency is 45KHz, and the resulting calibration curve of pH vs. phase for a number of different sensors is shown in Fig. 6-4. The tightness of the calibration curve points to the superb quality of these commercial pH sensors.

6.2.3 Optical Density

Optical density measurements are used to indicate the cell density. It is performed using two 1mm PMMA optical fibers configured as shown in Fig. 6-5. The collection fiber is configured with two 500μm pinholes separated by approximately 1cm to limit the numerical aperture

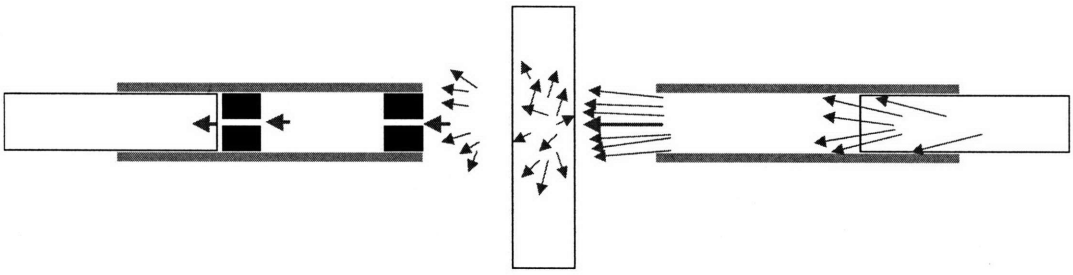

Figure 6-5: Low numerical aperture optical density measurement. Scattering transfers power into a larger solid angle. By collecting the smallest solid angle possible, we reject as much scattered light as possible and only measure the attenuated incident light, giving a much wider linear correlation between optical density and density of scatterers.

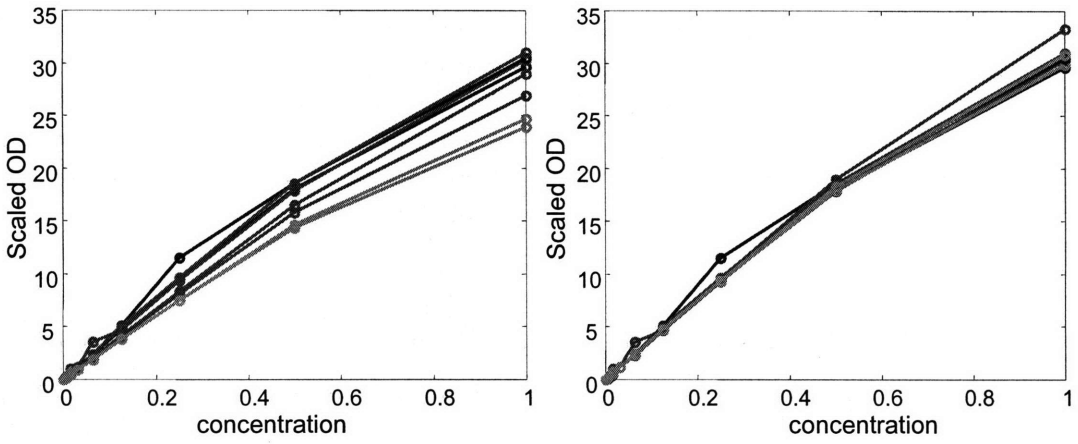

Figure 6-6: Optical density vs. concentration of polystyrene spheres (normalized) standard curve. a) Raw data scaled assuming a 500μm thick path length. b) Path lengths scaled for best agreement.

($\approx$0.05) captured by the fiber. This minimizes the detection of scattered light as opposed to light that passes through the medium without scattering and maximizes the linear range over which the optical density is proportional to the cell density [50]. Measurements are performed using the same phase sensitive detection algorithm, except the magnitude is of interest instead of the phase. The 650nm LED excitation is modulated at 4kHz. Fig. 6-6 shows a calibration curve for the optical density generated by making serial dilutions of a suspension of 1μm diameter polystyrene spheres. Because standard optical densities are scaled to a 1cm path length, the measurement is sensitive to errors in the thickness of the

medium. For this reason, it is typically necessary to perform an endpoint optical density using a diluted sample and a 1cm path length.

Calibration between optical density and dry cell weight (dcw) was performed by taking four 50mL samples from a 4L bioreactor, measuring the optical densities, and then centrifuging and resuspending the cells in water three times. After drying more than 24 hours in a vacuum oven, the dry cells were weighed giving a conversion factor of 0.33 $\pm$ 0.006 g-dcw/OD.

6.2.4 Phase sensitive detector

Phase sensitive detection is a well established technique for sensitive measurements of low level signals. The sensitivity is achieved by reducing background by measuring a modulated signal in a narrow bandwidth. Phase sensitivity is achieved by downconverting the modulated signal with two sinusoids phase shifted by 90° with respect to each other, orthogonal basis functions of a sinusoid with any phase. For our application, we are interested in implementing high performance phase sensitive detection using inexpensive electronics, including a single 100KHz A/D converter, electronic multiplexer, and simple unstabilized oscillator.

The phase sensitive detection algorithm is shown in Fig. 6-7. The fluorescence and reference are sampled together by interleaving and using the same analog to digital converter. The sampling frequency is approximately 21kHz, which was purposely chosen to be detuned from the 5kHz modulation frequency to prevent harmonics of the modulated signal from aliasing in band since there is no anti-aliasing filter in this inexpensive data acquisition hardware (NI6035 DAQ card). The modulation frequency is then detected using a simple FFT based algorithm to set the passband of two discrete time bandpass filters used to remove harmonics from the signal to prevent their down conversion to DC through aliasing. The 90° phase shifted reference is obtained through the hilbert transform of the filtered reference signal. The signal is then downconverted by both the in-phase and quadrature reference and low pass filtered and the inverse tangent of the ratio of the quadrature to the

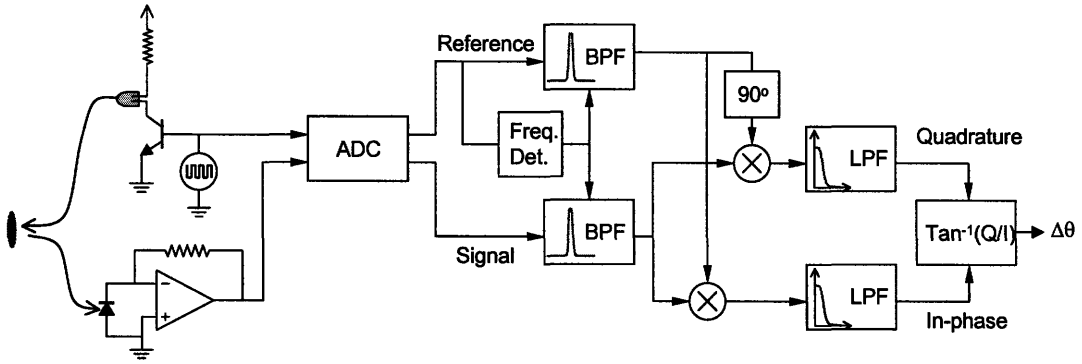

Figure 6-7: Block diagram of phase detector for fluorescence quenching sensors. Sampling of reference and signal is interleaved to correlate the phase noise of reference and signal. Band-pass filtering removes harmonics to avoid spurious components in the detected phase. Multiplication of signal with reference and Hilbert transformed reference gives the In-phase and Quadrature components after low-pass filtering. Inverse tangent of Q/I gives the phase shift of the signal with respect to the reference.

in-phase component yields the phase.

This algorithm, uses the measured reference directly in the down conversion as opposed to generating a pure sinusoid phase locked to the reference because it ensures the phase noise of the reference, which modulates the LED and thus appears in the fluorescence signal is used to demodulate the signal, resulting in its approximate cancelation. Perfect cancellation is not achievable using the present hardware because the signal and reference are not simultaneously sampled with two A/D converters.

6.3 Optical sensor addressing

An important consideration for the optical sensing scheme is how to read out all of the data. Because each bioreactor must have dissolved oxygen, pH, and optical density measurements, the number of sensors scales directly with the number of bioreactors, a condition, as pointed out in Sec. 2.2, dictates that the optical readout should be batch fabricated.

At the time of writing, a suitable batch fabricated optical addressing technology has not been developed. Properties of an ideal system and some prospects will be discussed in

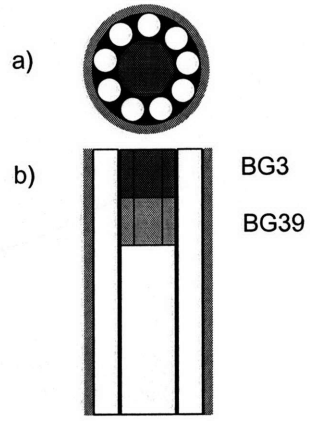

Figure 6-8: Fiber bundle used to address optical sensors. a) End on view, b) cutaway cross-section. The 1mm excitation fiber is filtered at the distal end using 1mm hexagons of BG3 and BG39 color glass filters. The nine 500μm collection fibers surround the excitation fiber. The interstitial space is filled with carbon black loaded silicone to prevent cross talk between the excitation and collection fibers.

Sec. 6.4. Instead, polymer optical fiber bundles were constructed as shown schematically in Fig. 6-8 The fiber bundles consist of a 1mm, central excitation fiber that terminates in two colorglass filters to block parasitic long wavelength emission from the LED. Surrounding the excitation fiber are nine 500μm collection fibers to capture the fluorescence. For this fiber bundle configuration, there is an optimal distance from the sensor. If it is too close to the surface, the illuminated area does not overlap the collection area of the collection fibers and if it is too far away, the collection efficiency decreases. This is shown in Fig. 6-9 indicating an optimal distance of approximately 1mm. The PIBA module is fabricated such that 1mm of PDMS separates the sensor from the bottom surface of the fiber bundle recess.

6.4 Scaling challenges and strategies

The current PIBA supports eight simultaneous bioreactions with independent pH control and per module dissolved oxygen control. While eight reactors is a step in the right direction, a throughput upwards of 64 or 128 reactors would have a much larger impact,

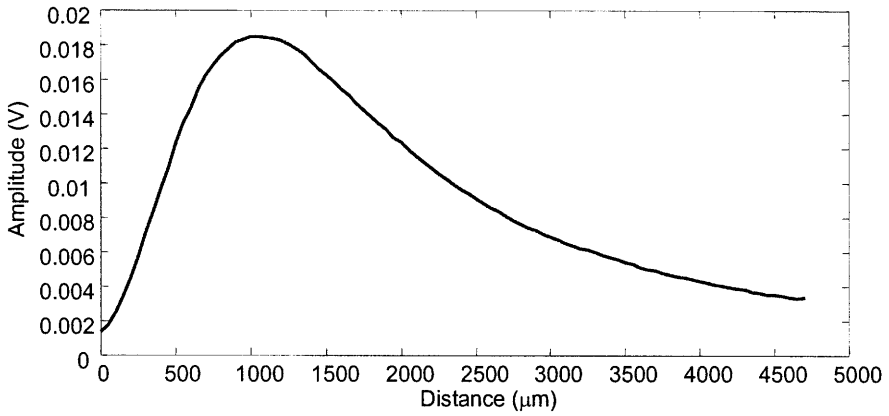

Figure 6-9: Fluorescence signal vs. distance from fiber bundle. Optimal distance is approximately 1mm.

especially when considering replicates of experiments are often desired, and that for a full combinatorial study of three parameters with ten levels would require one thousand experiments.

Suppose our objective is to implement a 64 or more reactor system with four fluid injectors per reactor, with individual DO control. How would the macroscopic resources such as pneumatic switches, LED's, and photodetectors scale?

6.4.1 Pneumatic actuation

With four fluid injectors per reactor, we need to control $64 \times 4 \times 3 = 768$ valves along with $64 \times 4 = 256$ pressure reservoirs, which is clearly a daunting task. One way to save pneumatic switches is to implement a row-column style addressing, where the valve closest to the reservoir in each injector is individually controlled along a module, but shared between modules, and the second valve is shared along a module and individually controlled between injector columns, requiring two per module. To reduce the probability of leakage, we will add some overhead and control the valve closeset to the growth well and the pressure reservoirs with two switches per module. This scheme requires 4 switches per module and 2 switches per reactor in a module for a scaling that goes as $4M + 2R$. To choose M and R, we wish to minimize $4M + 2R$ while satisfying $MR = 64$, subject to M and R integers.

This leads to M = R = 8 for a total of 48 switches. Note that the constraint that M and R be integers while satisfying MR=64 is overly constraining and the total number of reactors can be increased to 72 while maintaining 48 switches by choosing M = 6 and R = 12.

For the dissolved oxygen, using the scheme for individual pH control proposed in Sec. 5.4, we would require a single gas mixing switch for each reactor along with 10 switches for each actuation frequency we desire for a scaling that goes as $MR + 10X$. For a single actuation frequency the total would be 74 switches for 64 reactors or 82 switches for 72 reactors. In addition, we would require a variable duty cycle square wave oscillator for each gas mixing switch

In total, we would require $48 + 74 = 122$ pneumatic switches to support 64 reactors, or 130 pneumatic switches to support 72 reactors, with a scaling law that goes as $4M + 2R + MR + 10X$ pneumatic switches for MR independently controlled bioreactors. Considering that we have $21MR$ total deflectable membranes to actuate with air pressure, or 1512 for 72 reactors, 130 is a manageable number.

6.4.2 Optical sensors

Optoelectronics

A 64 reactor system will require 128 fluorescence measurements and 64 optical density measurements. If we choose to implement inlet and outlet oxygen concentration monitoring, the number grows to 256 fluorescence measurements. The current configuration uses one LED for each fluorescence and optical density measurement with a single oscillator for the dissolved oxygen (5kHz), pH (44kHz), and optical density (4kHz). On the detection side, there is one photodetector for every two fluorescence sensors because the collection fibers from two sensors are routed to a single photodetector.

Optical routing

While there is considerable flexibility and options for optimizing the optoelectronic scaling, optical routing offers more limited choices. Using optical fiber bundles for a 64 reactor

system rapidly becomes impractical. The sheer volume of optical fibers (128 bundles, 128 individual fibers) becomes difficult to handle, and use up a considerable amount of space due to the minimum bend radius of approximately 2 inches, not to mention the expense in manually fabricating them.

The solution to this problem will be to develop a batch fabrication technique for large core multimode waveguides. These structures would need to be able to direct and collect light out of the plane of the waveguides for easy interfacing with the PIBA modules. In addition, the fabrication process should be fully three dimensional and allow waveguides to cross under/over each other, allow integration of optical filtering for fluorescence excitation and collection, and provide for efficient coupling of LED excitation into them.

6.4.3 Additional considerations

To achieve better scaling of the macroscopic components, the primary tradeoff has been to give up parallel operation of the fluid injectors and optical sensors in favor of serial multiplexing in time. The degree to which this can be done is limited, however, by our desire for closed loop control over the growth parameters. As we saw in Sec. 5.2.1 the performance of the DO controller was tightly linked to the sampling rate. Generally speaking, the larger the sampling time, the smaller the controller gains and the slower the response of the system, allowing large deviations from the setpoint during disturbances.

Chapter 7

Bioreactor validation

In previous chapters, we described the functional elements of the parallel integrated bioreactor array, along with the design and scaling of the overall system. In this chapter, we will compare the cell culture process using conventional methods with the PIBA and discuss a series of cell culture experiments demonstrating the functionality of the system.

7.1 Conventional cell culture vs. PIBA

For the non-biologist, the following is a detailed description of a bench scale (2-10L) fermentation process.

1. From a frozen stock solution of the microbial strain to be cultured, streak on an agar plate to allow the isolation of a single colony. Cultivate the plate for 48-72 hours at the optimal growth temperature.
2. Prepare liquid medium to culture the cells. (4 hours)
3. Calibrate pH sensor. (30 min)
4. Assemble the bioreactor. (30 min)
5. Fill the bioreactor with the final growth medium, excluding components that will not be autoclaved. Prepare the bioreatctor for autoclaving. (1 hour)

6. Autoclave the bioreactor (3 hours) and allow it to cool. (8 hours)

7. Grow a starter culture in 7mL of Luria-Bertani medium in a roller tube until the optical density equals one. (4-6 hours)

8. Dilute 20:1 into 125mL of the final growth medium and grow in a shake flask until the optical density equals one. (4-6 hours)

9. Calibrate the dissolved oxygen sensor and prime the pH controller. (1 hour)

10. Add remaining medium components and innoculate the bioreactor with the shake flask culture. (15 min)

11. During cell growth, at least once per hour, remove 10mL samples to manually measure optical density and freeze for later analysis.

12. After cell culture is finished, kill all of the cells with bleach and dispose. Wash and rinse all of the components. (2 hours)

All in all, in a typical laboratory, a stirred tank experiment is a two day ordeal. One day to set up and one day to conduct the experiment and clean up. To perform eight stirred tank reactor experiments with 8 separate bioreactors would require approximately 75 man-hours of work. If a chain of experiments were being performed with a single reactor, a key limitation is the autoclaving and cool down of the stirred tank, and the fermentation itself, which would lead to 9 days of work for eight experiments. .

In contrast, while the innoculum procedure is the same, using the PIBA requires only approximately 2-3 hours to setup, after which all data is acquired automatically for eight bioreactions. After the experiment is concluded, final sample collection for analysis, and OD calibration measurements requires another 2-3 hours. Approximately five hours of work, 6 times less than for a single stirred tank bioreactor experiment, and one and a half days of preparation and fermentation yields eight experimental results, an order of magnitude faster than using conventional methods, with the advantage of automated data collection.

7.2 PIBA validation

One of the key objectives for the PIBA was to achieve multiple high cell density cell cultures, defined by an optical density higher than 20, in parallel, without oxygen limitation. The previous chapters desribed the key capabilities required to meet this objective, pH control, high oxygen transfer rate, and design for scalability. In the following sections we validate our design decisions by demonstrating a series of bioreactions conducted using the PIBA platform.

7.2.1 Strain and medium composition

Escherichia coli FB21591 (thiC::Tn5 -pKD46, KanR), obtained from the *E. coli* Genome Project at the University of Wisconsin (http://www.genome.wisc.edu), was used in all experiments. Cultures were grown in either a modified Luria-Bertani (LB) medium or defined medium at 37°C.

The modified Luria-Bertani (LB) rich medium[93] consisted of (per liter): 10g tryptone, 15g yeast extract, 5g NaCl, 5g K_2HPO_4, 1.2g $MgSO_4$, which were autoclaved, and then 1mL trace metal solution, 100mg Kanamycin, and 40g glucose, were added as filter sterilized solutions. The trace metal solution contained (per liter) 4mg $(NH_4)_6Mo_7O_{24}{\cdot}4H_2O$, 71mg H_3BO_3, 2.5mg $CuSO_4{\cdot}5H_2O$, 16mg $MnCl_2{\cdot}4H_2O$, and 3mg $ZnSO_4{\cdot}7H_2O$.

The defined medium[94] consisted of (per liter): 13.5 g KH_2PO_4, 4.0 g $(NH_4)_2HPO_4$, 1.4 g $MgSO_4{\cdot}H_2O$, and 1.7 g citric acid, which were autoclaved, and then 100mg Kanamycin, 40g glucose and 10mL trace metal solution, were added as filter sterilized solutions. The trace metal solution was composed of (per liter 5M HCl): 10.0 g $FeSO_4{\cdot}7H_2O$, 2.0 g $CaCl_2$, 2.2 g $ZnSO_4{\cdot}7H_2O$, 0.5 g $MnSO_4{\cdot}4H_2O$, 1.0 g $CuSO_4{\cdot}5H_2O$, 0.1 g $(NH_4)_6Mo_7O_{24}{\cdot}4H_2O$, and 0.02 g $Na_2B_4O_7{\cdot}10H_2O$.

For inoculum preparation the strain was first adapted to the final fermentation medium as follows: 5 mL of modified LB was inoculated with a single colony, from an overnight LB-Kanamycin agar plate, and incubated at 37°C on a roller drum at 60 rpm. At an optical density (OD_{600nm}) of 1±0.1, 1.6 mL was used to inoculate 30 mL of the final medium in a

500 mL baffled shake flask and incubated at 37°C on a horizontal rotary shaker at 150 - 200 rpm until the optical density reached approximately 1.0. At this point the culture was diluted in fresh final medium to reach an OD_{600nm} of about 0.05 and used to inoculate microbioreactors.

7.3 Batch fermentation on complex medium

A series of experiments were carried out to demonstrate: the importance of pH control for achieving high cell densities, the repeatability of the data, and comparability to results from stirred tank bioreactors.

7.3.1 Growth results

Results from *Escherichia coli* fermentations using four different growth conditions with three to six replicates for each growth condition are shown in Fig. 7-1. Measurements of the cell density, pH, and dissolved oxygen, taken every 40-80 seconds, where the lines represent the average of all replicates for a given condition, with the exception of the controlled dissolved oxygen curve (green), where the line represents the minimum dissolved oxygen among the replicates, which was the variable used for control. The error bars indicate the maximum and minimum boundaries of the replicates for a given growth condition, and indicate the precision between replicates. The overlap of the growth curves for culture times < 3 hours, where growth conditions were essentially equivalent, demonstrate reproducibility across cell cultures conducted on different days with independent innocula.

The series of experiments indicated the importance of pH control in achieving high cell densities. The longer the pH was maintained at 7, the higher the final cell density. The high frequency of pH control actions ($>30 hr^{-1}$), which was enabled by the integrated microfluidic injectors, was important considering the large amount of acetate produced by this strain under excess glucose conditions which results in a sharp decrease in pH due to acetate secretion of up to 1.5 units/hr, near the end of the fermentation. At this rate of acid production, the pH would change by 0.1 units in only 4 minutes.

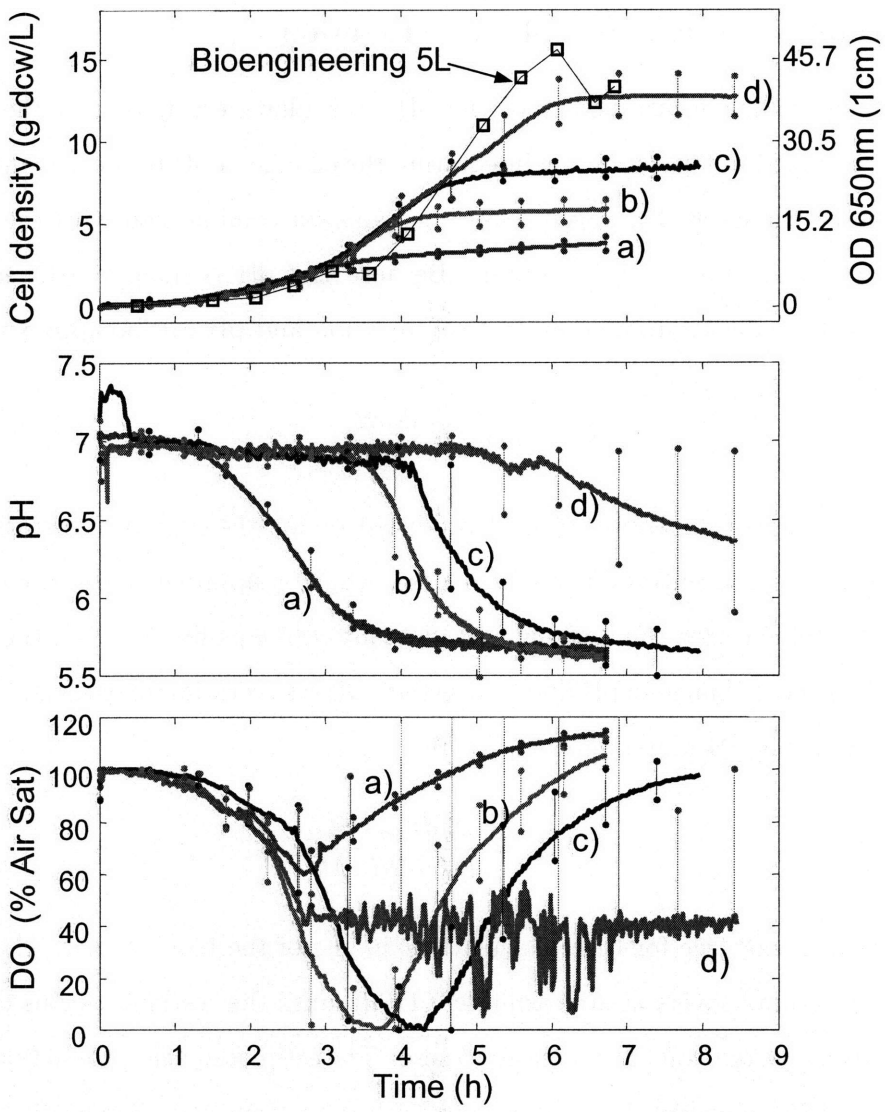

Figure 7-1: Data from four different experimental conditions: no pH control (a), 3 replicates); pH control with 1.6M NH_4OH (b), 5 replicates), pH control with 2.4M NH_4OH (c), 4 replicates), pH control with two 2.4M NH_4OH reservoirs and dissolved oxygen control set for $> 50\%$ oxygen (d), 7 replicates). Solid lines indicate the mean of all replicates and the error bars indicate the minimum and maximum data points of all replicates. The controlled dissolved oxygen case shows a large variance due to imperfect matching of the k_La, which led to excess oxygen supply to some growth wells. Black square markers are cell density data from the 4L stirred tank cell culture.

7.3.2 Acetate and injected volume estimation

High frequency, online measurement of the pH also allows estimation of the total acid production, assumed to be acetate, by integrating the change in pH between control actions, or summing the change in pH due to base injections, in combination with the previously measured titration curve of the medium. Because the pH is maintained near 7.0, the relationship between acid production, or base injection and pH can be approximated by a linear relationship by given by,

$$[acid] = \frac{\Delta pH}{\frac{dpH}{dM}} \tag{7.1}$$

where $[acid]$ is the concentration of acid produced or for the case of integrating the pH controller response, concentration of added base, which is approximately equal as long as the pH is maintained near the setpoint. Incidentally, the equality between the integrated change in pH and the change in pH due to injections allows an estimate of the actual injected volume based on the pH measurements, where

$$V_{inj} = \frac{\Delta pH_{inj}}{dpH/dM} \frac{V_{init}}{M} \tag{7.2}$$

Fig. 7-2 shows an example for these calculations in one of the bioreactions. The estimated fluid injection volume hovers at approximately 170nL until the reservoir begins to empty, at which point the injected volume decreases to zero. The estimated acid production compared to biomass is 0.75g/g, which is in agreement with data from a similar fermentation from the literature[93].

7.3.3 Steady state k_La

The steady state k_La_{ss}, could be determined from the dissolved oxygen and cell density measurements by using Eqn. 5.3. OUR_{max} was calculated from product of the specific oxygen uptake rate (20mmol/g-dcw/h[24]) and the cell density taken when the dissolved oxygen reached zero. The oxygen saturation concentration, C*, was assumed to be 0.21mmol/L, the value for water at 37°C, which is likely an overestimate due to the dissolved salts in the

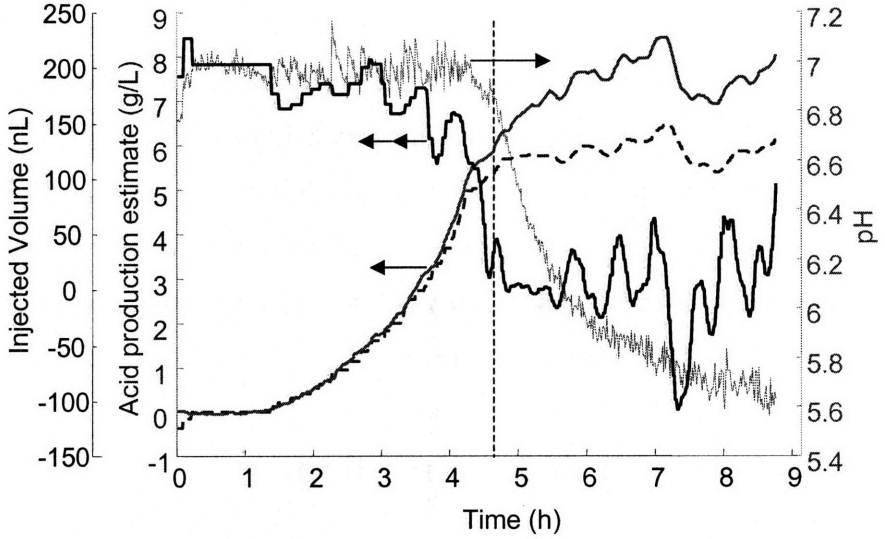

Figure 7-2: Estimate of acid production based on integration of dpH/dt (solid, first left axis), estimate of acid production from injected base (dashed), corresponding estimate of injected volume (solid, second left), pH during the fermentation (right axis). The acid production estimate is only valid for times during which the pH is maintained within 0.2 units of 7, beyond which the linear approximation to the medium titration curve fails. In this experiment, a single base reservoir was used and emptied after approximately 70 injections, or 10μL had been injected.

medium.

The average $k_L a_{ss}$ from Eqn. 5.3 for the 9 replicates where the dissolved oxygen was not controlled was $0.1s^{-1}$ with standard deviation of $0.02s^{-1}$, which was comparable to the expected $k_L a_{ss}$ of $0.13s^{-1}$. The maximum and minimum kLass were $0.14s^{-1}$ and $0.06s^{-1}$. We hypothesize that the variation in $k_L a_{ss}$ is to be due to a variation in the volume of innoculum, which had an impact on the membrane deflection, and therefore the mixing efficiency, of the mixer.

7.3.4 Comparision with 5.5L stirred tank bioreactor

Also shown in Fig. 7-1 is a growth curve from a 4L fermentation, using the same modified LB medium and strain, performed in a 5.5L stirred tank bioreactor (Bioengineering, Type L1523). The growth curve was obtained by manually taking samples every 30-60 minutes,

performing dilutions, and measuring the optical density. The data points were time shifted to account for the 1.5 hour longer lag phase in the stirred tank bioreactor and correspond well to the growth curves from the parallel integrated bioreactor array grown under the same conditions, with comparable final cell densities. This indicates that for experiments where cell density, pH, and dissolved oxygen are sufficient phenotypes, such as when optimizing medium composition for maximum yield, the parallel integrated bioreactor array can substitute for controlled stirred tank bioreactors.

7.4 Batch growth on defined medium

The results from batch growth on a complex medium confirmed the ability of the PIBA platform to support high cell density growth. While the growth curve from a 4L stirred tank fermentation using the same growth conditions as in the PIBA was comparable, we would like more evidence to confirm the applicability of results on the small scale to larger stirred tank reactors.

Rather than conducting multiple bench scale stirred tank experiments and comparing to PIBA results, we look to compare our growth results with previously developed and experimentally verified models for *E. coli*. A prerequisite for such comparisons are fermentations on defined media with known composition, as opposed to complex media such as the previously used Luria-Bertani based medium.

7.4.1 Growth results

Shown in Fig. 7-3 are four replicates for batch growth on defined medium. The growth curve, pH, and dissolved oxygen are shown along with the instantaneous doubling time. The ability to calculate the growth rate, or doubling time with high-resolution is a feature of the high frequency sampling of the optical density. A well defined lag phase of approximately three hours is clearly evident in all replicates, where growth slows for approximately an hour, after which exponential growth with doubling time between 1-2 hours proceeds for 9 hours until the 40g/L of glucose is consumed. This is evidenced by the sharp increase or spike

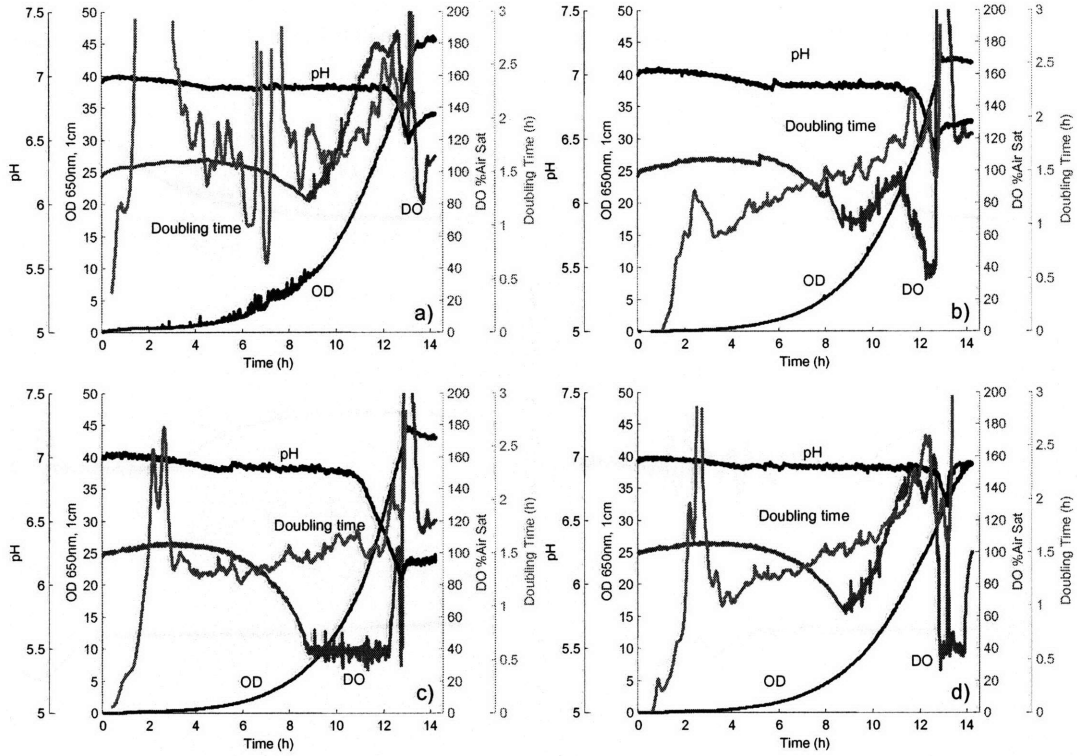

Figure 7-3: Four replicates of *E. coli* growth on defined medium with 40 g/L glucose. Shown are the growth curves, dissolved oxygen, pH, and doubling time. Note the well defined three hour lag phase after which the doubling time settles between 1-2 hours. Reactor c) was the minimum DO initially, followed by reactor b) and then reactor d). Growth stopped when the glucose was consumed. Acetate consumption after glucose is consumed is indicated by the sharp increase in pH.

in dissolved oxygen, after which acetate is rapidly consumed, leading to a sharp increase in the pH. The maximum of the average OD was 42.2, corresponding to a cell density of 13.8g/L.

7.4.2 Comparison with growth on LB

Fig. 7-4 shows the growth results from the modified LB medium and the defined medium, which highlights why growth on defined medium is prefered when studying microorganisms. There are numerous kinks in the growth curves in the LB fermentations, that indicate the bacteria are responding to the consumption of non-essential nutrients, which then need to

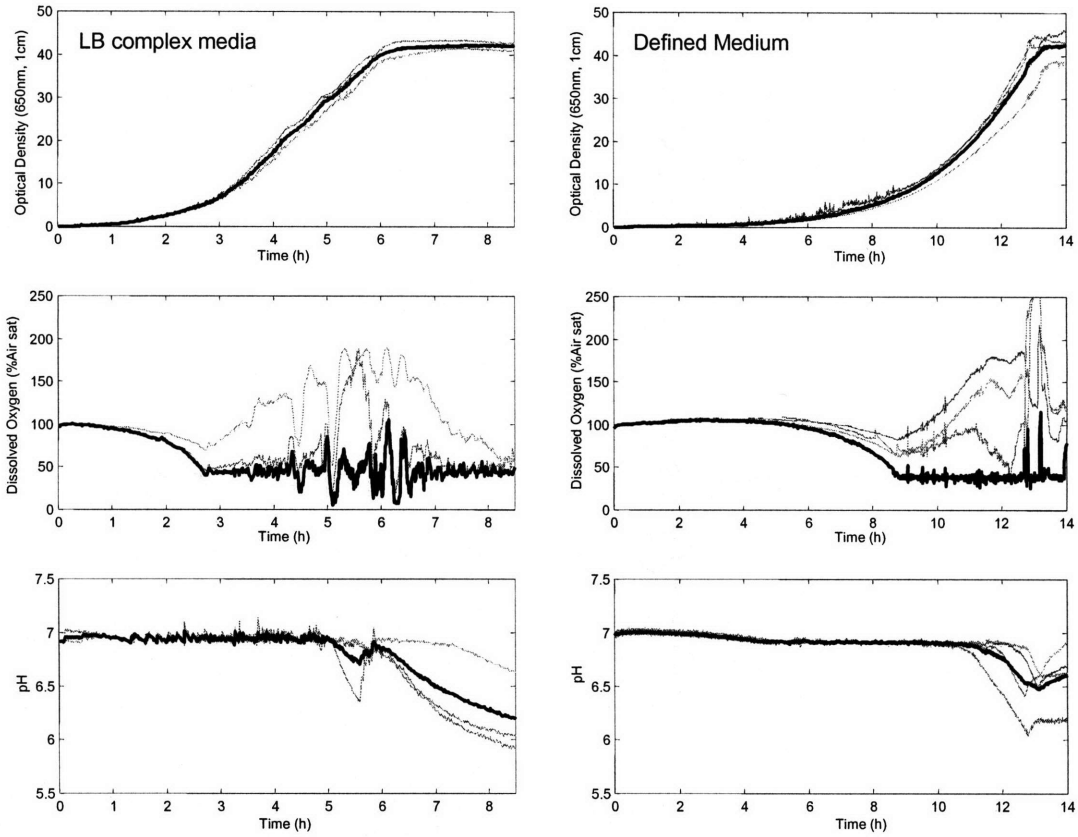

Figure 7-4: Comparison of *E. coli* growth experiments in Luria-Bertani complex media with 40g/L glucose and Defined medium with 40g/L glucose.

be synthesized.

7.4.3 Comparison with model

E. coli are known to produce acetate even without oxygen limitation in the presense of excess glucose. This is termed overflow metabolism[25] and is thought to occur because of saturation of oxidative metabolism of glucose within the cell. Excess glucose is then processed by an alternative pathway which results in the production of acetate.

A phenomelogical dynamic model was developed by Enfors [25], showed good agreement with experimental data on batch and fed-batch growth of *E. coli* in a 15L stirred tank bioreactor.

The governing equations, modified to incorporate the PIBA DO controller, are:

$$\frac{dS}{dt} = \frac{F(t)}{V}(S_{feed}(t) - S) - qSX \tag{7.3}$$

$$\frac{dA}{dt} = (qA_p - qA_c)X - \frac{F(t)}{V}A \tag{7.4}$$

$$\frac{dX}{dt} = (\mu - \frac{F(t)}{V})X \tag{7.5}$$

$$\frac{dV}{dt} = F(t) - F_{sample} \tag{7.6}$$

$$\frac{dO}{dt} = k_L a(R - O) - \frac{qOX}{32,000} \tag{7.7}$$

$$\frac{dR}{dt} = -\frac{F_R}{V_R} + \frac{F_R}{V_R}(O_{NC}D + C_{NO}(1 - D)) \tag{7.8}$$

with parameters defined in Table 7.1

S	Glucose concentration	40 (t=0)	g/L
$F(t)$	Volumetric flow rate into reactor	0	L/h
F_{sample}	Volumetric sampling rate	0	L/h
V	Volume of cell culture	0.1	mL
S_{feed}	Glucose concentration in feed	0	g/L
$k_L a$	Oxygen transfer coefficient	360	1/h
F_R	Flow rate into mixer driver reservoir	3.9	L/h
V_R	Volume of mixer driver reservoir	0.75	mL
qS	Specific glucose consumption rate		g/L-g-dcw
A	Acetate concentration		g/L
qA_p	Specific acetate production rate		g/L-g-dcw
qA_c	Specific acetate consumption rate		g/L-g-dcw
X	Biomass concentration		g-dcw/L
μ	Growth rate		1/h
O	Oxygen concentration		mmmol/L
R	Reservoir oxygen concentration		mmol/L
qO	Specific oxygen uptake rate		g/L
O_{NC}	Oxygen concentration at normally closed port		% Air sat
O_{NO}	Oxygen concentration at normally open port		% Air sat
D	Duty cycle of gas blending switch		

Table 7.1: Parameters in *E.coli* glucose overflow metabolism model

At each time step, qS, qA_p, qA_c, μ, qO, are calculated according to[25], where detailed parameters are given in App. B.

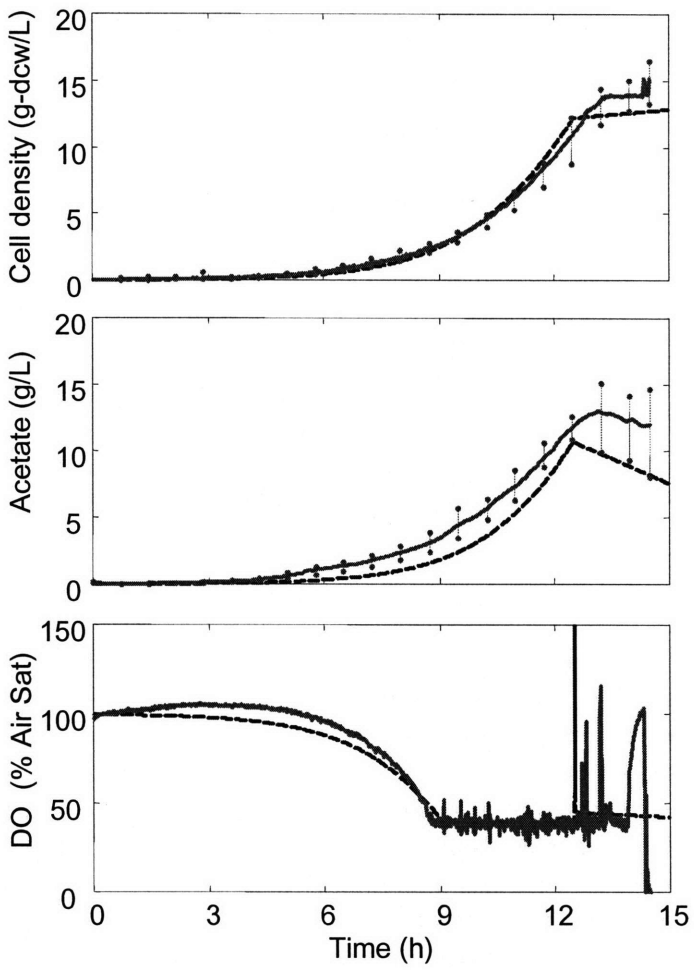

Figure 7-5: Comparison between dynamic model of *E. coli* glucose overflow metabolism (dashed) and experimental data (solid) of *E. coli* batch culture on defined medium with 40g/L glucose.

Fig. 7-5 shows growth results from the batch culture on defined medium compared to the output of the model with parameters given in Table B.1

The model was able to fit the data through five parameters which differed from the published model. The parameters are highlighted in App. B, and except for the Monod inhibition coefficients used to fit the relatively high acetate production, were within the range of parameters from the literature.

7.5 Fed batch growth using PIBA

In this section, we wish to explore the possibility of implementing fed batch fermentation using the PIBA. The objective of fed-batch growth is usually to obtain a high cell density by continuously feeding nutrients as they are consumed. In addition, the growth rate can be controlled through feeding a limiting substrate, typically glucose. By slowing the growth below a critical threshold, acetate production through overflow metabolism can be avoided [19]. In addition, a high acetate concentration has been observed to inhibit growth and negatively impact recombinant protein production. Even if overflow metabolism is not avoided, fed-batch growth can keep the acetate concentration low, by forcing the bacteria to consume it as a carbon source.

Due to the discrete nature of the fluid injectors, maintaining a low glucose concentration and controlling the growth rate below a critical threshold will not be possible. This is because when a glucose injection is initiated, the bacteria will rapidly consume it, produce acetate through overflow metabolism, consume the acetate, and then starve until the next glucose injection. Therefore, while a fed-batch strategy with the coarse intermittent feeding may be able to keep the acetate concentration low and maintain the long time scale growth rate less than the critical value, the instantaneous growth rate will fluctuate with feeding. For improved performance, high-resolution fluid injectors will be necessary to approximate a continuous flow as closely as possible, which means the time between injections should be less than the time for the cells to consume all of the glucose in order to minimize the overall fluctuation in the glucose concentration.

The time between injections will be a function of target final cell density and the capacity and resolution of the glucose injector. For example, assuming a $Y_{XS} = 0.5$ g/g biomass yield on glucose, we can convert glucose injections directly into biomass. To achieve a final cell density of 50g/L in a 100μL growth well using a 20μL glucose reservoir, assuming the batch phase starts with 5g/L glucose, we will need to provide 11.5mg of glucose which translates into a 575g/L glucose concentration in the reservoir. For a 250nL injection, each injection will introduce 1.4×10^{-4}g glucose which will be converted into 7.2×10^{-5}g biomass.

Ignoring the increase in volume for simplicity, each 250nL injection will translate into ΔX = 0.72g/L of biomass. In order to approximate a target growth rate, μ_o, we need to satisfy

$$X_{n+1} = X_n e^{\mu_o \Delta t_{n+1}} = X_n + \Delta X \tag{7.9}$$

where X_n is the cell density before the n$^{\text{th}}$ injection, and Δt_n is the time until the next injection . Solving for Δt_{n+1} we have

$$\Delta t_{n+1} = \frac{1}{\mu_o} \ln\left(1 + \frac{\Delta X}{X_n}\right) \tag{7.10}$$

To implement this strategy, we would require accurate measurements of the biomass. To get a sense for the time between injections, for μ_o=0.3hr^{-1}, near the end of the fermentation when $X \approx$ 50g/L, we have Δt = 170seconds, which is well within the minimum sampling time to operate the system ($\approx$ 60sec) and much less than the 3.3 hour time constant for growth.

7.5.1 Fed-batch simulation

Using the parameters extracted from the fit to the batch fermentation, and utilizing the assumed values for the glucose injector in Sec. 7.5, we were able to simulate a fed-batch fermentation using the PIBA, in order to indicate what we might expect in a real implementation. An example using exponential feeding with a target growth rate of $\mu_o = 0.075\text{hr}^{-1}$ is shown in Fig. 7-6. As expected, spikes in the glucose concentration at each injection led to a transient response in the dissolved oxygen, and the production of acetate. However, acetate only accumulated if the net acetate production after a glucose injection was non-zero. With an exponential feeding profile, this did not hold true unless the target growth rate was very low, consistent with the concept of a maximum growth rate before acetate production/accumulation becomes important.

The relatively poor performance of the dissolved oxygen controller response to feeding indicates a combined control strategy will be required to implement fed-batch fermentations,

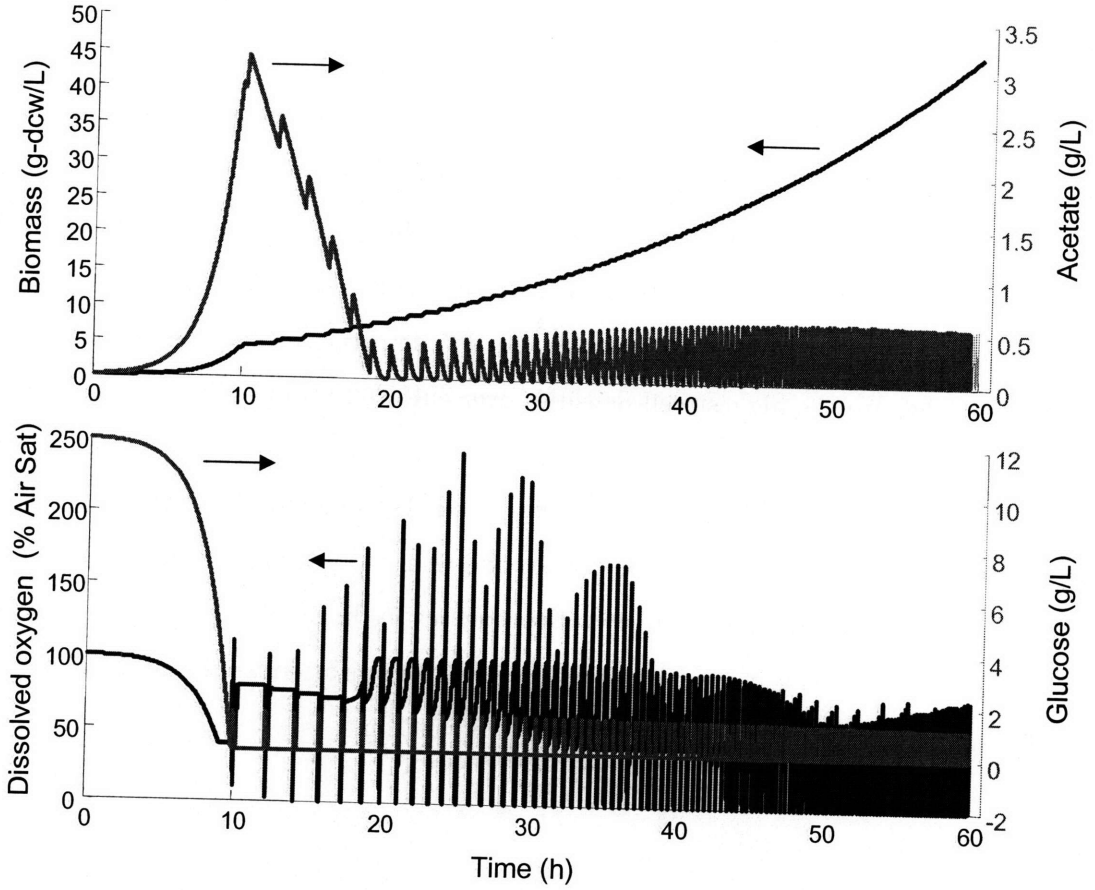

Figure 7-6: Simulation of Fed-batch fermentation of *E. coli* using exponential feeding to target a 0.075hr^{-1} growth rate. Acetate does not accumulate under these conditions.

preferably with independent dissolved oxygen control in each reactor.

When comparing the performance against other growth conditions, we found that with the model parameters that best fit the batch fermentation, did not adequately account for growth inhibition observed by others due to acetate accumulation. In fact, the best performance can be obtained with batch growth starting with a very high glucose concentration. This highlights the importance of experimental study in bioprocess development and the inadequate predictive power of the model, although it did prove useful to anticipate some technical challenges in implementing high cell density fed-batch fermentations in the PIBA platform.

7.6 Conclusions and future work

In this chapter, we presented a series of *E. coli* fermentations utilizing the PIBA platform. Five sets of eight simultaneous fermentations under various conditions were conducted, demonstrating the essential nature of pH control for achieving high cell density fermentations. In modified LB media with 40g/L of glucose, the cell density reached 12.8g-dcw/L and in defined media with 40g/L of glucose, the cell density reached 13.8g-dcw/L, which to our knowledge are the highest cell densities ever cultured in microfabricated bioreactor arrays.

Simulations of fed-batch fermentations using the PIBA indicate there will be challenges in maintaining the dissolved oxygen control. In addition, the intermittent nature of the glucose injections may not be representative of continuous feeding utilized on the macroscopic scale. Experimental verification of an actual process optimization would be of tremendous value for validating the system for its intended application.

Chapter 8

Conclusions and future work

Chap. 7 concluded with a demonstration of the parallel integrated bioreactor array, showing aerobic growth of *E. coli* in eight simultaneously operated reactors up to a cell density as high as 13.8g-dcw/L (OD≈42), more than four times higher than previously demonstrated microfabricated bioreactors. This was made possible by innovations in microfluidic device design, fabrication, and integration. However, not all of our original objectives were achieved leaving numerous opportunities for future development.

8.1 Contributions

This work has demonstrated the feasibility of implementing high-performance, disposable bioreactor arrays using microfabrication technologies. This approach offers a new avenue towards developing a scalable high-performance bioreactor array system, which are currently being pursued via mechanical and robotic multiplexing of miniature stirred tank bioreactors. The latter approach depends on advances in robotics and precision machining for cost reduction and performance improvement, while with microfabricated arrays, the scaling problem is primarily an optical and electronic challenge as will be discussed in Sec. 8.2.4.

The new level of performance in microfabricated bioreactor arrays was enabled by the development of a novel peristaltic oxygenating mixer which provided an oxygen transfer

rate corresponding to a k_La of up to $0.1s^{-1}$. Its combination with a novel dissolved oxygen control method allowed DO control in microbioreactors for the first time. Lateral mixing in approximately 10 seconds was also vital for implementing pH control using acid/base injections from a microfluidic injector, integrated with the peristaltic oxygenating mixer. The injector was capable of delivering 100-300nL injections and combined with an adaptive algorithm, was suitable for pH control of the *E. coli* fermentations.

The integration of the peristaltic oxygenating mixer and fluid injectors with the bioreactor growth well was enabled by a novel fabrication process which combined the best features of conventional CNC machining with elastomer micromolding. This process was capable of integrating devices with multiple depths (100μm - 2.5mm) and multiple profiles (hemispherical, square, rounded) in a single mold. In addition, the use of molded features external to the device greatly simplified the macroscopic interfaces to the devices.

8.2 Future work - near term

While this work was an advance in the state of the art, it fell short of the original objectives and is not yet suitable for deployment in microbiology laboratories. While a number of system improvements are developmental in nature, there are related areas for research. Two key areas to improve are device usability and migration to a process suitable for mass production.

8.2.1 Usability and mass fabrication

Usablility

Although the PIBA requires less setup effort than eight bench scale stirred tanks, innoculation of the microbioreactors and filling the acid/base reservoirs is still quite tedious. Currently, a 26 3/8 G needle is required to vent the chamber while the innoculum is injected into the well using a syringe. This currently requires great care to ensure no air bubbles are left inside the reactor because the innoculation ports were not designed with

this in mind. Future devices will need to incorporate a more streamlined shape such that the air/liquid interface tranvels smoothly from the input to the output port.

In addition, because controlling the injected volume with syringes is not very precise ($\pm 10\mu$L), and not standard practice for microbiologists, development of injection ports compatible with standard laboratory pipettes will be a priority. Desirable characteristics of these ports will be a normally closed state that is easy to force open with a 200μL pipette tip, and easy to open with a simple mechanical action to allow venting. Such injection ports would also be helpful for final sample recovery or even the removal of small samples during fermentation.

Mass production

The fabrication process described in Chap. 3 was close to ideal for rapid prototyping of molded devices, but the fabrication throughput of 3 bioreactor arrays in approximately 3.5 hours is insufficient to supply a microbiology laboratory. An important improvement will be to migrate the fabrication to an injection molded process for the two or more device layers. The key processing question to research is the bonding of elastomer membrane layers with with the injection molded thermoplastic layers in a scalable way that does not impact the function of the membrane pinch valves. In addition, direct deposition of the sensors into the growth wells will simplify production.

The fabrication out of rigid materials will also improve the performance of the optical density sensing since the optical path length will not be affected by mechanical compression. For experiments where analysis of the medium would not be required, this would further simplify the use of the system and eliminate the endpoint calibration of the optical density.

8.2.2 Oxygenation and mixing

Although initial results were promising, the oxygen transfer capacity was not up to expectations and there remains some open questions on the performance of the mixer.

Oxygen transfer capacity

The maximum measured k_La was $0.1s^{-1}$, which was below our original goal of $0.28s^{-1}$ to support 50g-dcw/L of rapidly growing *E. coli*. This was found to be limited by the mixing efficiency in the vertical direction, or transverse to the plane of the growth well. Improvement could be achieved by more agressive mixing with higher actuation pressure and frequency, with the caveat of ensuring the mechanical forces do not have a detrimental effect on the cells. Approaching perfect mixing will allow the k_La to approach $0.2s^{-1}$, assuming no further changes to the membrane thickness are made. Further improvements could be realized with membrane materials with higher oxygen permeability. Material selection was not optimized for this parameter and there is evidence that, as a silica filled PDMS, Sylgard 184 is not optimal in this regard. Given measurements of oxygen solubilities in pure PDMS improvements in the k_La by a factor of three are available, assuming improved mixing can be achieved. An additional avenue for improving the oxygen transport capacity would be to increase the surface area to volume ratio, by perhaps allowing oxygenation through the underside of the device. This could be accomplished by incorporating an additional membrane at the bottom of the device, mechanically supported by microchannels. This would approximately double the steady state k_La at the cost of fabrication complexity.

Mixing and fluid characterization

As discussed in Sec. 8.2.2, improved mixing will be critical to improve the oxygen transfer coefficient. However, quantifying the resultant mechanical forces will be necessary to ensure they do not harm the cells and that the mechanical environment would be similar to that encountered in a stirred tank bioreactor. Critical to this investigation will be the application of, or development of a method to image the three dimensional velocity profile of the fluid inside the microbioreactor. Preliminary results imaging fluorescent latex spheres indicate a complex lateral flow pattern within the device, but quantitative information on the fluid velocity has not yet been extracted. In addition, information on the vertical flow, which is most important for mixing has not been measured. With further insights from quantitative

fluid measurements, improvements in the membrane pattern, or actuation sequence may come to light. Quantification of the mechanical forces experienced by cells inside the mixer will also be critical in extending this bioreactor concept to grow mammalian cells, which are generally much larger and sensitive to shear forces than microbial cells. They do, however have lower oxygen demand which would allow less vigorous mixing. Nonetheless, quantification and comparison of shear forces in the microbioreactors and conventional reactors will be important for this application.

8.2.3 Fluid control and DO control

With the successful demonstration of the overall bioreactor array, where imprecision in the fabrication and non-ideal device functionality was overcome by algorithmic corrections, addressing these issues will be important to extract higher quality data from the system.

pH control

For the pH control, the number one issue is to extend the pH control capacity, by either enlarging the size of the fluid reservoir, or by by reducing the injected volume while increasing the molarity of the acid/base. Enlarging the fluid reservoir is straightforward, but comes at the cost of increased device area. Reducing the injection volume and increasing the molarity of the acid/base is a fabrication issue. The injected volume can be reduced by reducing the size of the injector channel and the length of the injector valve, and reducing the deadspace into which the valve membranes can bulge. Increasing the molarity of the acid/base is related to the material compatibility, which will play a role in the selection of materials for the next generation mass producible process.

The size of the channels and valves for the current generation devices was a compromise between injection volume and yield. Smaller channels were found to be sealed shut due to overcompresion of the device layers during bonding. This was exacerbated by the flat aspect ratio caused by end-mill runout. Runout can be minimized by taking greater care in mounting the end-mill into the milling machine headstock or by using higher precision

tools. The deadspace above the valves was made much larger than necessary in order to simplify alignment with the pins defining the actuation ports. The consequence of this was the variation in injected volume due to the bulging of the injector valves. This could be minimized with improved mold design in an injection molded part which constrains the bulging of the valve membrane.

Valve sticking was frequently observed when the molarity of the base was above 2.5. This was presumably due to the concentrated base reacting with the PDMS surface [81],[82], increasing the suceptibility of the membrane and channel walls to bond together through diffusion of polymer chains[83] with dimethyl-vinyl ends intermingling with those with dimethyl hydrogen ends, which will bond in the presense of platinum catalyst which remains in the polymer[84]. More careful experimentation would be required to confirm this hypothesis, however and to clarify the role of excess acid or base, although such valve sticking has been observed in channels filled with glucose solution, when the valves were sealed shut for more than 8 hours.

Fed-batch and continuous mode

For the pH control, one problem with the injector was the inconsistency of the injected volume due to bulging of the valve membrane in the open state. While this was easily overcome by using an adaptive pH control algorithm, for fed-batch and continuous mode operation, where direct feedback (through the pH) that allowed inferring the injected volume would not be available. In this case, *a priori* knowledge of the injected volume is critical for controlled experiments. As mentioned in Sec. 8.2.3 this can largely be accomplished by minimizing the dead-volume of the membrane pinch valve using rigid materials and more precise fabrication of the channel dimensions.

DO control

The performance of the dissolved oxygen controller with the improved (smaller) gas mixing reservoir performed admirably. The key limitation is an inability to individually control

the dissolved oxygen level. As described in Sec. 5.4, this can be accomplished with a modified design in the peristaltic oxygenating mixer by adding an additional control layer and isolating the gas feed into each bioreactor. This will have the additional advantage of allowing measurement of the inlet/outlet oxygen concentration, which will allow an independent estimate of the oxygen uptake rate.

8.2.4 Scaling

In Sec. 6.4 the overall architechture of the PIBA platform and the prospects for scaling the system beyond eight bioreactors were discussed. For $M \times R$ total reactors, the scaling for pneumatic switches to control four fluid injectors per reactor is 4M + 2R. For the mixing and dissolved oxygen, assuming the design for individual dissolved oxygen control at one acutation frequency, we would require $MR + 10$ switches. Overall, $MR + 4M + 2R + 10$ pneumatic switches would be required. For M = 6 and R = 12 and 72 reactors, 130 switches and the requisite driving electronics would be required. The driving electronics include 48 independent static digital lines, a simple shift register circuit to drive the peristalsis actuation, and an array of 72 variable duty cycle oscillators, which compose the most expensive part of the electronics. For comparison with robotic actuation methods, the relevant number is the 48 required pneumatic switches of the PIBA versus the pipetting robot to multiplex fluid addition. To compare DO control options the relevant comparison would be, on a reactor by reactor basis, one motor and motor controller and potentially one mass flow controller for conventional technology, with one pnumatic switch and one variable duty cycle oscillator for the PIBA.

Scaling in the optical sensors is directly proportional to the number of reactors. For each reactor, we would require a pH and DO sensor along with an optical density measurement. The key challenge will be in routing and collection of all of the optical signals to allow sharing the photoreceivers among more than one sensor, or in developing an inexpensive means of directly addressing all of the optical sensors. The ideal combination would be a technology that would allow batch fabrication of large core multimode components with

switching capability to allow optical multiplexing.

8.3 Future work - long term

Our original objective was to develop a tool for high-throughput and high-performance microbial growth experimentation. The key technologies to achieve scalable high-performance microbioreactor arrays have been developed, and with the additional development described in Sec. 8.2, such devices will be deployable to microbiologists. Extensions of this technology that motivate future areas of research are considered in the remaining sections.

8.3.1 Applications

Once user interface and manufacturing issues are resolved, they key question will be biological validation of the results from the PIBA in actual bioprocess development and scale up scenarios. Such a detailed study will surely reveal discrepancies between the 100μL PIBA reactors and 2-10L stirred tanks. That work could also explore the flexibility of the PIBA in simulating transients and concentration gradients within industrial scale reactors to determine the value of the PIBA as a scale-down system.

For those who study metabolic engineering or systems biology, extending the PIBA to support continuous mode bioreactions would prove valuable for studying multiple steady states.

8.3.2 Upstream

As described in Sec. 7.1, while the PIBA impacts the effort to setup and run the bioreactions, there is still considerable effort to prepare the inoculum using agar plates, roller tubes, and shake flasks. For experiments involving strain screening or medium optimization, this effort could be a significant burden. One of the main reasons for the inoculum generation procedure, starting from a colony, to a tube, and then a flask is to have process reproducibility since there is a large variance in the initial number of cells from a single

colony introduced into a liquid culture. The initial liquid culture growth in the roller tube using rich medium is to ensure rapid growth of a healthy population of cells that are later adapted to the growth medium in a shake flask to generate a sufficient volume of inoculum. An ideal process incorporating the microbioreactor arrays would allow direct deposition of colonies into a small, simple pre-culture chamber with no mixing and only an optical density measurement. After a fixed optical density is reached, the contents would be injected into a second pre-culture chamber with the final growth medium. Growth to a fixed optical density would the preciptiate injection into the fully actuated PIBA bioreactor. Such a system would require two addtional optical density measurements per bioreactor and two individually addressible valves to control inoculum injection.

Key enabling technologies for this would again be scalable optical density measurements and potentially a fabrication process capable of three-dimensionally routed fluidic channels and valves.

8.3.3 Downstream

At the end of the day, the product of any experiment is the data. The current system is capable of providing the optical density, total acid production, and the approximate oxygen demand, which is useful for some experiments where biomass is the key indicator. However for more complicated experiments where concentration of metabolites is desired, or RNA expression the current level of performance is inadequate.

A near term solution would be to provide sample collection capability for further analysis. In this case, the number of samples would be determined by the volume required for external analysis tools.

An ultimate objective would be to explore online chemical analysis capable of either *in situ* analysis using an optical spectroscopy, or an integrated sample processing and fluidic analysis system such as flow injection analysis.

Appendix A

Device Fabrication

The design objectives for the PIBA required developing a novel fabrication process that could support multiple depths and cross-sectional profiles. Specifically, we require 500μm deep growth wells, along with 100μm deep channels, with round cross section for good sealing of the membrane pinch valves. In addition, we required deep hemispherical fluid reservoirs to minimize the dead volume, and deep peristaltic mixing tubes to allow large fluid displacement. A final requirement was the maintenance of smooth surfaces for bonding multiple layers of PDMS together.

All of these requirement were satisfied by the polycarbonate mold transfer process described in this chapter.

A.1 Master Mold Fabrication

The process begins with the fabrication of a master polycarbonate mold, which is a positive replica of the final PDMS devices to be made, using computer numeric controlled (CNC) machining with a variety of ball and square end mills.

Optically clear surfaces are obtained by vapor polishing the machined parts in a methylene chloride vapor. This is critical, not only for optical access to the fluorescence based sensors, but also for good mold release between the PDMS device and surface treated PDMS

mold.

A.2 PDMS Device Mold

The PDMS device mold is cast from the polycarbonate master mold. This negative mold is then surface treated with (Tridecafluoro-1,1,2,2-Tetrahydrooctyl)-1 Trichlorosilane (United Chemical Technologies T2492) vapor by placing a few drops of the silane compound with the PDMS molds in an aluminum chamber. After chamber is evacuated to 25mm/Hg, the temperature is raised to 70°C for 4 or more hours.

A.3 Polycarbonate Device Mold

Each PDMS mold also has a corresponding polycarbonate mold, which defines the surface features of the final devices, including gaskets around all actuation and injection ports for efficient face sealing to the interface plates and recesses to allow the fiber bundles to be placed close to the optical sensors. In addition, there are holes to guide the placement of teflon coated steel pins, which define the pneumatic actuation ports, obviating the need for post cure punching of access holes. Each polycarbonate mold was CNC machined and then vapor polished. Alignment pins guarantee good alignment with the PDMS device molds.

A.4 Device Fabrication Procedure

Device fabrication typically requires four hours from start to finish to fabricate three sets of devices. This was limited by the number of polycarbonate device molds that had been fabricated.

1. Turn on the oven, making sure the dial is set such that the average internal temperature will be 65°C

2. Weigh approximately 65g of Dow Corning Sylgard 184 PDMS polymer into a plastic

cup. Add the curing agent in a 1:10 ratio and mix thoroughly with a plastic knife (10 minutes).

3. Degass the PDMS in a vacuum chamber at approximately 25mm/Hg vacuum, being careful that the PDMS does not foam out of the plastic cup. (40minutes)

   (a) While waiting for the PDMS to degass, prepare the top Polycarbonate device mold by clearing the guide holes for the teflon coated pins with a 20G needle. also, remove any residual PDMS from the teflon coated pins.

4. Pour PDMS into the top, peristaltic mixing tube molds and place the molds along with the remaining PDMS into the vacuum chamber for further degassing. (15 minutes)

   (a) Mark the bottom of the growth well molds with a marker to indicate the position of the oxygen sensors.

   (b) Place the oxygen sensors face down in the growth well molds.

5. Remove the peristalitc mixing tube molds from the vacuum chamber and pour PDMS into the growth well molds. Place the growth well molds and the PDMS back into the vacuum chamber. (2 minutes)

6. Break all of the surface bubbles on the peristaltic mixing tube molds and position the top polycarbonate device mold over each PDMS device mold, being careful not to trap any bubbles. (5 minutes)

7. Insert the teflon coated steel pins into the guide holes and gently tap them down to ensure they are touching the nodes in the PDMS device mold, being careful not to press too hard, which will deform the PDMS nodes. (15 minutes)

8. Place the small steel weights onto each mold, in between the teflon coated steel pins to press the polycarbonate device mold onto the PDMS device mold and place in the middle shelf of a 65°C oven for one hour. (1 minute)

9. Remove the growth well molds from the vacuum chamber and break the surface bubbles. (2 minutes)

10. Using a pair of tweezers, reposition the oxygen sensors, which will have drifted as the PDMS was degassed. Press reasonably firmly to squeeze out as much PDMS from under the oxygen sensor as possible. (5 minutes)

11. Place the polycarbonate device mold on top of the PDMS device mold, again taking care not to trap any bubbles, and weigh the assembly down with the raised steel weights. (5 minutes)

12. Place the growth well molds into the top shelf of the oven for 50 minutes. (1 minute)

13. Spin coat six membranes on (Tridecafluoro-1,1,2,2-Tetrahydrooctyl)-1 Trichlorosilane treated four inch silicon wafers. Monitor the membrane thickness with the coherence interferometer. Drive the reference arm at 40Hz with a 200mV amplitude triangular wave. A 170μs time separation between the peaks will result in an approximately 65μm thick membrane. (20 minutes)

14. Place three of the wafers, in their petri dishes, into the oven on top of the peristaltic mixing tube molds. Shuffle the stack of wafers every 10 minutes. After the first shuffle, place the second set of three wafers into the oven on top of the growth well molds and again shuffle every 10 minutes. The shuffling ensures more uniform curing. After each shuffle, test the degree of cure of the membranes, which should be firm but extrememly sticky.

15. Remove all of the molds from the oven (after 1 hour has elapsed from the placement of the peristaltic mixing tube molds) and check the membrane cure state. If the cure is insufficient, place the membranes back in the oven for 5 minute intervals. Note: it is better to overcure the top mold since its bond to the membrane will be very good due to the under cure of the membrane. Curing for less than 1 hour will lead to problems demolding that will result in mixing tube fusions!. The bottom mold

can be slightly undercured to ensure a better bond, but again, the trade off is in the demolding process and structural integrity of the features.

16. Pull the teflon coated steel pins out of the peristaltic mixing tube mold. (5 minutes)

17. Peel the peristaltic mixing tube PDMS mold off of the polycarbonate mold. (5 minutes)

18. De-mold the peristaltic mixing tube device layers from the PDMS mold by first pulling the edges of the mold away from the device, and then gently lifting the device of the mold, being careful not to pull too rapidly, lest the thin walls between the mixing tubes do not de-mold. This layer should be relatively fully cured (not very sticky to the touch) because the bonding quality will be determined by the partial (very sticky) cure of the membrane. (15 minutes)

19. Gently drop the peristaltic mixing tube layer onto a partially cured membrane, being careful to select the membranes without dust contamination. Using a roll of label tape as a roller, push down the peristaltic mixing tube layer onto the membrane, squeezing out as many bubbles as possible. Also, tamp down the device using your finger and place a large steel weight on top of the device. (10 minutes)

20. Place the assemblies into the middle shelf of the oven for 20 minutes.

21. Remove the polycarbonate mold from the growth well device.

22. De-mold the growth well device layer, using the same procedure as for the mixing tube device layer, being careful not to dislodge the embedded oxygen sensors. Also make sure there is no PDMS remaining above the oxygen sensors. Any excess PDMS can be removed simply with tweezers.

23. Place each growth well device face up on a large square glass plate, taking care to keep the device covered with petri dishes.

24. Place a small drop of PDMS at the position of the pH sensors.

25. Position the pH sensor spots on each one of these PDMS drops to glue them in place.

26. Remove the mixing tube device layers bonded to the membrane from the oven. Using a razor blade, cut around the edges of the mixing device.

27. Carefully peel the device from the wafer, being careful not to peel too fast. Bending the device as you peel makes this easier.

28. Place the mixing tube-membrane assembly onto the silicon wafer of the alignment chuck, membrane side up. Position the glass plate that the growth well device layer is stuck to face down over the mixing tube-membrane assembly.

29. Raise the alignment chuck until the layers are almost touching, then align the two layers using the micrometers. When alignment is satisfactory, raise the alignment chuck until the layers are touching.

30. Using a roll of label tape as a roller, GENTLY roll the top of assembled device to ensure a good bond. Using your finger, gently tamp down especially in between the growth wells, and over the fluid injector valves. Be careful not to press too hard, lest the valve membranes seal to the channels.

31. Place the glass plates onto a 50°C hotplate and cover with aluminum foil to keep out the light.

32. Leave overnight or for at least 8 hours to fully cure the devices.

Appendix B

Enfors Glucose overflow metabolism model

This appendix describes the glucose overflow model from [25] and provides the parameters used to generate Figs. 7-5 and 7-6

B.1 Model Description

The total glucose flux is given by

$$qS = \frac{qS_{max}}{1 + A/K_{i,S}} \frac{S}{S + K_S} \tag{B.1}$$

Where initially, we assume $qS_{ox} = qS$ and calculate the proportion of the oxidative glucose flux towards anabolism and energy

$$qS_{ox,an} = (qS_{ox} - q_m) Y_{X/S,ox} \frac{C_X}{C_S} \tag{B.2}$$

$$qS_{ox,en} = qS_{ox} - qS_{ox,an} \tag{B.3}$$

Y_{AS}	Stoichiometry Acetate from Glucose	0.667	g/g
Y_{OA}	Stoichiometry of respiration O_2 consumed per acetate	1.067	g/g
Y_{OS}	Stoichiometry of respiration O_2 consumed per glucose	1.067	g/g
Y_{XA}	biomass yield on acetate	0.2 (0.4)	g/g
Y_{XSof}	biomass yield on glucose overflow	0.10 (0.15)	g/g
Y_{XSox}	biomass yield on glucose	0.50	g/g
C_A	carbon content mols/gram acetate	1/30	mol C/g-acetate
C_S	carbon content mols/gram glucose	1/30	mol C/g-glucose
C_X	carbon content mols/gram cell	0.04	mol C/g-cell
K_S	Monod model glucose inhibition	0.05	g/L
K_A	Monod model acetate inhibition	0.05	g/L
K_{iO}	Monod model acetate inhibition on O_2 uptake	15 (4)	g/L
K_{iS}	Monod model acetate inhibition on glucose uptake	26 (5)	g/L
qO_{max}	Maximum oxygen uptake rate	0.48	g/g/h
qS_{max}	Maximum glucose uptake rate	1.8 (1.5)	g/g/h
q_m	Glucose required for maintenance	0.04	g/g/h
qAc_{max}	Maximum acetate consumption rate	0.1	g/g/h
O_{sat}	Dissolved oxygen saturation	0.21	mmol-O2/L
C_{no}	Dissoved oxygen saturation from N.O. port	0.21	mmol-O_2/L
C_{nc}	Dissolved oxygen saturation from N.C. port	1.05	mmol-O_2/L
FoV	Time constant for gas mixing reservoir	6480	1/h
k_La	Oxygen transfer coefficient	288	1/h

Table B.1: Parameters in *E.coli* glucose overflow metabolism model to approximate fermentation on defined medium. The numbers in parentheses indicate values used in the original paper. There were therefore five fitting parameters used.

The glucose used for aerobic energy metabolism is oxidized through respiration and determines the oxygen demand to metabolize glucose,

$$qO_S = qS_{ox,en} Y_{O/S} \tag{B.4}$$

If $qO_S > qO_{thresh}$, where $qO_{thresh} = qO_{max}/(1 + A/K_{i,o}$,then $qS_{ox,an}$ and $qS_{ox,en}$ are reduced proprotionally such that $qS'_{ox,en} = qO_{thresh}/Y_{O/S}$ and $qS'_{ox,an} = qS_{ox,an}/qS_{ox,en} qS'_{ox,en}$

$$qS'_{ox} = qS'_{ox,an} + qS'_{ox,en} \tag{B.5}$$

Thus, the oxidative flux is of glucose is limited and the remaining glucose contributes to overflow metabolism,

$$qS_{of} = qS - qS'_{ox} \tag{B.6}$$

which contributes to an anabolic and energetic component.

$$qS_{of,an} = qS_{of} Y_{X/S,of} \frac{C_X}{C_S} \tag{B.7}$$

$$qS_{of,en} = qS_{of} - qS_{of,an} \tag{B.8}$$

Energy production due to overflow metabolism results in acetate production

$$qA_p = qS_{of,en} Y_{A/S} \tag{B.9}$$

and acetate consumption follows a Monod model

$$qA_c = qA_{c,max} \frac{A}{A + K_A} \tag{B.10}$$

resulting in anabolism due to acetate consumption.

$$qA_{c,an} = qA_c Y_{X/A} \frac{C_X}{C_A} \tag{B.11}$$

The oxidation of acetate is limited by the maximum total respiration rate qO_{max} and thus is constrained by

$$qA_{c,en} = qA_c - qA_{c,an} \leq (qO_{max} - qO_S)/Y_{O/A} \tag{B.12}$$

this results in the total oxygen demand,

$$qO = qO_S + qA_{c,en} Y_{O/A} \tag{B.13}$$

The growth rate is then calculated from the yield coefficents on oxidative metabolism of glucose, over flow metabolism of glucose, and metabolism of acetate.

$$\mu = (qS_{ox} - q_m)Y_{X/S,ox} + qS_{of}Y_{X/S,of} + qA_cY_{X/A} \tag{B.14}$$

B.2 Matlab code

B.2.1 Parameter definition

`enfors_params_129_3_thesisfig.m`

Defines parameters used in the model.

```
% parameters for pH controlled growth 12_9_05

enfors_globals;

YAS = .667;    % Stoichiometry Acetate from Glucose
YOA = 1.067;   % Stoichiometry of respiratio O2 consumed per acetate
YOS = 1.067;   % Stoichiometry of respiration O2 consumed per glucose
YXA = 0.2;     % biomass yield on acetate << 0.4

YXSof = 0.10;  % biomass yield on glucose overflow << 0.15
YXSox = 0.50;  % biomass yield on glucose oxidation

CA = 1/30;     % mol C/g-acetate carbon content mols/gram acetate
CS = 1/30;     % mol C/g-glucose carbon content mols/gram glucose
CX = 0.04;     % mol C/g-cell    carbon content mols/gram cell

KS = 0.05;     % g/L  Monod inhibition glucose-glucose
KA = 0.05;     % g/L  Monod inhibition acetate-acetate
KiO = 15;      % g/L  Monod inhibition acetate-oxygen << 4
KiS = 26;      % g/L  Monod inhibition acetate-glucose << 5

Osat = 0.21;     % mmol-O2/L
Cno = 0.21;      % air
Cnc = 0.21*5;    % pure oxygen
FoV = 1.8*3600;  % 1/s time constant for humidifier reservoir

Ocrit = 0.0081;  % mmol-O2/L critical concentration
kLa = 288;       % 1/h % bioreactor

% data for batch culture
qOmax = 15e-3*32;  % g/g/h
```

```
qSmax = 1.8;        % g/g/h  <<  1.4
qm = 0.04;          % g/g/h
qAcmax = 0.1;       % g/g/h

Fsample = 0;

% initial conditions
Yi = [40;      % glucose g/L
      0;       % acetate g/L
      0.013;   % biomass g/l
      100e-6;  % Volume L
      Cno;     % Dissolved oxygen
      Cno];    % Reservoir oxygen

duty = 0;
```

B.2.2 Dynamic model

`enfors_derivs_3.m`

Contents of dynamical model.

```
function dYdt = enfors_derivs(t,Y)
% Y = [S;A;X;V;O;RO];
% glucose, acetate, cell mass, volume, oxygen, reservoir oxygen

% This version has a more physically motivated oxygen threshold.
% This version includes the effect of the mixer reservoir

enfors_globals;

% calculate substrate metabolism
qS = qSmax./(1+Y(2)./KiS).*Y(1)./(Y(1)+KS);  % glucose flux g/(g-cell-h) (1)

qSox = qS;  % assume no overflow, no limitation (all sugar through
            % oxidative pathway)

qSoxan = max([0,(qSox-qm).*YXSox.*CX./CS]);  % glucose flux to biomass   (2)
qSoxen = qSox-qSoxan;                        % glucose flux to aerobic energy  (3)
                                             % metabolism

qOS = qSoxen.*YOS;  % oxygen used for glucose oxidation  (4)

% threshold for overflow metabolism.
qOthresh = min([qOmax./(1+Y(2)./KiO),...
```

```
                kLa.*(Y(6))*32./1e3./Y(3)]);

if qOS>=qOthresh;  % oxygen for glucose oxidation saturated

  qSoxen = qSoxen.*qOthresh./qOS;    % set oxidized glucose to max

  qSoxan = qSoxan.*qOthresh./qOS;    % proportional reduction in anabolic flux
  qSox = qSoxan+qSoxen;              % new oxidative flux (5)

  qOS = qOthresh;

  qSof = qS-qSox;   % compute overflow flux (6)

  qSofan = qSof.*YXSof.*CX./CS; % (7)
  qSofen = qSof-qSofan;         % (8)

  % acetate production through overflow mechanism
  qAp = qSofen.*YAS; % (9)
else
  qSof = 0;
  qAp = 0;
end

% acetate consumption
qAc = qAcmax.*Y(2)./(abs(Y(2))+KA);  % (10)
qAcan = qAc.*YXA.*CX./CA;            % (11) growth on acetate

qAcen = qAc-qAcan;     % (12) energy from acetate

qAthresh = (qOthresh-qOS)./YOA; % maximum acetate flux during respiration
if qAcen>qAthresh
  qAcan = qAc.*qAthresh./qAcen;
  qAcen = qAthresh;
  qAc = qAcan+qAcen;
end;

qO = qOS+qAcen.*YOA;   % total oxygen flux (13)

% growth rate
mu = max([0,(qSox-qm).*YXSox]) + qSof.*YXSof + qAc*YXA;  % (14)


dYdt = [[F(t)./Y(4).*(Sfeed(t)-Y(1)) - qS.*Y(3)].';   % dS/dt glucose (g/L)
        [(qAp-qAc).*Y(3)-(F(t)./Y(4)).*Y(2)].';       % dA/dt acetate (g/L)
        [(-F(t)./Y(4)+mu).*Y(3)].';                   % dX/dt cell mass (g/L)
        [F(t)-Fsample].';                             % dV/dt volume
        [kLa.*(Y(6)-Y(5)) - qO.*Y(3)./32.*1e3].';     % dO/dt DO2 (mmol/L)
        [-FoV*Y(6) + FoV*(Cnc*duty + Cno*(1-duty))]]; %dOr/dt
```

B.2.3 Main loop

`DOcontrol_sim_2_thesisfig.m`

Main loop that solves dynamical equations and implements intermittent dissolved oxygen controller.

```
enfors_params_129_3_thesisfig
firstinc = 1;

DO_thresh = 40;

tsamp = 1/60;  % hrs  sampling time

tend = 16;      % end time
t1 = 0;         % interval start
t2 = tsamp;     % interval end
Y1 = Yi;        % interval start state
ttot = [];
Ytot = [];
dutytot = [];
DOerror = 0;
DOerrorint = 0;
duty = 0;
dutyprev = 0;
gain_factor = 1;

notdone = 1;
while notdone

  [t,Y]=ode23s('enfors_derivs_3',[t1 t2],Y1);

  ttot = [ttot;t];
  Ytot = [Ytot;Y];

  %================================
  % PID controller
  %================================
  NO_percent = 100;
  NC_percent = 500;

  DOp = Y(end,5)./.21*100;

  DOerror_prev = DOerror;

  DOerror = DOp-DO_thresh;
  DOerrorint = DOerrorint+DOerror*(t2-t1);
```

```
  DOerrordiff = (DOerror-DOerror_prev)/(t2-t1);
  if DOerror>0
    DOerror = DOerror/2;
  end

  KP = 0.1;
  KI = 0.02*3600;
  KD = 0;

  duty = (-KP*DOerror-KI*DOerrorint-KD*DOerrordiff)./...                    50
         (NC_percent-NO_percent);

  if duty < 0, duty = 0; DOerrorint = 0;end;
  if duty > 1, duty = 1; DOerrorint = 0;end;

  dutytot = [dutytot;dutyprev*ones(size(t))];
  dutyprev = duty;

  t1 = t(end);
  t2 = t(end)+tsamp;                                                        60
  Y1 = Y(end,:);

  if t1>tend, notdone = 0; end
end;


figure
plot(ttot,Ytot(:,5)./.21*100)
set(gca,'ylim',[0 120]);
addaxis(ttot,Ytot(:,6)./.21*100)                                            70
addaxis(ttot,Ytot(:,3))
addaxis(ttot,Ytot(:,1))
addaxis(ttot,Ytot(:,2))
addaxislabel(1,'Dissolved Oxygen (%)')
addaxislabel(2,'Reservoir Oxygen (%)')
addaxislabel(3,'Biomas (g/L)');
addaxislabel(4,'Glucose (g/L)');
addaxislabel(5,'Acetate (g/L)');

enfors_growth_rate_2                                                        80
```

Appendix C

Mold Dimensions

Detailed specifications of the mold are provided in the form of the G-code used to generate them. All dimensions are in inches. Each G-code file corresponds to a specific tool, so there are no tool-changes within each file. The CNC machining system was from FlashcutCNC. Documentation is available at http://www.flashcutcnc.com.

C.1 Mixing tube and valve mold

The G-codes that define the top layer, mixing tube and valve mold are provided here.

C.1.1 Ports and Valves

`fluid_injector_test_top_ports_2.fgc`

This makes all of the actuation ports that are connected to pneumatic pressure lines. Use 1/16 ball end mill

```
(Ports for mixing tube mold)
(Use 1/16 diameter ball end mill)
(Origin is bottom left corner)

G90  (absolute positioning)
G00 Z0.01
```

```
( Mixing tube ports )
                                                                    10
X0.3401
Y0.0591
G01 Z-0.0787  F1.5   (plunge 2mm down )
G00 Z0.01

X0.4223              (move to next tube)
G01 Z-0.0787  F1.5   (plunge 2mm down )
G00 Z0.01

X0.5045              (move to next tube)                            20
G01 Z-0.0787  F1.5   (plunge 2mm down )
G00 Z0.01

X0.5867              (move to next tube)
G01 Z-0.0787  F1.5   (plunge 2mm down )
G00 Z0.01

X0.6689              (move to next tube)
G01 Z-0.0787  F1.5   (plunge 2mm down )
G00 Z0.01                                                           30

X0.7511              (move to next tube
G01 Z-0.0787  F1.5   (plunge 2mm down )
G00 Z0.01

X0.8333              (move to next tube)
G01 Z-0.0787  F1.5   (plunge 2mm down )
G00 Z0.01

Y2.9409              (move to top row)                              40
G01 Z-0.0787  F1.5   (plunge 2mm down )
G00 Z0.01

X0.7511              (move to next tube)
G01 Z-0.0787  F1.5   (plunge 2mm down )
G00 Z0.01

X0.6689              (move to next tube)
G01 Z-0.0787  F1.5   (plunge 2mm down )
G00 Z0.01                                                           50

X0.5867              (move to next tube)
G01 Z-0.0787  F1.5   (plunge 2mm down )
G00 Z0.01

X0.5045              (move to next tube)
```

```
G01 Z-0.0787  F1.5   (plunge 2mm down )
G00 Z0.01

X0.4223              (move to next tube)
G01 Z-0.0787  F1.5   (plunge 2mm down )
G00 Z0.01

X0.3401
G01 Z-0.0787  F1.5   (plunge 2mm down )
G00 Z0.01



(**********************NOW MAKE OTHER PORTS**********************)

(**********Channel valve ports***************)

X0.2657
Y2.7680
Z0.01

(*** well 1***)
G91  (incremental coordinates)
G01 Z-0.0887 F1.5
G00 Z0.1887

Y-0.5276
Z-0.1
G01 Z-0.0887 F1.5
G00 Z0.1887

(*** well 2***)
Y-0.1417
Z-0.1
G01 Z-0.0887 F1.5
G00 Z0.1887

Y-0.5276
Z-0.1
G01 Z-0.0887 F1.5
G00 Z0.1887


(*** well 3***)
Y-0.1417
Z-0.1
```

```
G01 Z-0.0887 F1.5
G00 Z0.1887

Y-0.5276
Z-0.1
G01 Z-0.0887 F1.5                                                    110
G00 Z0.1887

(*** well 4***)
Y-0.1417
Z-0.1
G01 Z-0.0887 F1.5
G00 Z0.1887

Y-0.5276
Z-0.1                                                                120
G01 Z-0.0887 F1.5
G00 Z0.1887


G90  (Absolute positioning)

(  Injector Ports  )
X0.0787
Y0.0591
Z0.01                                                                130
G01 Z-0.0787 F1.5

G00 Z0.01
X0.1609
Z0.01
G01 Z-0.0787 F1.5

G00 Z0.01
X0.2431
Z0.01                                                                140
G01 Z-0.0787 F1.5


G00 Z0.01

(  Injector metering  )
X0.3444

G00 Z0.01
Y0.2320                                                              150
G01 Z-0.040 F1.5
```

```
G00 Z0.01
Y0.7601
G01 Z-0.040 F1.5

G00 Z0.01
Y0.9013
G01 Z-0.040 F1.5

G00 Z0.01
Y1.4294
G01 Z-0.040 F1.5

G00 Z0.01
Y1.5706
G01 Z-0.040 F1.5

G00 Z0.01
Y2.0987
G01 Z-0.040 F1.5

G00 Z0.01
Y2.2399
G01 Z-0.040 F1.5

G00 Z0.01
Y2.7680
G01 Z-0.040 F1.5

G00 Z0.01
X0.4232
G01 Z-0.040 F1.5

G00 Z0.01
Y2.2399
G01 Z-0.040 F1.5

G00 Z0.01
Y2.0987
G01 Z-0.040 F1.5

G00 Z0.01
Y1.5706
G01 Z-0.040 F1.5

G00 Z0.01
Y1.4294
G01 Z-0.040 F1.5
```

```
G00 Z0.01
Y0.9013
G01 Z-0.040 F1.5

G00 Z0.01
Y0.7601
G01 Z-0.040 F1.5

G00 Z0.01
Y0.2320                                                    210
G01 Z-0.040 F1.5

G00 Z0.01


G00 Z2   (tool up)
Y0
X0
```

`fluid_injector_test_top_reservoirs_square.fgc`

This makes the pressure reservoir that allows pressurization of the fluid injectors. Use 1/8 square end mill

```
(Makes pressure  reservoirs using 1/8 square end mill)
(This version, use a 1/8 end mill and make a square side)

G90

G00 Z0.050
X0.1550

Y0.3678
G01 Z0 F1.5                                                10
M98 Preswell
G00 Z0.050

Y0.6793
G01 Z0 F1.5
M98 Preswell
G00 Z0.050

Y1.0371
G01 Z0 F1.5                                                20
M98 Preswell
G00 Z0.050

Y1.3486
```

```
G01 Z0 F1.5
M98 Preswell
G00 Z0.050

Y1.7064
G01 Z0 F1.5
M98 Preswell
G00 Z0.050

Y2.0179
G01 Z0 F1.5
M98 Preswell
G00 Z0.050

Y2.3757
G01 Z0 F1.5
M98 Preswell
G00 Z0.050

Y2.6872
G01 Z0 F1.5
M98 Preswell
G00 Z0.050


Oreswell
(make round reservoir)
(mill should be positioned at top of circle, at surface)

G91 (INCREMENTAL coordinates)

G01 X0 Y0 Z-0.0625 F1.5      (move down to reservior depth)
G02 X0 Y0 I0 J-0.0275 F1.5   (clockwise move)
G00 X0 Y0 Z0.0625            (move back to starting point)

G90  (Back to ABSOLUTE coordinates)

M99
```

`fluid_injector_test_top_delivery_tubes_2.fgc`

This makes the channels that connect the shared metering valves and also the channel that connects the pressure reservoirs. Use 1/32 ball end mill.

```
(  Fluid injector lines )

(use 1/32 ball end mill)
```

```
G90

G00 Z0.010
X0.1609
Y0.0591

(reservoir pressurization channel)

G01 Z-0.0394 F1.5  (for 0.0313 wide channel)
Y2.6597
G00 Z0.010

Y2.7680
X0.3444

G01 Z-0.017 F1.5  (for 0.0313 wide channel)
Y0.0591
G00 Z0.010

X0.4232
G01 Z-0.017 F1.5  (for 0.0313 wide channel)
Y2.7680

G00 Z0.2
```

C.1.2 Mixing Tubes

These files describe the variable width mixing tubes. All tools are ball end mills. Diameter is given in the file name.

`mixing_tubes_variable_width_1_16_halfwell_2.fgc`

```
(G-code for 1/16 end mill)

(Program zero will be set to the lower left corner of the)
(1x3 inch blank, Z=0 is the surface of the piece)


(***************FIRST WELL*******************)
G90  (Absolute positioning to move to center of first well)
G00 Z0.050          (rapid move to 0.050 above work surface)
X0.5866
Y0.4961  (rapid move to center of first well)
```

```
G52 X0.5866 Y0.4961 Z0
M98 Ptube16
G52 X0 Y0 Z0
G00 Z0.050

(**********SECOND WELL**********)
G90  (Absolute positioning to move to center of first well)
G00 Z0.050          (rapid move to 0.1 above work surface)
X0.5866 Y1.1654  (rapid move to center of second  well)

G52 X0.5866 Y1.1654 Z0
M98 Ptube16
G52 X0 Y0 Z0
G00 Z0.050

(**********THIRD WELL**********)
G90  (Absolute positioning to move to center of first well)
G00 Z0.050          (rapid move to 0.1 above work surface)
X0.5866 Y1.8346  (rapid move to center of first well)

G52 X0.5866 Y1.8346 Z0
M98 Ptube16
G52 X0 Y0 Z0
G00 Z0.050

(**********FOURTH WELL**********)
G90  (Absolute positioning to move to center of first well)
G00 Z0.050          (rapid move to 0.1 above work surface)
X0.5866 Y2.5039  (rapid move to center of first well)

G52 X0.5866 Y2.5039 Z0
M98 Ptube16
G52 X0 Y0 Z0
G00 Z0.050

(**********move off surface for tool change **********)
G90
G00 Z.2
Y0
X0

(********** SUBROUTINE sensordiv to make sensor divots*******)
Otube16
(calling program should have positioned mill at old center of well)
(local coordinate system is set to that point)

G00 Z0.010
```

```
(add tube 3 top in new version)
G00 X-0.0975
Y0.0350
G01 Z-0.0394 F1.5
Y0.2070
G00 Z0.010


(tube 4 top)
G00 X-0.0156
Y0.1010
G01 Z-0.0394 F1.5
Y0.2640
G00 Z0.010


(tube 4 bottom)
G00 X0.0156
Y-0.2640
G01 Z-0.0394 F1.5
Y-0.1010
G00 Z0.010

(tube 6 bottom)
G00 X0.1487
G01 Z-0.0394 F1.5
Y-0.2640
G00 Z0.010

(tube 7 top)
G00 X0.2466
Y0.042
G01 Z-0.0394 F1.5
Y0.2400
G00 Z0.010

G00 Z0.050
X0


M99
```

mixing_tubes_variable_width_1_32_halfwell_2.fgc

```
(G-code for 1/32 end mill)
```

```
(Program zero will be set to the lower left corner of the)
(1x3 inch blank, Z=0 is the surface of the piece)


(****************FIRST WELL*********************)
G90  (Absolute positioning to move to center of first well)
G00 Z0.050          (rapid move to 0.050 above work surface)
X0.5866
Y0.4961  (rapid move to center of first well)

G52 X0.5866 Y0.4961 Z0
M98 Ptube32
G52 X0 Y0 Z0
G00 Z0.050

(****************SECOND WELL*********************)
G90  (Absolute positioning to move to center of first well)
G00 Z0.050          (rapid move to 0.1 above work surface)
X0.5866 Y1.1654  (rapid move to center of second  well)

G52 X0.5866 Y1.1654 Z0
M98 Ptube32
G52 X0 Y0 Z0
G00 Z0.050

(****************THIRD WELL*********************)
G90  (Absolute positioning to move to center of first well)
G00 Z0.050          (rapid move to 0.1 above work surface)
X0.5866 Y1.8346  (rapid move to center of first well)

G52 X0.5866 Y1.8346 Z0
M98 Ptube32
G52 X0 Y0 Z0
G00 Z0.050

(****************FOURTH WELL*********************)
G90  (Absolute positioning to move to center of first well)
G00 Z0.050          (rapid move to 0.1 above work surface)
X0.5866 Y2.5039  (rapid move to center of first well)

G52 X0.5866 Y2.5039 Z0
M98 Ptube32
G52 X0 Y0 Z0
G00 Z0.050

(******************move off surface for tool change ******************)
G90
G00 Z.2
```

```
Y0
X0

(********************* SUBROUTINE sensordiv to make sensor divots*******)
Otube32
(calling program should have positioned mill at old center of well)
(local coordinate system is set to that point)

G00 Z0.010

(tube 3 top)
(no 1/32 tube three in new version)

(tube 4 center)
G00 X0
Y0.1010
G01 Z-0.035 F1.5
Y-0.1010
G00 Z0.010

(tube 5 bottom)
G00 X0.0822
Y-0.0350
G01 Z-0.035 F1.5
Y-0.2797
G00 Z0.010

(tube 6 middle)
G00 X0.1644
Y-0.0200
G01 Z-0.035 F1.5
Y-0.1010
G00 Z0.010



G00 Z0.050
X0


M99
```

`mixing_tubes_variable_width_3_32_halfwell_2.fgc`

```
(G-code for 3/32 end mill)
```

```
(Program zero will be set to the lower left corner of the)
(1x3 inch blank, Z=0 is the surface of the piece)


(**********FIRST WELL**********)
G90  (Absolute positioning to move to center of first well)
G00 Z0.050          (rapid move to 0.050 above work surface)
X0.5866                                                          10
Y0.4961  (rapid move to center of first well)

G52 X0.5866 Y0.4961 Z0
M98 Ptube3_32
G52 X0 Y0 Z0
G00 Z0.050

(**********SECOND WELL**********)
G90  (Absolute positioning to move to center of first well)
G00 Z0.050          (rapid move to 0.1 above work surface)       20
X0.5866 Y1.1654  (rapid move to center of second  well)

G52 X0.5866 Y1.1654 Z0
M98 Ptube3_32
G52 X0 Y0 Z0
G00 Z0.050

(**********THIRD WELL**********)
G90  (Absolute positioning to move to center of first well)
G00 Z0.050          (rapid move to 0.1 above work surface)       30
X0.5866 Y1.8346  (rapid move to center of first well)

G52 X0.5866 Y1.8346 Z0
M98 Ptube3_32
G52 X0 Y0 Z0
G00 Z0.050

(**********FOURTH WELL**********)
G90  (Absolute positioning to move to center of first well)
G00 Z0.050          (rapid move to 0.1 above work surface)       40
X0.5866 Y2.5039  (rapid move to center of first well)

G52 X0.5866 Y2.5039 Z0
M98 Ptube3_32
G52 X0 Y0 Z0
G00 Z0.050

(**********move off surface for tool change **********)
G90
G00 Z.2                                                          50
```

```
Y0
X0

(********************** SUBROUTINE sensordiv to make sensor divots*******)
Otube3_32
(calling program should have positioned mill at old center of well)
(local coordinate system is set to that point)

G00 Z0.010

(tube 3 bottom)
G00 X-0.0822
Y0.0350
G01 Z-0.0500 F1.5
Y-0.2070      (not as long in new version)
G00 Z0.010

(tube 7 bottom)
G00 X0.2466
Y-0.2070
G01 Z-0.0500 F1.5
Y-0.0700
G00 Z0.010

(tube 5 top)
G00 X0.0822
Y-0.0350
G01 Z-0.0500 F1.5
Y0.2484
G00 Z0.010

G00 Z0.050
X0


M99
```

`mixing_tubes_variable_width_3_64_halfwell_2.fgc`

```
(G-code for 3/64 end mill)

(Program zero will be set to the lower left corner of the)
(1x3 inch blank, Z=0 is the surface of the piece)


(***************FIRST WELL*******************)
```

```
G90  (Absolute positioning to move to center of first well)
G00 Z0.050          (rapid move to 0.050 above work surface)
X0.5866                                                          10
Y0.4961  (rapid move to center of first well)

G52 X0.5866 Y0.4961 Z0
M98 Ptube3_64
G52 X0 Y0 Z0
G00 Z0.050

(****************SECOND WELL*********************)
G90  (Absolute positioning to move to center of first well)
G00 Z0.050          (rapid move to 0.1 above work surface)       20
X0.5866 Y1.1654  (rapid move to center of second  well)

G52 X0.5866 Y1.1654 Z0
M98 Ptube3_64
G52 X0 Y0 Z0
G00 Z0.050

(****************THIRD WELL*********************)
G90  (Absolute positioning to move to center of first well)
G00 Z0.050          (rapid move to 0.1 above work surface)       30
X0.5866 Y1.8346  (rapid move to center of first well)

G52 X0.5866 Y1.8346 Z0
M98 Ptube3_64
G52 X0 Y0 Z0
G00 Z0.050

(****************FOURTH WELL*********************)
G90  (Absolute positioning to move to center of first well)
G00 Z0.050          (rapid move to 0.1 above work surface)       40
X0.5866 Y2.5039  (rapid move to center of first well)

G52 X0.5866 Y2.5039 Z0
M98 Ptube3_64
G52 X0 Y0 Z0
G00 Z0.050

(******************move off surface for tool change ******************)
G90
G00 Z.2                                                          50
Y0
X0

(********************* SUBROUTINE sensordiv to make sensor divots*******)
Otube3_64
```

```
(calling program should have positioned mill at old center of well)
(local coordinate system is set to that point)

G00 Z0.010

(tube 7 middle)
G00 Y-0.0700
X0.2466
G01 Z-0.035 F1.5
Y0.0420
G00 Z0.010

(tube 6 top)
G00 X0.1722
Y-0.0200
G01 Z-0.035 F1.5
Y0.2718
G00 Z0.010

G00 Z0.050
X0


M99
```

`mixing_tubes_variable_width_connection_halfwell.fgc`

This connects the membrane sections of each growth well together.

```
(make connections between wells using 1/32 ball end mill)

G90

G00 Z0.010

(tube 1**************************)
X0.5045

Y0.0591
G01 Z-0.030 F1.5
Y0.2891
G00 Z0.010

Y0.7031
G01 Z-0.030 F1.5
Y0.9584
G00 Z0.010
```

```
Y1.3724
G01 Z−0.030 F1.5
Y1.6277
G00 Z0.010

Y2.0417
G01 Z−0.030 F1.5
Y2.2970
G00 Z0.010

Y2.7110
G01 Z−0.030 F1.5
Y2.9409
G00 Z0.010


(tube 2 **********)
X0.5867

Y2.9409
G01 Z−0.030 F1.5
Y2.7110
G00 Z0.010

Y2.2970
G01 Z−0.030 F1.5
Y2.0417
G00 Z0.010

Y1.6277
G01 Z−0.030 F1.5
Y1.3724
G00 Z0.010

Y0.9584
G01 Z−0.030 F1.5
Y0.7031
G00 Z0.010

Y0.2891
G01 Z−0.030 F1.5
Y0.0591
G00 Z0.010

(tube 3**********)
X0.6689
```

```
Y0.0591
G01 Z−0.030 F1.5
Y0.2891
G00 Z0.010

Y0.7031
G01 Z−0.030 F1.5
Y0.9584
G00 Z0.010

Y1.3724
G01 Z−0.030 F1.5
Y1.6277
G00 Z0.010

Y2.0417
G01 Z−0.030 F1.5
Y2.2970
G00 Z0.010

Y2.7110
G01 Z−0.030 F1.5
Y2.9409
G00 Z0.010

(tube 4**********)
X0.7511

Y2.9409
G01 Z−0.030 F1.5
Y2.7110
G00 Z0.010

Y2.2970
G01 Z−0.030 F1.5
Y2.0417
G00 Z0.010

Y1.6277
G01 Z−0.030 F1.5
Y1.3724
G00 Z0.010

Y0.9584
G01 Z−0.030 F1.5
Y0.7031
G00 Z0.010
```

```
Y0.2891
G01 Z-0.030 F1.5
Y0.0591
G00 Z0.010

(tube 5**************************)
X0.8333

Y0.0591
G01 Z-0.030 F1.5
Y0.2891
G00 Z0.010

Y0.7031
G01 Z-0.030 F1.5
Y0.9584
G00 Z0.010

Y1.3724
G01 Z-0.030 F1.5
Y1.6277
G00 Z0.010

Y2.0417
G01 Z-0.030 F1.5
Y2.2970
G00 Z0.010

Y2.7110
G01 Z-0.030 F1.5
Y2.9409
G00 Z0.010
```

C.2 Well mold

`fluid_injector_test_bottom_wells.fgc`

This carves out the growth wells. Use 1/4 square end mill

```
(wells for fluid injector.  curved one side, flat the other)
(use 1/4 square end mill)

(Program zero will be set to the lower left corner of the)
(1x3 inch blank, Z=0 is the surface of the piece)
```

```
(****************FIRST WELL*********************)
G90  (Absolute positioning to move to center of first well)
G00 Z0.050          (rapid move to 0.050 above work surface)
X0.5866
Y0.4961  (rapid move to center of first well)

G52 X0.5866 Y0.4961 Z0
M98 Pwell
G52 X0 Y0 Z0
G00 Z0.050

(****************SECOND WELL*********************)
G90  (Absolute positioning to move to center of first well)
G00 Z0.050          (rapid move to 0.1 above work surface)
X0.5866 Y1.1654  (rapid move to center of second  well)

G52 X0.5866 Y1.1654 Z0
M98 Pwell
G52 X0 Y0 Z0
G00 Z0.050

(****************THIRD WELL*********************)
G90  (Absolute positioning to move to center of first well)
G00 Z0.050          (rapid move to 0.1 above work surface)
X0.5866 Y1.8346  (rapid move to center of first well)

G52 X0.5866 Y1.8346 Z0
M98 Pwell
G52 X0 Y0 Z0
G00 Z0.050

(****************FOURTH WELL*********************)
G90  (Absolute positioning to move to center of first well)
G00 Z0.050          (rapid move to 0.1 above work surface)
X0.5866 Y2.5039  (rapid move to center of first well)

G52 X0.5866 Y2.5039 Z0
M98 Pwell
G52 X0 Y0 Z0
G00 Z0.050

(******************move off surface for tool change ********************)
G90
G00 Z.2
Y0
X0

(********************** SUBROUTINE sensordiv to make sensor divots*******)
```

```
Owell
(calling program should have positioned mill at old center of well)
(local coordinate system is set to that point)

G01 Z-0.0197 F1.5     (this should make a 500um deep well)
X-0.0128
Y0.1703
X0.1703
Y-0.1703
X-0.0128
Y0
X0.1703 Y0.1703
G02 X0.1703 Y-0.1703 I-0.1703 J-0.1703 F1.5
G01 X0 Y0 F1.5
G00 Z0.050

M99
```

`fluid_injector_test_sensor_divots_3mm.fgc`

This makes the shallow divots for the optical sensors.

```
(this makes sensor divots)
(use 1/8 end mill)
(assumes 500um deep wells)

(G-code for large well bioreactors--WELLS)
(this version also implements curved sides)

(Inch units standard)

(Program zero will be set to the lower left corner of the)
(1x3 inch blank, Z=0 is the surface of the piece)


(**********FIRST WELL**********)
G90  (Absolute positioning to move to center of first well)
G00 Z0.1          (rapid move to 0.1 above work surface)
X0.5866
Y0.4961  (rapid move to center of first well)
Z0.01             (rapid move to work surface)

G01 Z0 F1.5
M98 Psensordiv
```

```
G00 Z0.1

(***************SECOND WELL*********************)
G90  (Absolute positioning to move to center of first well)
G00 Z0.1          (rapid move to 0.1 above work surface)
X0.5866 Y1.1654  (rapid move to center of first well)
Z0.01             (rapid move to work surface)

G01 Z0 F1.5
M98 Psensordiv
G00 Z0.1

(***************THIRD WELL*********************)
G90  (Absolute positioning to move to center of first well)
G00 Z0.1          (rapid move to 0.1 above work surface)
X0.5866 Y1.8346  (rapid move to center of first well)
Z0.01             (rapid move to work surface)

G01 Z0 F1.5
M98 Psensordiv
G00 Z0.1

(***************FOURTH WELL*********************)
G90  (Absolute positioning to move to center of first well)
G00 Z0.1          (rapid move to 0.1 above work surface)
X0.5866 Y2.5039  (rapid move to center of first well)
Z0.01             (rapid move to work surface)

G01 Z0 F1.5
M98 Psensordiv
G00 Z0.1

(******************move off surface for tool change ********************)
G90
G00 Z.2
Y0
X0

(********************** SUBROUTINE sensordiv to make sensor divots*******)
Osensordiv
(calling program should have positioned mill at zero level)
(this assumes 500um deep wells, or 19.7 mils)
(divots will be 12 mils for center and 10 mill for sides)

G91 (incremental units)
G01 Z-0.0317 F1.5    (this should make a 2mil or 50um divot)
G00 Z0.0317
```

```
G00 X0.2206 Y0.2206
G01 Z-0.0297 F1.5    (this should make a 2mil or 50um divot)
G00 Z0.0297

Y-0.4412
G01 Z-0.0297 F1.5    (this should make a 2mil or 50um divot)
G00 Z0.0297

X-0.2206 Y0.2206                                              80

G90  (back to absolute mode)

M99
```

`fluid_injector_test_bottom_reservoirs_2.fgc`

This makes the hemispherical fluid reservoirs. Use 3/16 ball end mill

```
(Makes reservoirs using 3/16 ball end mill)
(depth 0.0675 for 0.180 diameter reservoirs)
(volume is 16.2uL)

G90

G00 Z0.050
X0.1550

Y0.3403                                                       10
G01 Z-0.0675 F1.5
G00 Z0.050

Y0.6518
G01 Z-0.0675 F1.5
G00 Z0.050

Y1.0096
G01 Z-0.0675 F1.5
G00 Z0.050                                                    20

Y1.3211
G01 Z-0.0675 F1.5
G00 Z0.050

Y1.6789
G01 Z-0.0675 F1.5
```

```
G00 Z0.050

Y1.9904
G01 Z-0.0675 F1.5
G00 Z0.050

Y2.3482
G01 Z-0.0675 F1.5
G00 Z0.050

Y2.6597
G01 Z-0.0675 F1.5
G00 Z0.050
```

`fluid_injector_test_bottom_channels_2_DI.fgc`

This makes the fluid injector channels and the innoculation channels. Use 1/32 ball end mill.

```
(Program zero will be set to the lower left corner of the)
(1x3 inch blank, Z=0 is the surface of the piece)


(**********FIRST WELL**********)
G90  (Absolute positioning to move to center of first well)
G00 Z0.050          (rapid move to 0.050 above work surface)
X0.5866
Y0.4961  (rapid move to center of first well)

G52 X0.5866 Y0.4961 Z0
M98 Pchannels
G52 X0 Y0 Z0
G00 Z0.050

(**********SECOND WELL**********)
G90  (Absolute positioning to move to center of first well)
G00 Z0.050          (rapid move to 0.1 above work surface)
X0.5866 Y1.1654  (rapid move to center of second  well)

G52 X0.5866 Y1.1654 Z0
M98 Pchannels
G52 X0 Y0 Z0
G00 Z0.050

(**********THIRD WELL**********)
G90  (Absolute positioning to move to center of first well)
G00 Z0.050          (rapid move to 0.1 above work surface)
X0.5866 Y1.8346  (rapid move to center of first well)
```

```
                                                                        30
G52 X0.5866 Y1.8346 Z0
M98 Pchannels
G52 X0 Y0 Z0
G00 Z0.050

(****************FOURTH WELL*********************)
G90  (Absolute positioning to move to center of first well)
G00 Z0.050          (rapid move to 0.1 above work surface)
X0.5866 Y2.5039  (rapid move to center of first well)
                                                                        40
G52 X0.5866 Y2.5039 Z0
M98 Pchannels
G52 X0 Y0 Z0
G00 Z0.050

(******************move off surface for tool change ********************)
G90
G00 Z.2
Y0
X0                                                                      50

(********************** SUBROUTINE sensordiv to make sensor divots*******)
Ochannels
(calling program should have positioned mill at old center of well)
(local coordinate system is set to that point)

G00 Y0.2640          (upper right channel)
X0.1956
G01 Z-0.007 F1.5     (move to channel depth -- extra deep innoculation ports)
X0.3543                                                                 60

G00 Z0.050           (lower right channel)
X0.1956
Y-0.2640
G01 Z-0.007 F1.5     (move to channel depth -- extra deep innoculation ports)
X0.3543

G00 Z0.050           (lower left straight)
X-0.0509
G01 Z-0.005 F1.5     (move to channel depth)                            70
X-0.3700
X-0.4316 Y-0.1558  (diagonal branch to center of well)


G00 Z0.050           (lower left diagonal channel)
X-0.5276 Y-0.2640
G01 Z-0.005 F1.5     (move to channel depth)
```

```
X-0.4316 Y-0.1558

G00 Z0.050          (lower left crooked channel)
X-0.4316 Y-0.1558
G01 Z-0.005 F1.5    (move to channel depth)
X-0.3520 Y-0.0659
Y-0.0300
X-0.5276

G00 Z0.050          (upper left straight)
X-0.0509
Y0.2640
G01 Z-0.005 F1.5    (move to channel depth)
X-0.3700
X-0.4316 Y0.1558  (diagonal branch to center of well)


G00 Z0.050          (upper left diagonal channel)
X-0.5276 Y0.2640
G01 Z-0.005 F1.5    (move to channel depth)
X-0.4316 Y0.1558

G00 Z0.050          (upper left crooked channel)
X-0.4316 Y0.1558
G01 Z-0.005 F1.5    (move to channel depth)
X-0.3520 Y0.0659
Y0.0300
X-0.5276



G00 Z0.050
Y0
X0


M99
```

`fluid_injector_test_bottom_channels_2_DI_well_trench.fgc`

This makes the fluid injector channels deep in the reservoir. Use 1/32 ball end mill.

```
(Program zero will be set to the lower left corner of the)
(1x3 inch blank, Z=0 is the surface of the piece)
```

```
(**********FIRST WELL**********)
G90  (Absolute positioning to move to center of first well)
G00 Z0.050          (rapid move to 0.050 above work surface)
X0.5866
Y0.4961  (rapid move to center of first well)

G52 X0.5866 Y0.4961 Z0
M98 Pchannels
G52 X0 Y0 Z0
G00 Z0.050

(**********SECOND WELL**********)
G90  (Absolute positioning to move to center of first well)
G00 Z0.050          (rapid move to 0.1 above work surface)
X0.5866 Y1.1654  (rapid move to center of second  well)

G52 X0.5866 Y1.1654 Z0
M98 Pchannels
G52 X0 Y0 Z0
G00 Z0.050

(**********THIRD WELL**********)
G90  (Absolute positioning to move to center of first well)
G00 Z0.050          (rapid move to 0.1 above work surface)
X0.5866 Y1.8346  (rapid move to center of first well)

G52 X0.5866 Y1.8346 Z0
M98 Pchannels
G52 X0 Y0 Z0
G00 Z0.050

(**********FOURTH WELL**********)
G90  (Absolute positioning to move to center of first well)
G00 Z0.050          (rapid move to 0.1 above work surface)
X0.5866 Y2.5039  (rapid move to center of first well)

G52 X0.5866 Y2.5039 Z0
M98 Pchannels
G52 X0 Y0 Z0
G00 Z0.050

(**********move off surface for tool change **********)
G90
G00 Z.2
Y0
X0
```

```
(********************* SUBROUTINE sensordiv to make sensor divots*******)
Ochannels
(calling program should have positioned mill at old center of well)
(local coordinate system is set to that point)

G00 Z0.050          (upper left trench)
X-0.3817
Y0.2340                                                              60
G01 Z-0.0625 F1.5
X-0.4316 Y0.1558

G00 Z0.050
Y-0.1558
G01 Z-0.0625 F1.5
X-0.3817 Y-0.2340

G00 Z0.050
Y0                                                                   70
X0


M99
```

`fluid_injector_test_bottom_ports.fgc`

This makes the ports for the fluid injectors and the growth wells. Use 1/16 ball end mill.

```
(ports for new fluid injector)

G90

G00 Z0.050
X0.0591

Y0.2320
G83 R0.020 Z-0.0394 Q-0.070 F1.5
                                                                     10
Y0.4486
Y0.5436
Y0.7611
Y0.9013
Y1.1179
```

```
Y1.2129
Y1.4304
Y1.5706
Y1.7872
Y1.8822
Y2.0997
Y2.2399
Y2.4565
Y2.5515
Y2.7690

X0.9418
Y2.2399
Y2.0997
Y1.5706
Y1.4304
Y0.9013
Y0.7611
Y0.2320
```

C.3 Moat

`moat.fgc`

This makes the moat around the mold that in negative forms the walls of the mold and therefore, the total thickness of the device.

```
(cut moat to define edges of mold)
(1/8 inch end mill, go 1/8 inch deep)

(0,0 is the same as for the other programs)

G90 (Absolute positioning)
G00 Z0.1
X-0.125
Y-0.125
Z0.01

G01 Z-0.125 F1
X1.125

G00 Z1   (tool up to clean chips)
M00
G00 Z0.01

G01 Z-0.125 F1
```

```
Y1.5

G00 Z1
M00
G00 Z0.01

G01 Z-0.125 F1
Y3.125

G00 Z1
M00
G00 Z0.01

G01 Z-0.125 F1
X-0.125

G00 Z1
M00
G00 Z0.01

G01 Z-0.125 F1
Y1.5

G00 Z1
M00
G00 Z0.01

G01 Z-0.125 F1
Y-0.125

G00 Z2
```

C.4 Gasket mold

This is the external mold corresponding to the mixer and valve mold. It defines the actuation ports and all of the gaskets around those ports and the injection sites.

`nipples_drill_1.fgc`

This file drills all of the holes that will accept teflon coated steel pins that define the actuation ports. Use #64 drill.

```
(NO SHRINK. Accounts for thermal expansion)
(this is the DRILL file for the nipple plate)
```

```
(use #64 drill)


G90  (absolute positioning)

(*************Mixing tube ports******************)
G00 Z0.1
X0.0787                                                          10
Y0.0591
G83 R0.05 Z-0.280 Q0.075 F1.5  (peck drilling cycle)
X0.1609
X0.2431


(************* bottom row of mixing tube ports ************* )
G00 Z0.1
X0.3401
Y0.0591                                                          20
G83 R0.05 Z-0.280 Q0.075 F1.5  (peck drilling cycle)
X0.4223
X0.5045
X0.5867
X0.6689
X0.7511
X0.8333

(***********Channel valve ports***************)
G00 Z0.1                                                         30
X0.2657
Y0.2325
G83 R0.05 Z-0.280 Q0.075 F1.5  (peck drilling cycle)
Y0.7601
Y0.9018
Y1.4294
Y1.5711
Y2.0987
Y2.2404
Y2.7680                                                          40

(*************  Top row mixing ports******************)
G00 Z0.1
X0.3401
Y2.9409
G83 R0.05 Z-0.280 Q0.075 F1.5  (peck drilling cycle)
X0.4223
X0.5045
X0.5867
X0.6689                                                          50
```

```
X0.7511
X0.8333


( ******************** Alignment corner posts ******************)
G00 Z0.1
X1.0445
Y3.0445
G83 R0.05 Z-0.280 Q0.075 F1.5  (peck drilling cycle)
X-0.0445                                                          60
Y-0.0445
X1.0445
```

`nipples_around_holes_16.fgc`

This file makes the gaskets, or nipples around the actuation port holes. This is simply a square gasket made using a 1/16 square end mill.

```
(this version simply uses a 1/16 flat end mill to do the nipple)

G90  (absolute positioning)

(*************Mixing tube ports******************)
G00 Z0.02
X0.0787
Y0.0591
M98 Pnipple
G00 X0.1609                                                       10
M98 Pnipple
G00 X0.2431
M98 Pnipple

(************* bottom row of mixing tube ports ************* )
G00 Z0.02
X0.3401
Y0.0591
M98 Pnipple
G00 X0.4223                                                       20
M98 Pnipple
G00 X0.5045
M98 Pnipple
G00 X0.5867
M98 Pnipple
G00 X0.6689
M98 Pnipple
```

```
G00 X0.7511
M98 Pnipple
G00 X0.8333
M98 Pnipple

(**********Channel valve ports**********)
G00 Z0.02
X0.2657
Y0.2325
M98 Pnipple
G00 Y0.7601
M98 Pnipple
G00 Y0.9018
M98 Pnipple
G00 Y1.4294
M98 Pnipple
G00 Y1.5711
M98 Pnipple
G00 Y2.0987
M98 Pnipple
G00 Y2.2404
M98 Pnipple
G00 Y2.7680
M98 Pnipple

(********** Top row mixing ports**********)
G00 Z0.02
X0.3401
Y2.9409
M98 Pnipple
G00 X0.4223
M98 Pnipple
G00 X0.5045
M98 Pnipple
G00 X0.5867
M98 Pnipple
G00 X0.6689
M98 Pnipple
G00 X0.7511
M98 Pnipple
G00 X0.8333
M98 Pnipple

(**********Subroutine for Nipples**********)
Onipple
(subroutine to etch nipple using 60 degree mechanical etch bit)
(calling function will have moved bit to CENTER of hole, 0.1 above surface)
```

```
G91 (incremental positining mode)

G01 Z-0.0317 F1
G00 Z0.0317

G90  (back to absolute mode)
M99
```

`nipples_only_direct.fgc`

This file makes the gaskets, or nipples around the fluid injection ports. There is no central hole, so use a 60° pointed mechanical etching tool, typically used for printed circuit board etching.

```
(Nipples only NO SHRINK)
(this version minimizes backlash accumulation)

G90
G00 Z0.02
X0.0591
Y0.2565
M98 Pnipple

G00 Y0.4730
M98 Pnipple

G00 Y0.5680
M98 Pnipple

G00 Y0.7846
M98 Pnipple

G00 Y0.9258
M98 Pnipple

G00 Y1.1423
M98 Pnipple

G00 Y1.2373
M98 Pnipple

G00 Y1.4539
M98 Pnipple

G00 Y1.5951
M98 Pnipple
```

```
G00 Y1.8116
M98 Pnipple

G00 Y1.9066
M98 Pnipple

G00 Y2.1232
M98 Pnipple

G00 Y2.2644
M98 Pnipple

G00 Y2.4809
M98 Pnipple

G00 Y2.5759
M98 Pnipple

G00 Y2.7925
M98 Pnipple

G00 X0.9409
M98 Pnipple

G00 Y2.2644
M98 Pnipple

G00 Y2.1232
M98 Pnipple

G00 Y1.5951
M98 Pnipple

G00 Y1.4539
M98 Pnipple

G00 Y0.9258
M98 Pnipple

G00 Y0.7846
M98 Pnipple

G00 Y0.2565
M98 Pnipple
```

```
(**********Subroutine for Nipples**********)
Onipple
(subroutine to etch nipple using 60 degree mechanical etch bit)
(calling function will have moved bit to TOP of hole, 0.02 above surface)

G91 (incremental positining mode)

(G00 Y0.0245)                  (move to top of circle)
G01 Z-0.0317 F1.5              (move to etch depth)
G02 X0 Y0 I0 J-0.0245 F1.5  (draw circle)                    90
G00 Z0.0317                    (return to 0.02 above surface)
(Y-0.0245)                     (return to center of circle)

G90  (back to absolute positining mode)

M99
```

`nipple_plate_1mm_fibers_direct.fgc`

This file makes a hole that will accept a 1/16 diameter rod to open a recess for the 1mm diameter optical density fiber.

```
(this makes holes for 1mm fibers)
(use 1/16 drill)

(this uses direct coordinates rather than relative moves for)
(each well -- reduces backlash accumulation)

G90 (absolute positioning)
G00 Z0.050
X0.2666
Y0.4961                                                     10
G83 R0.020 Z-0.280 Q0.075 F1.5  (peck drilling cycle)
Y1.1654
Y1.8347
Y2.5040

X0.9066
Y1.8347
Y1.1654
Y0.4961
```

C.5 Fiber bundle recess mold

`bottom_plate_2mm_fibers_total.fgc`

This file makes the holes that will accept 1/8 inch diameter polished posts to make the fiber bundle recesses.

```
(Program zero will be set to the lower left corner of the)
(1x3 inch blank, Z=0 is the surface of the piece)


(**********FIRST WELL**********)
G90  (Absolute positioning to move to center of first well)
G00 Z0.1          (rapid move to 0.1 above work surface)
X0.5866
Y0.4961  (rapid move to center of first well)
Z0.01             (rapid move to work surface)

M98 Pfiberdrill
G00 Z0.1

(**********SECOND WELL**********)
G90  (Absolute positioning to move to center of first well)
G00 Z0.1          (rapid move to 0.1 above work surface)
X0.5866 Y1.1654  (rapid move to center of first well)
Z0.01             (rapid move to work surface)

M98 Pfiberdrill
G00 Z0.1

(**********THIRD WELL**********)
G90  (Absolute positioning to move to center of first well)
G00 Z0.1          (rapid move to 0.1 above work surface)
X0.5866 Y1.8346  (rapid move to center of first well)
Z0.01             (rapid move to work surface)

M98 Pfiberdrill
G00 Z0.1

(**********FOURTH WELL**********)
G90  (Absolute positioning to move to center of first well)
G00 Z0.1          (rapid move to 0.1 above work surface)
X0.5866 Y2.5039  (rapid move to center of first well)
Z0.01             (rapid move to work surface)

M98 Pfiberdrill
G00 Z0.1

(**********move off surface for tool change **********)
G90
G00 Z.2
```

```
Y0
X0

(********************* SUBROUTINE fiberdrill to make sensor divots*******)
Ofiberdrill
(calling program should have positioned mill 0.010 above)
(surface)

G91 (incremental units)
G83 R0 Z-0.275 Q0.075 F1.5  (peck drilling cycle)
X0.2206 Y0.2206 Z-0.275
G00 X-0.2206 Y-0.2206

G90  (back to absolute mode)

M99
```

`bottom_plate_alignment.fgc`

This file makes corner holes that will accept alignment pins to align the external mold to the internal mold. Use a #64 drill.

```
( ******************  Alignment corner posts  *****************)
G00 Z0.1
X-0.0445
Y-0.0445
G83 R0.05 Z-0.280 Q0.075 F1.5  (peck drilling cycle)
X1.0445
Y3.0445
X-0.0445
```

Bibliography

[1] M. Maharbiz, W. Holtz, R. Howe, and J. Keasling, "Microbioreactor arrays with parametric control for high-throughput experimentation," *Biotechnol. Bioeng.*, vol. 85, pp. 376–381, 2004.

[2] P. Harms, Y. Kostov, J. French, M. Soliman, M. Anjanappa, A. Ram, and G. Rao, "Design and performance of a 24-station high throughput microbioreactor," *Biotechnol. Bioeng.*, 2005.

[3] R. Puskeiler, A. Kusterer, G. John, and D. Weuster-Botz, "Miniature bioreactors for automated high-throughput bioprocess design (htbd): reproducibility of parallel fed-batch cultivations with escherichia coli." *Biotechnol. Appl. Biochem.*, vol. 42, no. 3, pp. 227–235, Dec 2005.

[4] N. Szita, P. Boccazzi, Z. Zhang, P. Boyle, A. Sinskey, and K. Jensen, "Development of a multiplexed microbioreactor system for high-throughput bioprocessing," *Lab on a Chip*, vol. 5, pp. 819–826, 2005.

[5] K. Lee, "Integrated polymer optical backplanes for fluorescence sensing," Master's thesis, Massachusetts Institute of Technology, 2006.

[6] R. M. Belagaje, S. G. Reams, S. C. Ly, and W. F. Prouty, "Increased production of low molecular weight recombinant proteins in escherichia coli," *Protein Science*, vol. 6, pp. 1953–1962, 1997.

[7] E. B. Jensen and S. Carlsen, "Production of recombinant human growth hormone in escherichia coli: Expression of different precursors and physiological effects of glucose, acetate, and salts," *Biotechnol. Bioeng.*, vol. 36, pp. 1–11, 1990.

[8] A. Ault, "The monosodium glutamate story: The commercial production of msg and other amino acids," *J. Chem. Educ.*, vol. 81, pp. 347–355, 2004.

[9] C. E. Nakamura and G. M. Whited, "Metabolic engineering for the microbial production of 1,3-propanediol," *Curr. Opin. Biotechnol.*, vol. 14, pp. 454–459, 2003.

[10] S. A. Freyer, M. Konig, and A. Kunkel, "Validating shaking flasks as representative screening systems," *Biochemical Engineering Journal*, vol. 17, pp. 169–173, 2004.

[11] J. Edwards, R. Ibarra, and B. Palsson, "In silico predictions of escherichia coli metabolic capabilities are consistent with experimental data," *Nat. Biotech.*, vol. 19, pp. 125–130, 2001.

[12] V. Singh, "Method for culturing cells using wave-induced agitation," U. S. Patent 6 190 913, 2001.

[13] D. Weuster-Botz, "Parallel reactor systems for bioprocess development," *Adv. Biochem. Engin./Biotechnol.*, vol. 92, pp. 125–143, 2005.

[14] S. Y. Lee, "High cell-density culture of *Escherichia coli*," *Trends Biotechnol.*, vol. 14, no. 3, pp. 98–105, 1996.

[15] R. G. Harrison, P. W. Todd, S. R. Rudge, and D. Petrides, *Bioseparations Science and Engineering.* New York: Oxford University Press, 2002.

[16] C. Lee, W.-J. Sun, B. Burgessa, B. Junker, J. Reddy, B. Buckland, and R. Greasham, "Process optimization for large-scale production of tgf-α-pe40 in recombinant *Escherichia coli*, effect of medium composition and induction timing on protein expression," *Journal of Industrial Microbiology and Biotechnology*, vol. 18, pp. 260–266, 1997.

[17] J. Altenbach-Rehm, C. Nell, M. Arnold, and D. Weuster-Botz, "Parallel bubble columns with fed-batch technique for microbial process development on a small scale," *Chem. Eng. Technol.*, vol. 22, no. 12, pp. 1051–1058, 1999.

[18] F. R. Schmidt, "Optimization and scale up of industrial fermentation processes," *Appl. Microbiol. Biotechnol.*, vol. 68, pp. 425–435, 2005.

[19] S. Y. Lee, "High cell-density culture of escherichia coli," *Trends in Biotechnology*, vol. 14, no. 3, pp. 98–105, 1996.

[20] H. Kitano, "Systems biology: a brief overview," *Science*, vol. 295, pp. 1662–1664, Mar 2002.

[21] A. Varma and B. Palsson, "Metabolic flux balancing: basic concepts, scientific and practical use," *Nat. Biotech.*, vol. 12, pp. 994–998, 1994.

[22] V. A. and P. B.O., "Stoichiometric flux balance models quantitatively predict growth and metabolic by-product secretion in wild-type escherichia coli w3110," *Appl. Environ. Microbiol.*, vol. 60, pp. 3724–3731, 1994.

[23] G. Stephanopoulos and K. L. Jensen, "Metabolic engineering: Developing new products and processes by constructing functioning biosynthetic pathways *in vivo*," *AIChE Journal*, vol. 51, no. 12, pp. 3091–3093, 2005.

[24] K. B. Andersen and K. von Meyenburg, "Are growth rates of escherichia coli in batch cultures limited by respiration?" *Journal of Bacteriology*, vol. 144, no. 1, pp. 114–123, 1980.

[25] B. Xu, M. Jahic, and S.-O. Enfors, "Modeling of overflow metabolism in batch and fed-batch cultures of escherichia coli," *Biotechnol. Prog.*, vol. 15, no. 1, pp. 81–90, 1999.

[26] V. Linek, P. Benes, and V. Vacek, "Measurement of aeration capacity of fermenters," *Chem. Eng. Technol.*, vol. 12, pp. 213–217, 1989.

[27] J. B. Gros, C. G. Dussap, and M. Catte, "Estimation of o_2 and co_2 solubility in microbial culture media," *Biotechnol. Prog.*, vol. 15, pp. 923–927, 1999.

[28] R. Hermann, M. Lehmann, and J. Buchs, "Characterization of gas-liquid mass transfer phenomena in microtiter plates," *Biotechnol. Bioeng.*, vol. 81, no. 2, pp. 178–186, 2003.

[29] W. A. Duetz, L. Ruedi, R. Hermann, K. O'Connor, J. Buchs, and B. Witholt, "Methods for intense aeration, growth, storage, and replication of bacterial strains in microtiter plates," *Appl. Environ. Microbiol.*, vol. 66, no. 6, pp. 2641–2646, Jun 2000.

[30] U. Maier and J. Buchs, "Characterization of the gas-liquid mass transfer in shaking bioreactors," *Biochem. Eng. J.*, vol. 7, pp. 99–106, 2001.

[31] L. Tolosa, Y. Kostov, P. Harms, and G. Rao, "Noninvasive measurement of dissolved oxygen in shake flasks," *Biotechnol. Bioeng.*, vol. 80, no. 5, pp. 594–597, Dec. 2002.

[32] D. Weuster-Botz, J. Altenbach-Rehm, and M. Arnold, "Parallel substrate feeding and ph-control in shaking-flasks," *Biochem. Eng. J.*, vol. 7, pp. 163–170, 2001.

[33] H. Onyeaka, A. W. Nienow, and C. J. Hewitt, "Further studies related to the scale-up of high cell density escherichia coli fed-batch fermentations: The additional effect of a changing microenvironment when using aqueous ammonia to control ph," *Biotechnol. Bioeng.*, vol. 84, no. 4, pp. 474–484, Nov. 2003.

[34] A. Zanzotto, N. Szita, P. Boccazzi, P. Lessard, A. Sinskey, and K. Jensen, "Membrane-aerated microbioreactor for high-throughput bioprocessing," *Biotechnol. Bioeng.*, vol. 87, pp. 243–254, 2004.

[35] S. R. Lamping, H. Zhang, B. Allen, and P. A. Shamlou, "Design of a prototype miniature bioreactor for high throughput automated bioprocessing," *Chem. Eng. Sci.*, vol. 58, pp. 747–758, 2003.

[36] Y. Kostov, P. Harms, L. Randers-Eichhorn, and G. Rao, "Low-cost microbioreactor for high-throughput bioprocessing," *Biotechnol. Bioeng.*, vol. 72, pp. 346–352, 2001.

[37] R. Puskeiler, K. Kaufmann, and D. Weuster-Botz, "Development, parallelization, and automation of a gas-inducing milliliter-scale bioreactor for high-throughput bioprocess design (htbd)," *Biotechnol. Bioeng.*, vol. 89, pp. 512–523, 2005.

[38] P. Boccazzi, A. Zanzotto, N. Szita, S. Bhattacharya, K. F. Jensen, and A. J. Sinskey, "Optimization and scale up of industrial fermentation processes," *Appl. Microbiol. Biotechnol.*, vol. 68, pp. 518–532, 2005.

[39] Z. Zhang, N. Szita, P. Boccazzi, A. Sinskey, and K. Jensen, "A well-mixed, polymer-based microbioreactor with integrated optical measurements," *Biotechnol. Bioeng.*, pp. 286–296, Dec 2005.

[40] D. Wester-Botz, R. Puskeiler, A. Kusterer, K. Kaufmann, G. T. John, and M. Arnold, "Methods and milliliter scale devices for high-throughput bioprocess design," *Bioprocess. Biosyst. Eng.*, vol. 28, pp. 109–119, 2005.

[41] D. Weuster-Botz, S. Stevens, and A. Hawrylenko, "Parallel-operated stirred-columns for microbial process development," *Biochem. Eng. J.*, vol. 11, pp. 69–72, 2002.

[42] A. D. Stroock, S. K. W. Dertinger, A. Ajdari, I. Mezic, H. A. Stone, and G. M. Whitesides, "Chaotic mixer for microchannels," *Science*, vol. 295, pp. 657–651, 2002.

[43] F. Schnfeld, V. Hessel, and C. Hofmann, "An optimised split-and-recombine micro-mixer with uniform chaotic mixing," *Lab on a Chip*, pp. 65–69, 2004.

[44] L.-H. Lu, K. S. Ryu, and C. Liu, "A magnetic microstirrer and array for microfluidic mixing," *Journal of Microelectromechanical systems*, vol. 11, no. 5, pp. 462–469, 2002.

[45] H. P. Chou, M. A. Unger, and S. R. Quake, "A microfabricated rotary pump," *Biomedical Microdevices*, vol. 3, pp. 323–330, 2001.

[46] M. Yi, H. Bau, and H. Hu, "A peristaltic meso-scale mixer," in *Micro Electro Mechanical Systems MEMS 2000 ASME International Mechanical Engineering Congress and Exposition.* ASME, 2000, pp. 367–374.

[47] K. Selverov and H. Stone, "Peristaltically driven channel flows with applications toward micromixing," *Physics of Fluids*, vol. 13, no. 7, pp. 1837–1859, 2001.

[48] D. B. Papkovsky, "New oxygen sensors and their application to biosensing," *Sensors and Actuators B*, vol. 29, pp. 213–218, 1995.

[49] H. L. T. Lee, P. Boccazzi, N. Gorret, R. J. Ram, and A. J. Sinskey, "*In situ* bioprocess monitoring of *Escherichia coli* bioreactions using raman spectroscopy," *Vibrational Spectroscopy*, vol. 35, no. 1-2, pp. 131–137, 2004.

[50] N. L. Swanson, B. D. Billard, and T. L. Gennaro, "Limits of optical transmission measurements with application to particle sizing techniques," *Appl. Opt.*, vol. 38, pp. 5887–5893, 1999.

[51] H. Suzuki, A. Sugama, and N. Kojima, "Micromachined clark oxygen electrode," *Sensor. Actuat. B-Chem.*, vol. 10, pp. 91–98, 1993.

[52] C.-C. Wu, T. Yasukawa, H. Shiku, and T. Matsue, "Fabrication of miniature clark oxygen sensor integrated with microstructure," *Sensor. Actuat. B-Chem.*, vol. 110, pp. 342–349, 2005.

[53] P. Bergveld, "Thirty years of isfetology what happened in the past 30 years and what may happen in the next 30 years," *Sensor. Actuat. B-Chem.*, vol. 88, pp. 1–20, 2003.

[54] T. Kalinowski, Z. Rittersma, W. Benecke, and J. Binder, "An advanced micromachined fermentation monitoring device," *Sensor. Actuat. B-Chem.*, vol. 68, pp. 281–285, 2000.

[55] M. Hofmann, D. Ellersiek, F. Kensy, J. Buchs, W. Mokwa, and U. Schnakenberg, "Galvanic decoupled sensor for monitoring biomass concentration during fermentation processes," *Sensor. Actuat. B-Chem.*, vol. 111-112, pp. 370–375, 2005.

[56] S. Hauttmann and J. Muller, "In-situ biomass characterization by impedance spectroscopy using a full-bridge circuit," *Bioprocess and Biosystems Engineering*, vol. 24, pp. 137–141, 2001.

[57] J. C. McDonald, D. C. Duffy, J. R. Anderson, D. T. Chiu, H. Wu, O. J. A. Schueller, and G. M. Whitesides, "Fabrication of microfluidic systems in poly(dimethylsiloxane)," *Electrophoresis*, vol. 21, pp. 27–40, 2000.

[58] J. Anderson, D. Chiu, R. Jackman, O. Cherniavskaya, J. McDonald, H. Wu, S. Whitesides, and G. Whitesides, "Fabrication of topologically complex three-dimensional microfluidic systems in pdms by rapid prototyping," *Anal. Chem.*, vol. 72, no. 14, pp. 3158–3164, Jul 2000.

[59] B.-H. Jo, L. M. V. Lerberghe, K. M. Motsegood, and D. J. Beebe, "Three-dimensional micro-channel fabrication in polydimethylsiloxane (pdms) elastomer," *Journal of Microelectromechanical Systems*, vol. 9, no. 1, pp. 76–81, March 2000.

[60] M. Unger, H. Chou, T. Thorsen, A. Scherer, and S. Quake, "Monolithic microfabricated valves and pumps by multilayer soft lithography," *Science*, vol. 288, pp. 113–116, 2000.

[61] K. Hosokawa and R. Maeda, "A pneumatically-actuated three-way microvalve fabricated with polydimethylsiloxane using the membrane transfer technique," *J. Micromech. Microeng.*, vol. 10, pp. 415–420, 2000.

[62] J. J. Sniegowski and M. P. de Boer, "Ic-compatible polysilicon surface micromachining," *Annu. Rev. Mater. Sci.*, vol. 30, pp. 299–333, 2000.

[63] G. T. A. Kovacs, N. I. Maluf, and K. E. Petersen, "Bulk micromachining of silicon," *Proceedings of the IEEE*, vol. 86, no. 8, pp. 1536–1551, 1998.

[64] M. Heckele and W. Schomburg, "Review on micro molding of thermoplastic polymers," *J. Micromech. Microeng.*, vol. 14, pp. R1–R14, 2004.

[65] L. Ceriotti, K. Weible, N. de Rooij, and E. Verpoorte, "Rectangular channels for lab-on-a-chip applications," *Microelectronic Engineering*, vol. 67-68, pp. 865–871, 2003.

[66] K. Kim, S. Park, J.-B. Lee, H. Manohara, Y. Desta, M. Murphy, and C. H. Ahn, "Rapid replication of polymeric and metallic high aspect ratio microstructures using pdms and liga technology," *Microsystem Technologies*, vol. 9, pp. 5–10, 2002.

[67] X.-M. Zhao, Y. Xia, and G. M. Whitesides, "Soft lithographic methods for nano-fabrication," *J. Mater. Chem.*, vol. 7, no. 7, pp. 1069–1074, 1997.

[68] J. W. V. Dyk, "Process for removing surface defects from articles having a thermoplastic surface," U. S. Patent 3 684 553, 1968.

[69] V. D. McGinniss, "Vaporous solvent treatment of thermoplastic substrates," U. S. Patent 4 529 563, 1985.

[70] D. Meyerhofer, "Characteristics of resist films produced by spinning," *J. Appl. Phys.*, vol. 49, pp. 3993–3997, 1978.

[71] A. G. Emslie, F. T. Bonner, and L. G. Peck, "Flow of a viscous liquid on a rotating disk," *J. Appl. Phys.*, vol. 29, pp. 858–862, 1958.

[72] W. V. Sorin and D. F. Gray, "Simultaneous thickness and group index measurement using optical low-coherence reflectometry," *IEEE Photon. Technol. Lett.*, vol. 4, pp. 105–107, 1992.

[73] J. Narasimhan and I. Papautsky, "Polymer embossing tools for rapid prototyping of plastic microfluidic devices," *J. Micromech. Microeng.*, vol. 14, pp. 96–103, 2004.

[74] L. M. Maurer, E. Yohannes, S. S. Bondurant, M. Radmacher, , and J. L. Slonczewski1, "ph regulates genes for flagellar motility, catabolism, and oxidative stress in escherichia coli k-12," *Journal of Bacteriology*, vol. 187, no. 1, pp. 304–319, 2005.

[75] C. Laritz and L. Pagel, "A microfluidic ph-regulation system based on printed circuit board technology," *Sensor. Actuat. A-Phys.*, vol. 84, pp. 230–235, Sep 2000.

[76] B. van der Schoot, M. Boillat, and N. de Rooij, "Micro-instruments for life science research," *IEEE T. Instrum. Meas.*, vol. 50, pp. 1538–1542, Dec 2001.

[77] T. Merkel, M. Graeber, and L. Pagel, "A new technology for fluidic microsystems based on pcb technology," *Sensors and Actuators A*, vol. 77, pp. 98–105, 1999.

[78] D. T. Eddington, R. H. Liu, J. S. Moore, and D. J. Beebe, "An organic self-regulating microfluidic system," *Lab on a Chip*, vol. 1, pp. 96–99, 2001.

[79] O. Tabata, K. Kawahata, S. Sugiyama, and I. Igarashi, "Mechanical property measurements of thin films using load-deflection of composite rectangular membranes," *Sensors and Actuators A*, vol. 20, pp. 135–141, 1989.

[80] C. T. Loy, S. C. Pradhan, t. Y. Ng, and K. Y. Lam, "A series solution approach to an analytical load-deflection relation for the measurement of mechanical properties of thin films," *J. Micromech. Microeng.*, vol. 9, pp. 341–344, 1999.

[81] J. M. Desimone, J. P. Rolland, and G. M. Denison, "Functional materials and novel methods for the fabrication of microfluidic devices," International Patent 2 005 084 191, 2005.

[82] A. Colas and J. Curtis, *Biomaterials Science*, B. D. Ratner, A. S. Hoffman, F. J. Schoen, and J. E. Lemons, Eds. Elsevier Academic Press, 2004.

[83] N. Amouroux and L. Leger, "Effect of dangling chains on adhesion hysteresis of silicone elastomers, probed by jkr test," *Langmuir*, vol. 19, pp. 1396–1401, 2003.

[84] S. Perutz, E. J. Kramer, J. Baney, C. Y. Hui, and C. cohen, "Investigation of adhesion hysteresis in poly(dimethylsiloxane) networks using the jkr techniqe," *J Polym. Sc. Pt. B-Polym Phys.*, vol. 36, pp. 2129–2139, 1998.

[85] J. P. Rolland, R. M. V. Dam, D. A. Schorzman, S. R. Quake, and J. M. DeSimone, "Solvent-resistant photocurable liquid teflon for microfluidic device fabrication," *J. Am. Chem. Soc.*, vol. 126, pp. 2322–2323, 2004.

[86] C. E. S. Denis and C. J. D. Fell, "Diffusivity of oxygen in water," *Can. J. Chem. Eng.*, vol. 49, p. 885, 1971.

[87] X. Lu, I. Manners, and M. Winnik, "Polymer/silica composite films as luminescent oxygen sensors," *Macromolecules*, vol. 34, pp. 1917–1927, 2001.

[88] E. Douglas, "Solubilities of oxygen, argon, and nitrogen in distilled water," *J. Phys. Chem.*, vol. 68, pp. 169–174, 1964.

[89] F. Sauges and W. Horsthemke, "Diffusive transport in spatially periodic hydrodynamic flows," *Phys. Rev. A*, vol. 34, pp. 4136–4143, 1986.

[90] M. N. Rosenbluth, H. L. Berk, I. Doxas, and W. Horton, "Effective diffusion in laminar convective flows," *Phys. Fluids*, vol. 30, pp. 2636–2647, 1987.

[91] I. Fridovich, "Oxygen toxicity: A radical explanation," *Journal of Experimental Biology*, vol. 201, pp. 1203–1209, 1998.

[92] C. von Bltzingslwen, A. K. McEvoy, C. McDonagh, B. D. MacCraith, I. Klimant, C. Krause, and O. S. Wolfbeis, "Sol-gel based optical carbon dioxide sensor employing dual luminophore referencing for application in food packaging technology," *Analyst*, vol. 127, pp. 1478–1483, 2002.

[93] J. Shiloach, J. Kaufman, A. S. Guillard, and R. Fass, "Effect of glucose supply strategy on acetate accumulation, growth, and recombinant protein production by *Escherichia coli* bl21 (λde3) and *Escherichia coli* jm 109," *Biotechnol. Bioeng.*, vol. 49, pp. 421–428, 1996.

[94] F. Wang and S. Y. Lee, "High cell density culture of metabolically engineered escherichia coli for the production of poly(3-hydroxybutyrate) in a defined medium," *Biotechnol. Bioeng.*, vol. 58, pp. 325–328, 1998.